5-2007

Experimental Aerodynamic Analysis of Converging Free Jets

Nathanael Tate McBee
University of Tennessee - Knoxville

To the Graduate Council:

I am submitting herewith a thesis written by Nathanael Tate McBee entitled "Experimental Aerodynamic Analysis of Converging Free Jets." I have examined the final electronic copy of this thesis for form and content and recommend that it be accepted in partial fulfillment of the requirements for the degree of Master of Science, with a major in Aerospace Engineering.

Robert Bond, Major Professor

We have read this thesis and recommend its acceptance:

Mancil Milligan, Rao Arimilli

Accepted for the Council:
Dixie L. Thompson

Vice Provost and Dean of the Graduate School

(Original signatures are on file with official student records.)

To the Graduate Council:

I am submitting herewith a thesis written by Nathanael Tate McBee entitled "Experimental Aerodynamic Analysis of Converging Free Jets." I have examined the final electronic copy of this thesis for form and content and recommend that it be accepted in partial fulfillment of the requirements for the degree of Master of Science, with a major in Aerospace Engineering.

Robert Bond
Major Professor

We have read this thesis and
recommend its acceptance:

Mancil Milligan

Rao Arimilli

Acceptance for the Council:

Linda Painter
Interim Dean of Graduate Studies

(Original signatures are on file with official student records)

EXPERIMENTAL AERODYNAMIC ANALYSIS OF CONVERGING FREE JETS

A Thesis
Presented for the
Master of Science
Degree
The University of Tennessee, Knoxville

Nathanael Tate McBee
May 2007

DEDICATION

I dedicate this thesis to my mother, father, two sisters and all of my close friends for their support, understanding and encouragement. Without their help, I would have given up long before now.

ACKNOWLEDGEMENTS

I would like to express my thanks to Dr. Robert Bond for his guidance with this project. His assistance, direction and availability were invaluable and extremely appreciated. Dr. Bond has always expressed a strong interest in the quality of education his students received. His teaching approach constantly maintained a high level of excitement which kept the students involved and interested. This same approach was carried out with his mentorship during this project and I was glad to have been working with him. I would also like to thank Dr. Mancil Milligan not only for his help with this project, but for his instruction and teaching. His knowledge and experience in the field gives each student a benchmark to pursue in their own careers. Thanks to Dr. J. Evans Lyne for his inspiration, friendship and encouragement. Finally, my thanks to Dr. Rao Arimilli for the challenges he introduced along with the encouragement and guidance to complete them.

ABSTRACT

The setup of the converging jets is commonly used in the manufacture of meltblown fibers. This requires forced airflow through small channels angled toward each other until meeting at the exit of the die. The emerging air jets impinge while molten polymer is extruded and becomes entrained in the air flow to be collected downstream as a thin cooled fiber.

The experimental analysis of converging free jets was examined to reveal characteristics of the flow field. A hot-film anemometer was used to gather and analyze the corresponding data for two separate meltblown fiber dies. These were examined and compared to each other as well as previous computational fluid dynamics studies of similar setups.

A traverse system was used to position the anemometer probe while measurements of the mean velocity and turbulence intensity were obtained at varying positions throughout the flow fields. This data was analyzed and compared to existing studies and theoretical prediction and was found to agree with existing computer models by showing three distinct regions: the first zone where each emerging jet maintains individual velocity profiles; a second mixing zone of maximum turbulence and an intermediate velocity profile; and a third zone where the individual jets are no longer present and the velocity profile becomes characteristic of a theoretical single emerging jet of similar mass flow rate.

TABLE OF CONTENTS

LIST OF FIGURES

NOMENCLATURE

α	Meltblowing die channel half angle (degrees)
κ	Thermal coefficient of resistance ($1/^{o}K$)
σ	Standard deviation
ρ	Fluid density (kg/m^3)
a	Calibration coefficient
A_W	Cross sectional area of the probe filament (m^2)
b	Calibration coefficient / 0.5 of Jet width (m)
c	Calibration coefficient
h	Heat transfer coefficient of convection of probe (W/m^2K)
I	Electrical current (amperes)
J	Momentum (kg*m/s)
l	Mixing length (m)
R_{REF}	Reference resistance (Ohms)
R_W	Resistance of the anemometer probe's wire-like filament (Ohms)
T_f	Temperature of the fluid of interest (K)
T_{REF}	Reference temperature (K)
T_W	Temperature of the anemometer probe's wire-like filament (K)
TI	Turbulence Intensity (%)
u	Instantaneous x-component of velocity (m/s)
u_{max}	Maximum velocity in x-direction (m/s)
v	Instantaneous y-component of velocity (m/s)
$\bar{v}$	Fluid mean velocity (m/s)
v'	Deviation from mean velocity (m/s)
v_f	Fluid velocity (m/s)
v_i	Fluid instantaneous velocity (m/s)
x	x-direction of coordinate frame
y	y-direction of coordinate frame
z	z-direction of coordinate frame

CHAPTER 1: INTRODUCTION

The experimental aerodynamic analysis of axisymmetric converging free jets was employed with the intent to measure the flow field representative of that encountered in the process of meltblown fiber production. The meltblown fiber jet's setup can be seen in Figure A-1. This figure and all subsequent figures are presented in Appendix A. In operation, the meltblown fiber jet produces an extruded strand of polypropylene which becomes entrained in the airflow of the jet where it is cooled and solidified. These fibers are collected to form the non-woven fabric which is utilized for cloth filters or other items where a woven fabric is not as efficient due to its grid-like pattern which could allow passage of particles.

The set up used for this research included the use of a hot film anemometer, a two dimensional traverse system and the meltblown fiber jet operating without producing fibers. Measurements of time averaged velocity ($\bar{v}$) and turbulence intensity (TI) were obtained with this equipment and provided an insight into the physical phenomenon taking place inside the flow field. Because this is an experimental study and not a simplified computer model, all of nature's influences such as edge effects of the nozzle or room recirculation will be present and show some effect on the experimental results.

The hot film anemometer used is made by TSI Instruments model IFA 300; this setup can be seen in Figure A-2. Utilizing its provided ThermalPro software, the anemometer system collects and organizes resulting experimental data for the user. More specifically, ThermalPro allows the user to select several parameters, run the experiment, and analyze the data in several simple steps.

The goal of this experiment was to try and reveal a representative model of the flow field and its behavior characteristic of a converging free jet setup. This included velocity profiles gathered at varying distances away from the exit plane of the nozzle. The gathered data was compared to results of previous computer models and predicted theoretical results.

CHAPTER 2. LITERATURE REVIEW

I. Free Jet

Free turbulent flow and its behavior is important in understanding how two converging jets may perform. This type of flow is considered free because there are no solid walls to restrict it. The absence of a solid wall boundary gives rise to the idea of a jet boundary. This occurs because of the differing velocities of the high speed stream and the stagnant fluid. This velocity gradient creates a turbulent mixing zone and causes the jet width to increase with distance downstream as shown in Figure A-3 [1]. As the emerging two-dimensional free jet is introduced to the surrounding fluid, this mixing causes it to entrain stagnant fluid at the edges. The centerline velocity will decrease with distance from the exit plane as the width of the jet simultaneously increases. The turbulence of the stream as well as the viscosity helps with the entrainment of the surrounding fluid. This causes the increasing mass flow of the jet, keeping in mind that the velocity magnitude will simultaneously be dropping as the jet width increases. This ensures that the overall momentum is conserved.

The following equations will relate the mixing length, jet width, and ultimately the centerline velocity in relation to downstream position. Here we introduce the ratio of the mixing length *l* to the jet width *b*.

$$\frac{l}{b} = \beta = const \qquad \textbf{(2.1)}$$

Next we relate the transverse velocity fluctuation with the mixing length.

$$\frac{Db}{Dt} \sim v' \tag{2.2}$$

where for steady state flow,

$$\frac{D}{Dt} = u\frac{\partial}{\partial x} + v\frac{\partial}{\partial y} \tag{2.3}$$

Assuming that both the transverse and the downstream fluctuations are of the same order,

$$\left|\overline{v'}\right| = const \times \left|\overline{u'}\right| = const \times l\frac{d\overline{u}}{dy} \tag{2.4}$$

where $\left|\overline{u}\right|$, $\left|\overline{u'}\right|$, and $\left|\overline{v'}\right|$ are time-averaged velocities. Comparing equation **(**2.4**)** with equation **(**2.2**)** yields,

$$\frac{Db}{Dt} \sim l\frac{\partial u}{\partial y} \tag{2.6}$$

The average value of $\frac{\partial u}{\partial y}$ taken over half the width of the jet is assumed to be approximately proportional to $\frac{u_{\max}}{b}$, therefore

$$\frac{Db}{Dt} = const \times \frac{l}{b}u_{\max} = const \times \beta u_{\max} \tag{2.7}$$

$$\frac{Db}{Dt} \sim u_{\max}\frac{db}{dx} \tag{2.8}$$

Combining equation **(**2.7**)** and **(**2.8**)**,

$$\frac{db}{dx} = const \times \frac{l}{b} \tag{2.9}$$

therefore

$$b = const \times x \tag{2.10}$$

This confirms that the width of the jet is proportional to the distance x.

In order to develop a relationship between the centerline velocity and the axial distance x, we look at the x-component of momentum for incompressible flow

$$J = \rho \int u^2 dA = const \tag{2.11}$$

where J is the momentum, ρ is the density, and A is the area. Equation (2.11) may be implemented because of the assumption that the pressure is constant everywhere except close to the nozzle exit. In two dimensions, the previous equation takes the following form,

$$J' = const \times \rho u_{\max}^2 b \tag{2.12}$$

in which J' is the momentum per unit length. This means,

$$u_{\max} = const \times b^{-1/2} \sqrt{\frac{J'}{\rho}} \tag{2.13}$$

Joining this equation with **(**2.10**)**, results in,

$$u_{\max} = const \times \frac{1}{\sqrt{x}} \sqrt{\frac{J'}{\rho}} \tag{2.14}$$

which shows that the centerline velocity is proportional to the inverse square root of x

$$u_{\max} \sim x^{-1/2} \tag{2.15}$$

II. Parallel Free Jets

The preceding results are well known and boundary layer theory is excellent in predicting the behavior of the flow. This is not the case for parallel jets emerging close to one another. The two jets interact with each other in a complicated manner which proves to be very difficult to solve in a mathematical sense. There have been several studies

concerning this phenomenon and correlations between experimental and computational results are closely related.

The most notable concurrence is that of the numerically predicted points where the jets begin to merge. This along with the centerline velocity profiles agree very well with the available experimental data [2]. This gives rise to three distinct zones: a converging region, a merging region and a combined region. This can be seen in Figure A-4 for converging free jets [3]. The results of this study show a good relationship between the computational and experimental merging points but the computational models show a narrower jet envelope than that revealed by experiment.

III. Converging Free Jets

While there has been substantial documentation on parallel free jets, the case of non-parallel free jets is far less represented. Converging jets refer to a case where jets are oriented toward each other at some half angle α about the centerline.

Converging jets still retain the same three distinct regions observed in parallel jets. Before merging in the second region, the two emerging jets maintain their own individual characteristics while the third region is characteristic of a fully developed single jet. While the same three regions of interest as present in the case of parallel free jets, the characteristics of the individual emerging jets are strongly dependent on α. The merging and combined regions (greater than 40 nozzle diameters downstream) [3] are relatively independent of α.

Parallel jets display a great capacity for entrainment of the surrounding fluid while this characteristic decreases with increasing α for the case of converging jets. This is obvious until the observer moves far enough downstream where the converging jets resemble a single jet with a similar mass flow rate. The downstream regions of the converging jets are somewhat independent of the preliminary geometry.

The driving force behind the flow characteristics is the conservation of momentum. As the angle α increases, the mixing of the two jets becomes more intense. This is noticeable in the centerline velocity profiles where the 60 degree die shows a much more rapid decrease in the mixing region as compared to the 30 degree die. This would mean that as the half angle increases, the turbulence will increase as well.

CHAPTER 3. EXPERIMENTAL SETUP AND PROCEDURE

The key component in the ability to analyze the flow field was the use of the hot film anemometer. The anemometer used in this experimental setup is made by TSI Instruments model IFA 300. Utilizing its provided ThermalPro software, the anemometer system collects and organizes resulting experimental data for the user. More specifically, ThermalPro allows the user to select several parameters, run the experiment, and analyze the data in several simple steps. This device is used frequently not only in analyzing flow fields of air and other gases, but liquid flow fields as well. The anemometer has been used extensively because of its ability to make high frequency measurements of velocity [7]. The system consisted of a data acquisition computer, anemometer controller and the hot film probe. This probe was the central element responsible for collecting the data in the flow field. It is essentially a thin wire-like filament which is maintained at a specific temperature by the controller. As air flows past the filament, it is cooled by convection. This cooling sends a voltage difference to the controller where it is measured and corrected in order to maintain the constant temperature across the filament. These increases and decreases in voltage are recorded and converted into velocity readings.

I. Velocity Calculation

Velocity readings using hot film anemometers are obtained by relating the differences in the voltage to a predetermined calibration curve. The following calculations give an example of how these are determined.

Assume the anemometer probe is immersed in a flow and is heated by an electrical current. The electrical power input is equal to the power lost by convective heat transfer as follows,

$$I^2 \cdot R_W = h \cdot A_W (T_W - T_f) \tag{3.1}$$

The wire resistance, R_W, is a function of temperature according to the following equation

$$R_W = R_{REF}[1 + \kappa(T_W - T_{REF})] \tag{3.2}$$

where κ is the thermal coefficient of resistance. King's law relates the heat transfer coefficient to the fluid velocity as

$$h = a + b \cdot v^c{}_f \tag{3.3}$$

Where a, b, and c are calibration coefficients ($c \approx 0.5$).

Combining the previous equations results in the following

$$a + b \cdot v^c{}_f = \frac{R_{REF}[1 + \kappa(T_W - T_{REF})]}{A_W (T_W - T_f)} \tag{3.4}$$

This allows the fluid velocity, v_f, to be solved. The fluid velocity is found to be

$$v_f = \left\{ \left[\frac{I^2 R_{REF}\left[1 + \kappa(T_W - T_{REF})\right]}{A_W (T_W - T_f)} - a \right] / b \right\}^{\frac{1}{c}} \tag{3.5}$$

This gives the fluid velocity to be a function of the wire temperature with a known fluid temperature [6].

II. Turbulence Intensity

A highly useful parameter that can be found from the high speed data acquired with the anemometer is turbulence intensity. Turbulence intensity is a dimensionless number that relates the deviation of instantaneous velocity from the mean value across the sampled time period.

The instantaneous velocity of the flow can broken into two components with the following equation

$$v_i = \bar{v} + v' \tag{3.6}$$

Where v_i is the instantaneous velocity magnitude, $\bar{v}$ is the mean velocity magnitude, and v' is the instantaneous deviation from the mean. These are velocity magnitude measurements because the flow direction cannot be distinguished using only a single probe setup like the one used in this experiment.

The standard deviation is a statistical measure of data dispersion about a mean value and is represented as

$$\sigma^2 = \frac{1}{N}\sum_{i=0}^{N-1}(v_i - \bar{v})^2 \tag{3.7}$$

Substituting 3.6 into 3.7 gives

$$\sigma^2 = \frac{1}{N}\sum_{i=0}^{N-1}(v_i')^2 \tag{3.8}$$

Therefore,

$$\sigma^2 = \overline{v'^2} \tag{3.9}$$

The standard deviation is now

$$\sigma = \sqrt{\sigma^2} = (\overline{v'^2})^{1/2} \tag{3.10}$$

A large turbulent instance in the flow will give rise to velocity deviations from the mean and large standard deviation values. The dimensionless parameter turbulence intensity is now given by

$$TurbulenceIntensity = \frac{\sqrt{\overline{v'^2}}}{\bar{v}} \tag{3.11}$$

The ThermalPro software outputs a measurement of the turbulence intensity for each sampled time period. Collecting these measurements over a two dimensional space could reveal areas of high turbulence which may in turn point out areas of large eddy formation.

III. Calibration

The anemometer probe is a highly sensitive piece of equipment and needs to be calibrated in order to accurately represent the data that will be collected. For example, if the experiment called for a low velocity regime, the calibration of the probe should be done inside the limits of that regime. In the case of the meltblown fiber jet, the tests were run with back pressures up to 12 psig. This was the upper limit for initial calibration of the anemometer.

The anemometer was calibrated using the TSI model 1127 calibration device. This is a small pressure driven chamber with a small exit orifice. The calibration device was connected to an air line and a ten foot water manometer. The manometer was used to record the stagnation pressure for the calibration device and entered into the Thermal

Pro software. Once the air line pressure was adjusted and the reading from the manometer recorded, the software records the corresponding velocity exiting the calibration device's orifice. Adjusting the pressure and capturing several data points allowed for the software to create a calibration curve specific to that particular probe. This calibration curve was used as a correlation between the measured voltage fluctuations and the associated velocities from the calibration device. This calibration data can be seen in Fig A-5. Data retrieved from the ThermalPro software is reported in m/s while the traverse system was set up in inches. These units will be represented in the figures corresponding to this analysis.

IV. Data Collection

The process of data collection constituted the majority of the experimental effort. This proved to be the most time consuming aspect of the project due to its involvement with a manual traverse system. This was used to position the anemometer probe in the flow field while the velocity data were acquired. The traverse was repositioned for each data point by manually dialing it to the appropriate position. The approach involved starting the measurements at the exit face of the nozzle and gradually working downstream. The typical flow field measurements consisted of several hundred data points with the greater part of the concentration within the first few inches of the nozzle exit.

V. Anemometer Frequency

The ThermalPro software offered the flexibility to adjust the anemometer's operating frequency. Without knowing the anticipated frequency of the eddy formation, the flow needed to be tested within a range of frequencies in order to determine the appropriate frequency for the remainder of the analysis. This was accomplished by positioning the probe at the centerline of the flow field at a position of 3 inches from the nozzle exit. Data was acquired over a period of 1 second at frequencies from 10 kHz to 50 kHz. Figure A-6 shows the results from this study. It was observed that the average velocity remained relatively constant between 1000Hz and 50 kHz, but the turbulence intensity did not show constant properties until above roughly 20 kHz. Based on this observation, the rest of the experimental analysis was conducted at an acquisition rate of 40000 Hz.

VI. Transverse Profile

The idea behind the single probe analysis is to collect the time dependent velocity at each given point and construct an average velocity profile at varying distances from the jet exit. The first case studied was an effort to determine whether the horizontal transverse (z – direction corresponding to Figure A-3) had any effect on the average velocity or if the jet was two dimensional. The probe was first placed on the outside edge of the nozzle exit and measurements were taken straight across the jet face until reaching the other side. The resulting velocity profile is shown in Figure A-7. This clearly shows that the average velocity across the jet face is relatively constant except for the far edges

which would be expected. Based on this, the jet was assumed to be two dimensional in nature and further data acquisition was confined to the center (2.5 inches) in the horizontal z-direction.

VII. Velocity Field

The first flow field to be examined corresponded to a back nozzle pressure of 2 psig with a channel half angle of 30 degrees. The channel width measured approximately 0.1 inches and the die face at the intersection of the channels measured about 0.015 inches. The front face of the die tapered at an angle of 10 degrees from the vertical y-direction.

The back pressure was set to 2 psig by opening the valve to allow the air supply to flow through a series of air filters and a regulator. The pressure was read from a pressure gauge to find the appropriate operating condition and to observe the pressure throughout the analysis. The pressure was monitored to ensure that no noticeable fluctuation of back pressure occurred during the data acquisition.

The flow field data acquisition was approached by starting at the exit of the nozzle and working downstream in small step sizes. The velocity profile was captured at each x-position by taking several data points in both the +y and –y directions (reference axes can be seen in Figure A-1). The traverse system allowed a full capture of the flow field throughout the first few inches, however the +y direction was not fully captured far downstream due to the fact that the velocity field grew larger than the traverse was set up to reach. This disadvantage proved minimal since this occurred in the combined region

and had the characteristics of a fully developed single jet. The –y direction was fully captured and gave insight into the velocity profile and its symmetry.

The next flow field examined corresponded to the same 2 psig back pressure setting but had a half angle of 60 degrees. The channel width measured 0.040 inches and the die face at the intersection of the channels measured 0.015 inches. The front face of the die tapered at an angle of 10 degrees from the vertical.

This flow field was approached with the same procedure as before. The system was set to 2 psig and monitored throughout the data gathering.

The final flow field observed was a sort of matched setting between the 30 degree die and the 60 degree die. The centerline velocity at an x-position of 0.3 inches from the 30 degree die was used as a reference point in order to match the velocity at the same position using the 60 degree die. This was done to match the velocity in the third region of the flow fields at this point and investigate the change in back pressure required to maintain the matched velocity at that point in the flow field.

CHAPTER 4. RESULTS

I. Thirty and Sixty Degree Comparison

The first comparison set of experimental data is for both the 30 and 60 degree dies being analyzed with a back pressure of 2 psig. These were first investigated by comparison of the centerline velocities and turbulence intensity as a function of distance from the die. These results can be seen in Figure A-8 and Figure A-9. It is clear by looking at the figures that the different geometries play a large role in the difference between centerline velocities. The largest difference can be seen at the nozzle exit. The 60 degree die shows a much more significant increase in velocity. This occurs because the two emerging jets impinge more dramatically than in the case of the 30 degree die. The overall shape and characteristic of the two profiles, however, are relatively similar in the mixing and combined regions. The turbulence intensity is shown in both figures as well and shows almost identical patterns except for the area at the die exit. Both figures show the turbulence intensity rising steadily after the mixing region and leveling off to a maximum value just below twenty percent. This can be expected since both velocity profiles are similar except for the regions at the die exit. Figure A-10 shows both centerline velocity profiles plotted together and normalized using the respective peak velocities to better visualize the overall characteristics. It is clear that the two flow fields show similarity, however the 30 degree die appears to experience less viscous dissipation throughout the flow due to the quicker decrease of the centerline velocity after the mixing region in the case of the 60 degree die. The next area of interest was the velocity profiles at several positions downstream of the nozzle exit. The converging region was of

particular interest which was where the positioning of the data points was the closest in an attempt for a better representation of the actual velocity profiles in that region. Figure A-11 shows the velocity profiles at the nozzle exit for the 60 degree die. The velocity profile reveals the characteristics of both emerging jets maintaining their own shapes as expected. It is also interesting to note that the turbulence intensity rises dramatically at low velocities. This is due to the large fluctuations occurring between such low measured velocities and would be expected. These data are not shown for the 30 degree case as there were not enough data taken to resolve the peaks. Although the presence of two emerging jets can be better visualized with more data points, the overall effect is still seen from the centerline velocity profiles which show the same increase in velocity within the first few tenths of an inch from the nozzle exit. Should the data acquisition of the 30 degree die been at a higher resolution like that of the 60 degree die, it would be expected to show the same behavior. This agrees well with the findings shown in Figure A-12**.** This figure was the result of a previous study by Hatcher [3], and shows the velocity profile for a 30 degree die similar to the one studied here. The flow was driven by a 10 psig back pressure and modeled with the CFD software package FLUENT. These computational results show good agreement with the experimental trends obtained with the 30 and 60 degree dies.

The next region of interest was the merging region. This occurs as the two emerging jets begin to merge together but still retain some characteristics of individual jets. Figure A-13 shows the velocity profile at 0.1 inches from the nozzle exit for the 60

degree die which is in this region. The two jets have begun to merge together, but still maintain some single jet characteristics such as independent velocity peaks.

The final region, the combined region, makes up the rest of the flow field and is typical of the behavior of a single emerging jet. Figures A-14 and A-15 show this region for both the 30 degree die and the 60 degree die respectively. The remainder of the figures showing the acquired data for the flow field representative of both the 30 degree die and the 60 degree die are included in Appendix B. All supporting figures for the 30 degree die are shown in Figures B-1 through B-23**,** while the supporting figures for the 60 degree die are shown in Figures B-24 through B-46**.** These figures show the velocity profiles obtained at sequential distances from the nozzle exit.

II. Thirty and Sixty Degree Velocity Matched Comparison

The next comparison was that of the 30 degree die at a back pressure of 2 psig compared with the 60 degree die at a back pressure of 2.125 psig. This was done in order to match the centerline velocity at an arbitrary distance of .3 inches from the nozzle exit to provide a point of similarity after the two emerging jets begin to mix. The centerline velocity for both cases can be seen in Figure A-16**.** Although the velocity is matched at one point, the 60 degree die still looses energy to viscous mixing just as was seen in Figure A-10**.** The velocity does reach a higher maximum because of the increased back pressure, but shows the same characteristics in the final combined region as seen previously at 2 psig back pressure. The viscous forces remove the energy in the mixing region while the combined region retains characteristics of a single emerging free jet as

seen in both figures. A plot of the normalized centerline velocity is also shown in Figure A-17

The supporting figures for the 60 degree die at this back pressure are shown in Figures B-47 to B-63**.** The converging region of the flow is evident in Figure A-18 showing the individual jets maintaining their individual velocity profiles. Although the velocity profile at the exit of the nozzle look similar to a profile expected in the mixing region, it still maintains individual jet characteristics. This profile would not include the center mixing between the two jets if the anemometer probe were able to fit inside the exit channel. At such a large half angle α, the mixing of the jets occurs extremely rapidly at the exit of the individual jet channels.

The mixing region is noticeable in Figure A-19 which shows the mixing region almost complete at a distance of only one tenth of an inch from the nozzle exit. The rest of the supporting figures for this case show the velocity profiles at sequential distances from the nozzle exit. The jet takes on the same characteristics as a single emerging free jet while the velocity profile shows the jet width to enlarge with increasing distance from the nozzle exit demonstrating the conservation of momentum expected.

III. CFD Comparison

A computational fluid dynamic (CFD) model of the 60 degree die with the same 2 psig back pressure was analyzed in much the same way by Haynes [4]. A time dependent analysis at 1 inch from the nozzle exit is shown in Figure A-20**.** The corresponding time dependent data for the experimental procedure can be seen in Figure A-21 shown for a

one second sample**.** A comparison between the CFD and experimental data reveals a similarity in the time averaged velocity although the CFD model shows a larger range in fluctuation which could be due to various turbulence models employed in CFD packages to simulate turbulent fluctuations.

Comparison was also examined at a position of 2 inches which can be seen in Figures A-22 and A-23 respectively**.** These still show similarity in the overall time averaged velocity just as the comparison at 1 inch did, but the CFD fluctuations still show much higher velocities than those which were experienced experimentally.

Centerline velocity was also an area where the CFD and experimental results were very similar. Figure A-24 shows the centerline velocity as obtained by CFD analysis on a 30 degree die operating at a back pressure of 10 psig [3]. It can be seen that the curve fit for the data reveals an inverse of the square root of distance x, which is what was obtained theoretically in chapter 2. The experimental result is shown in Figure A-25. The curve fit for the experimental results is proportional to x^-.4771 which agrees very closely with both the theoretical and CFD results.

Overall, the CFD analysis seems to provide a great starting point for analyzing flows such as the ones which were examined here. A computational analysis will reveal characteristics like those which would be seen experimentally.

IV. Eddy Formation

The formation of circulating eddies is a flow characteristic that can sometimes be recognized through experimental analysis such as this. The interaction of the small and

large eddies are unpredictable to a certain extent but may possibly be noticed experimentally by analyzing the time dependent velocity graphs provided by the ThermalPro software and looking for some nature of repetitive patterns. With the amount of data collected, it was out of the scope of this project to analyze the time dependent data at each location in the flow, but looking through some of the data at a surface level revealed some characteristics of repeating patterns such as seen in Figure A-26**.** This shows what looks to be a repetitive pattern in the time dependent data. According to this figure, the pattern repeats roughly three times in a dT=0.00135 seconds, which means the pattern repeats at a frequency of about 2.2 kHz at this location. Deeper analysis in this area may reveal more patterns in different areas of the analyzed flow.

CHAPTER 5. CONCLUSIONS AND RECOMMENDATIONS

I. Conclusions

The following conclusions are based on the experimental analysis obtained in this study

1. The hot film anemometer provided an excellent measurement of the flow field for the converging free jet setup and showed good agreement with available CFD results and theoretical findings.
2. The self-similar zone of the flow displays the velocity distribution predicted by theory.
3. The converging jet configuration displays three distinct regions: the first where the two jets maintain individual characteristics, the second where the two jets begin to merge, and the third where the jets have merged and show characteristics of a single, similar jet.
4. Turbulence intensity indicates that turbulent kinetic energy is at a maximum in the merging zone [3].
5. The hot film anemometer showed frequency sample rate dependent results. Below certain frequencies, approximately 20 kHz, the anemometer did not produce results which accurately depicted the flow.
6. The flow can be assumed constant in the transverse z-direction except near the far edges.

7. Increasing the half angle from 30 degrees to 60 degrees resulted in higher dissipation in the merging zone, while the two geometries resulted in similar combined zones.

II. Recommendations

The following are recommendations to further the experimental analysis and support the above conclusions.

1. A comparison between an actual single emerging jet and the converging jet with the same operating back pressure is needed to examine how closely the third region of the converging jet setup resembles it.
2. The setup should be upgraded to include two or more simultaneous anemometers (x-probe) in order to analyze the flow in two dimensions rather than the one dimensional analysis conducted in this experiment.
3. The experiment could be more conclusive if the dies used were similar in channel width, die face taper, and only differed in their channel half angles. In addition, it could be helpful to analyze similar dies with differing face angles with respect to the vertical. These dies are expensive and difficult to machine which makes a CFD analysis a much more attractive option.
4. The experimental data which was gathered could be further analyzed and studied with spectrum analysis and correlation software. The anemometer manufacturer provided such a software package, however this type of analysis was outside of the scope of this study.

5. A wider range of back pressures could be analyzed with anemometer calibration for each range of expected velocities.
6. Time dependent data could be looked into closely to try and identify areas of suspected eddy formation.

REFERENCES

1. Schlichting, H., *Boundary Layer Theory*. Translated by J. Kestin. 1955, New York: McGraw-Hill.

2. Spall, R. E. and E. A. Anderson. *Experimental and numerical investigation of two-dimensional parallel jets*. in Proceedings of the ASME Fluids Engineering Division Summer Meeting. 2003.

3. Hatcher, G. W., *Computational Aerodynamic Analysis of Converging Free Jets*. 2004, Masters Thesis: University of Tennessee, Knoxville.

4. Haynes, J. X., *An Investigation On The Use Of Computational Fluid Dynamics To Simulate The Turbulent Phenomena From A Melt-blowing Die*. 2006, Masters Thesis: University of Tennessee, Knoxville.

5. TSI Inc., IFA 300 Constant Temperature Anemometer System Instruction Manual. TSI Inc., 2000

6. "eFunda: Theory of Hot-Wire Anemometers". 2003. eFunda. March 10, 2006 http://www.efunda.com/designstandards/sensors/hot_wires/hot_wires_theory.cfm

7. TSI Inc., Innovation in Thermal Anemometry – A Complete Family of Thermal Anemometry Systems, Probes, and Accessories. TSI Inc., 2006

8. Taglia, C., *Numerical and Experimental Investigation of an Annular Jet Flow With Large Blockage*. 2004. ASME. September 21, 2006 http://www.ltnt.ethz.ch/img/deltaglia.pdf

9. “Free and Forced Convection”. September 21, 2006 http://www.me.wustl.edu/ME/labs/thermal/me372b3.htm

10. McDonough, J. M. *Introductory Lectures on Turbulence*. 2004, University of Kentucky Departments of Mechanical Engineering and Mathematics.

11. Munson, B. R., Young, D. F. and Okiishi, T. H., Fundamentals of Fluid Mechanics. Canada: John Wiley & Sons, Inc., 1994.

12. Tennekes, H. and Lumley, J. L., A First Course In Turbulence. Cambridge: The MIT Press, 1972.

13. White, Frank M., Viscous Fluid Flow. Singapore: McGraw-Hill, 1991.

14. Lomas, Charles G., Fundamentals of Hot Wire Anemometry. Cambridge: Cambridge University Press.

APPENDIX A: FIGURES

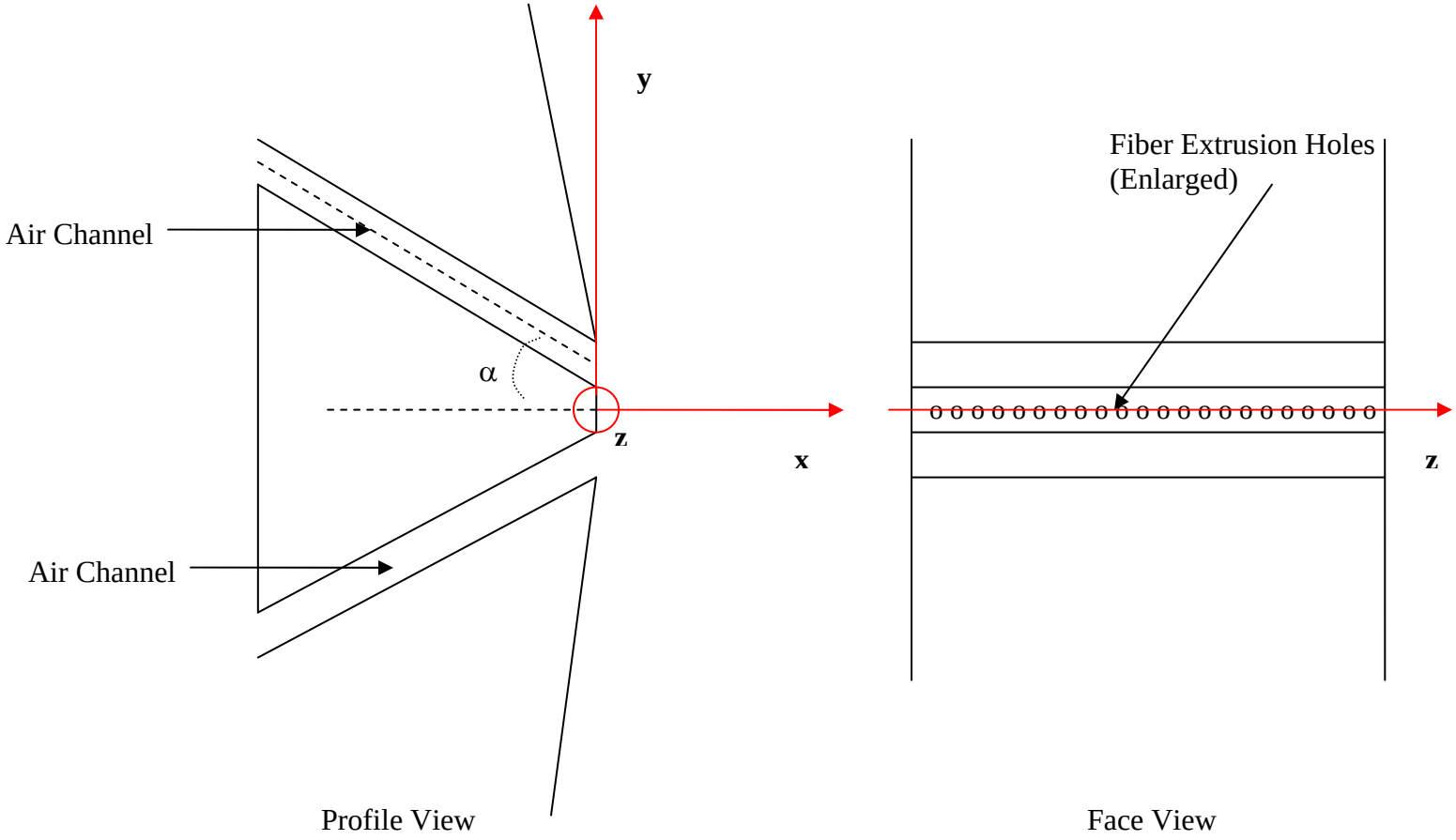

Figure A-1
Meltblowing Schematic

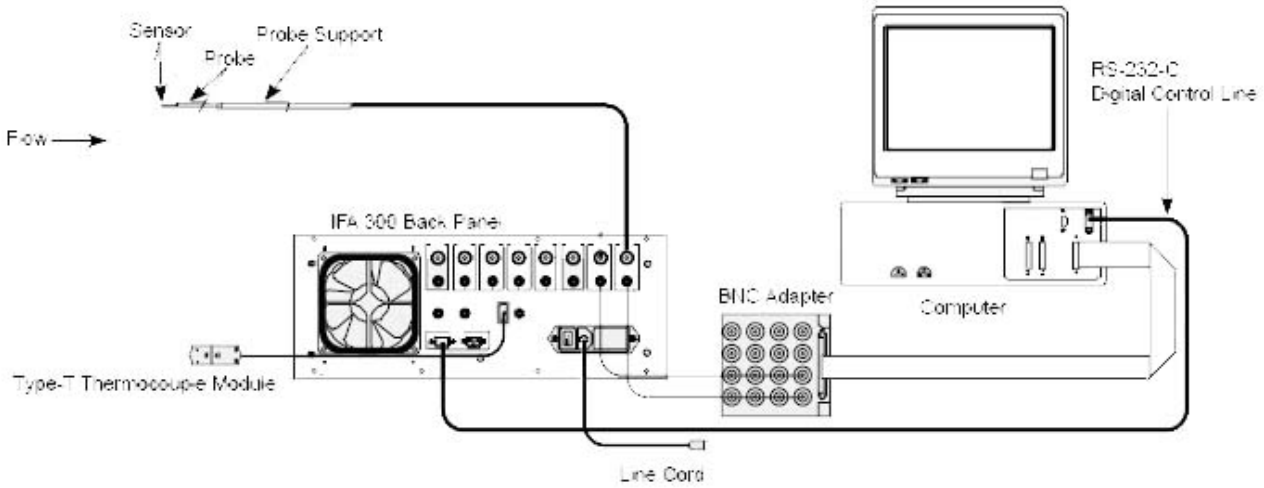

Figure A-2
IFA 300 Anemometer Setup [5]

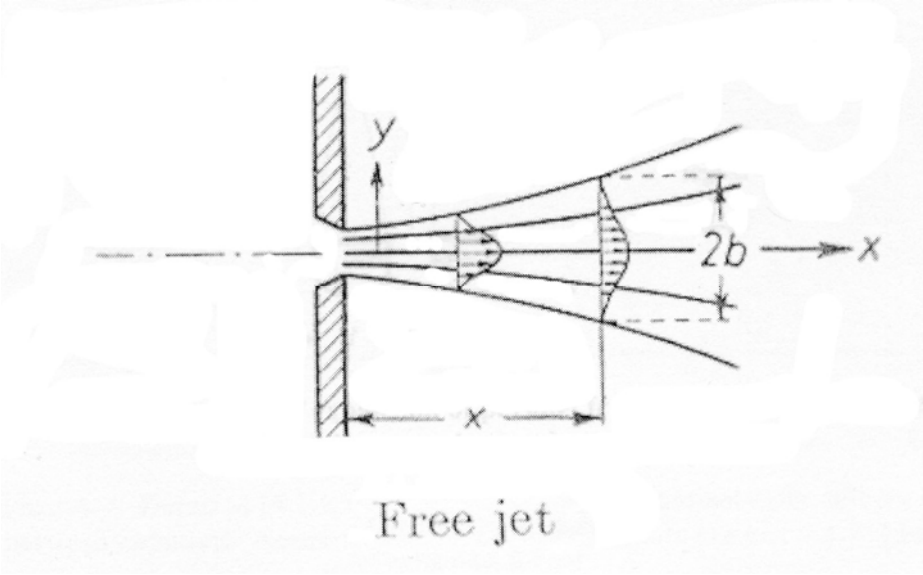

Figure A-3
Free Jet Schematic [3]

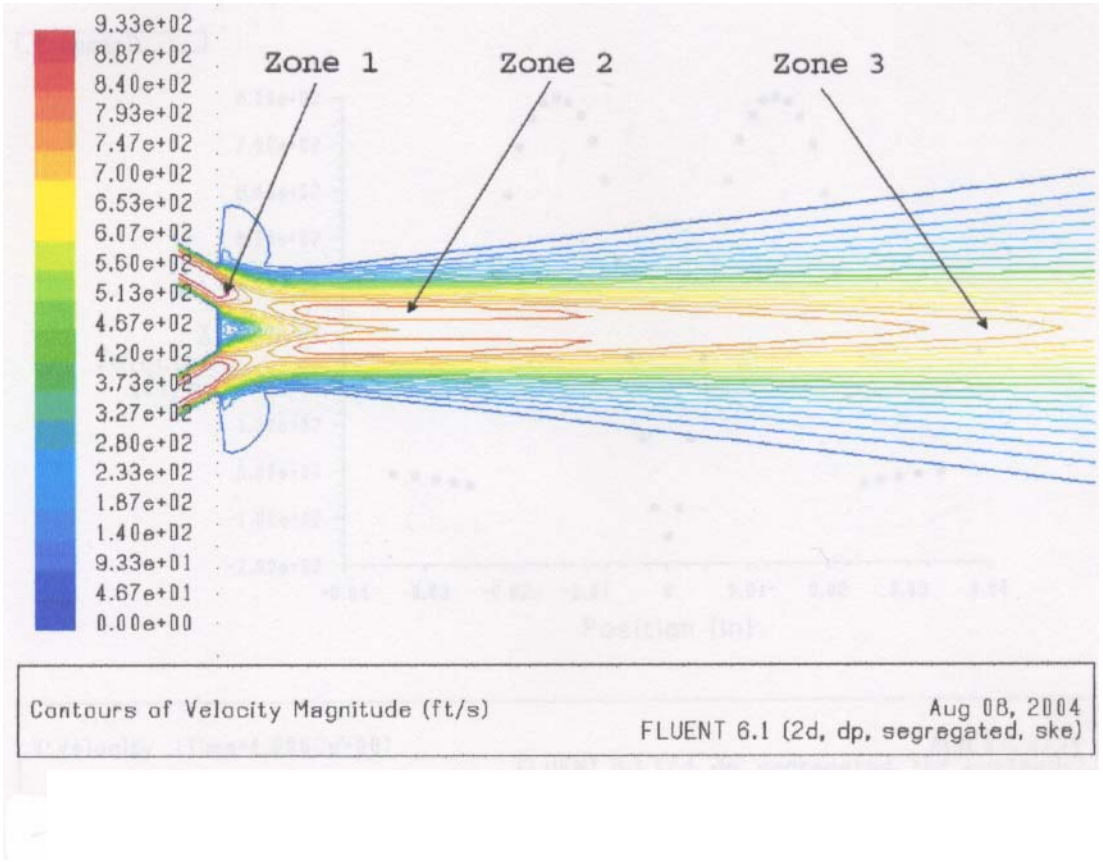

Figure A-4
FLUENT Representation (30 Degree Die – 10 psig Back Pressure) [3]

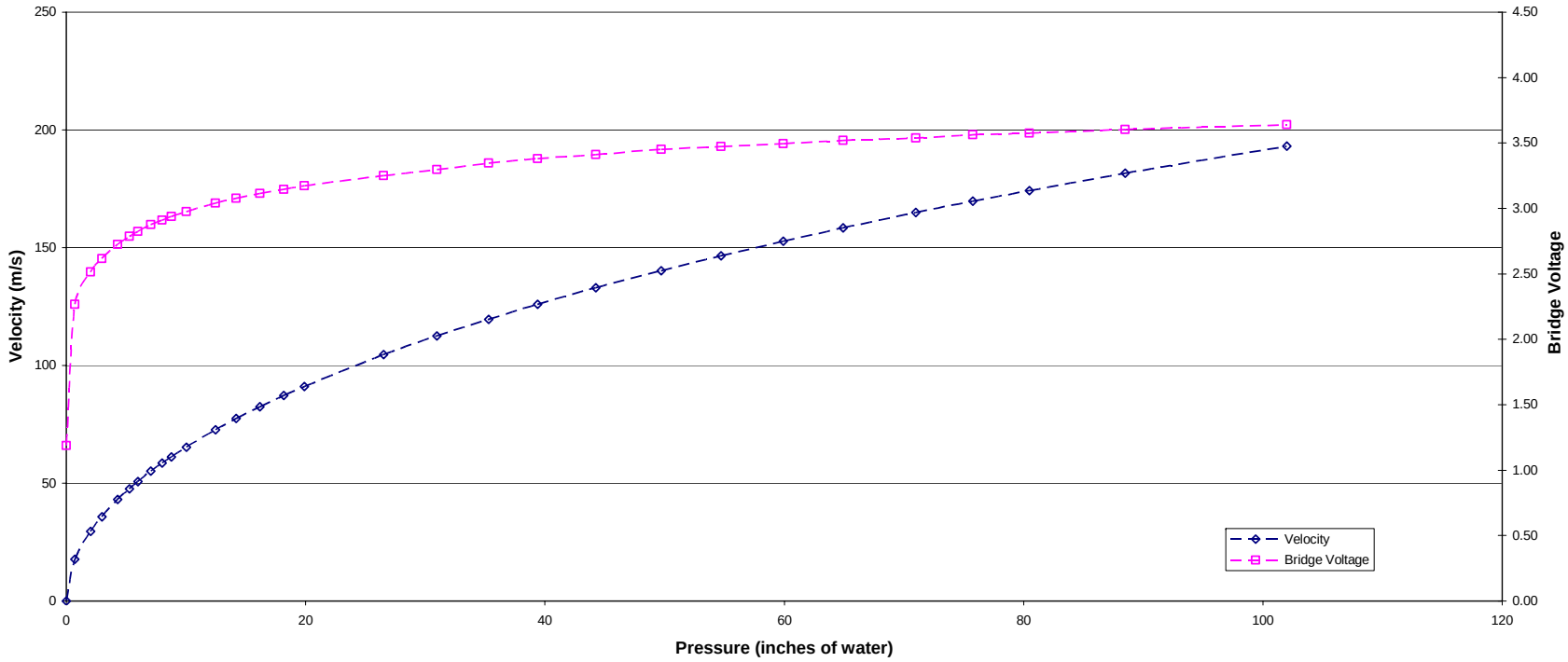

Figure A-5
Velocity and Bridge Voltage as a Function of Pressure

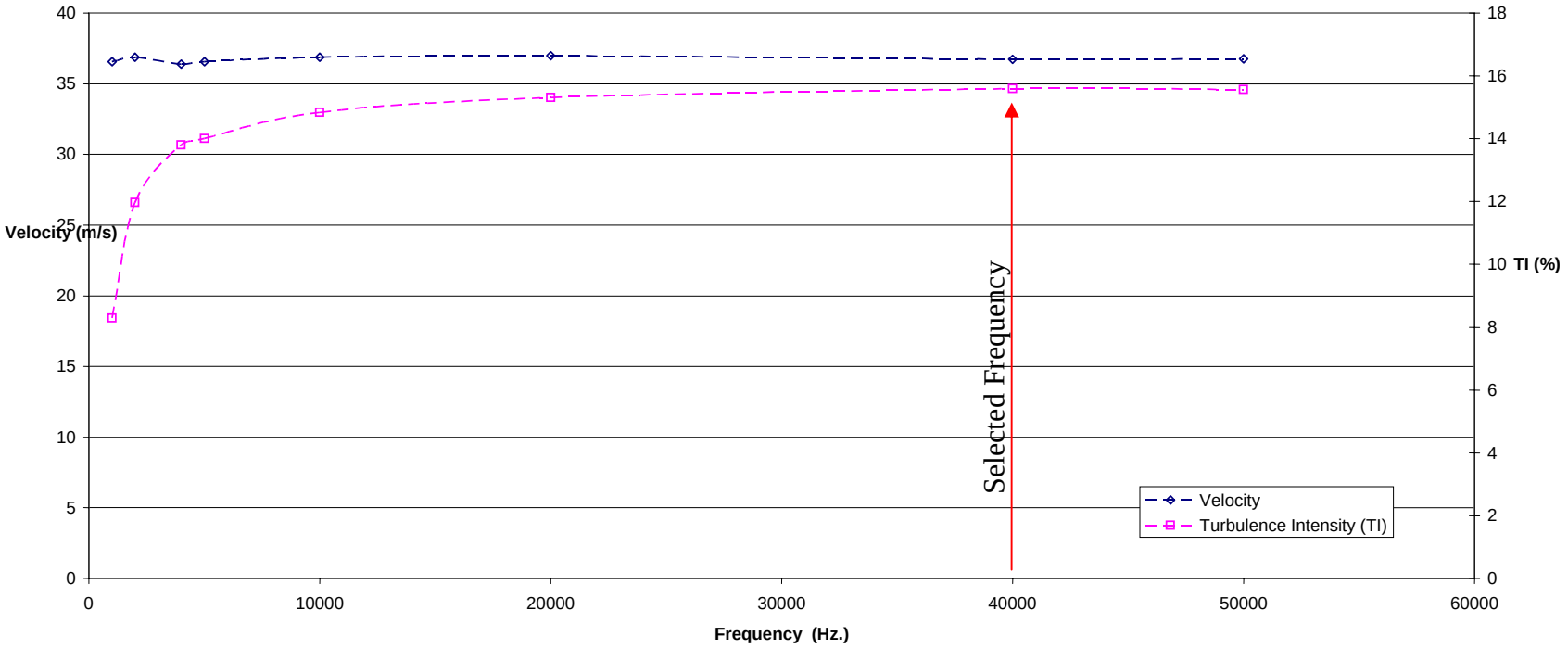

Figure A-6
Velocity and Turbulence Intensity as a Function of Sampling Frequency at a Horizontal Position of 3.0 Inches

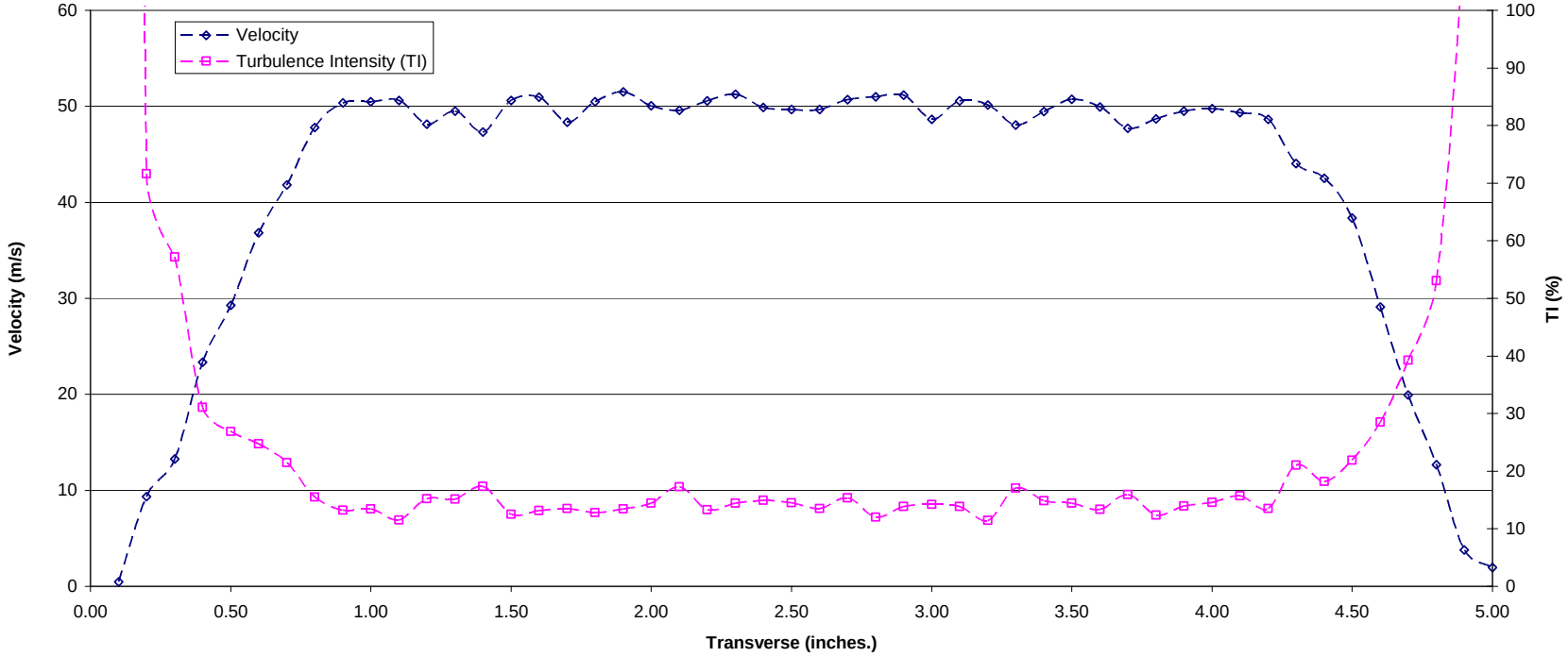

Figure A-7
Transverse Velocity Profile at a Horizontal Position of 3.0 Inches (30 Degree Die – 2 psig Back Pressure)

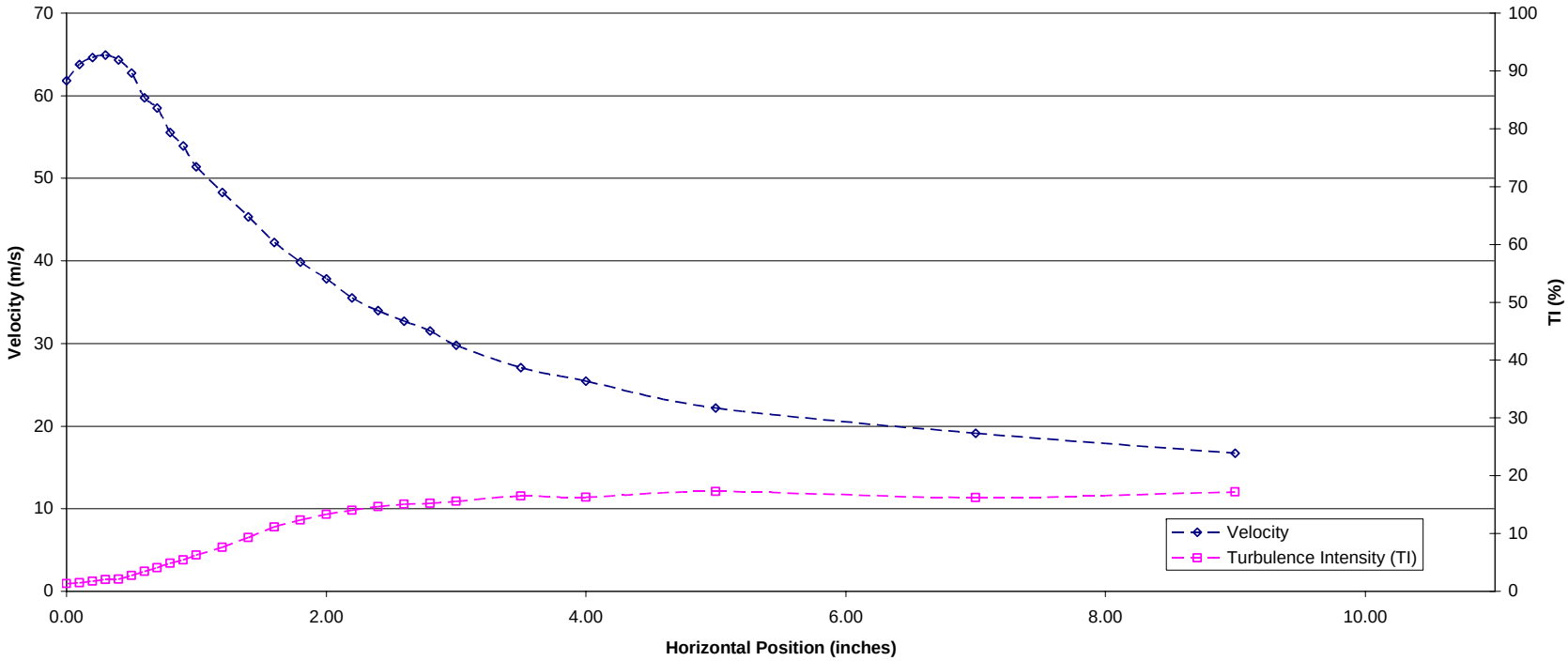

Figure A-8
Centerline Velocity and Turbulence Intensity (30 Degree Die – 2 psig Back Pressure)

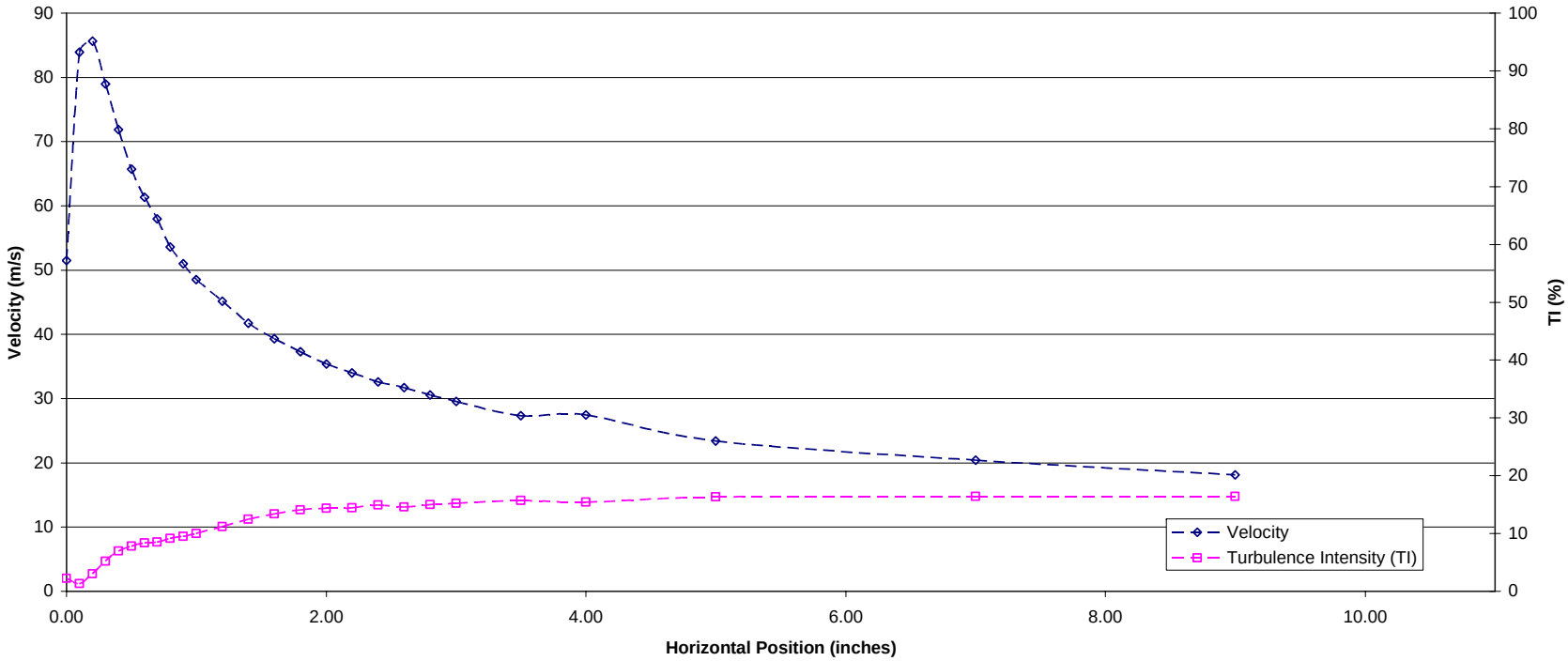

Figure A-9
Centerline Velocity and Turbulence Intensity (60 Degree Die – 2 psig Back Pressure)

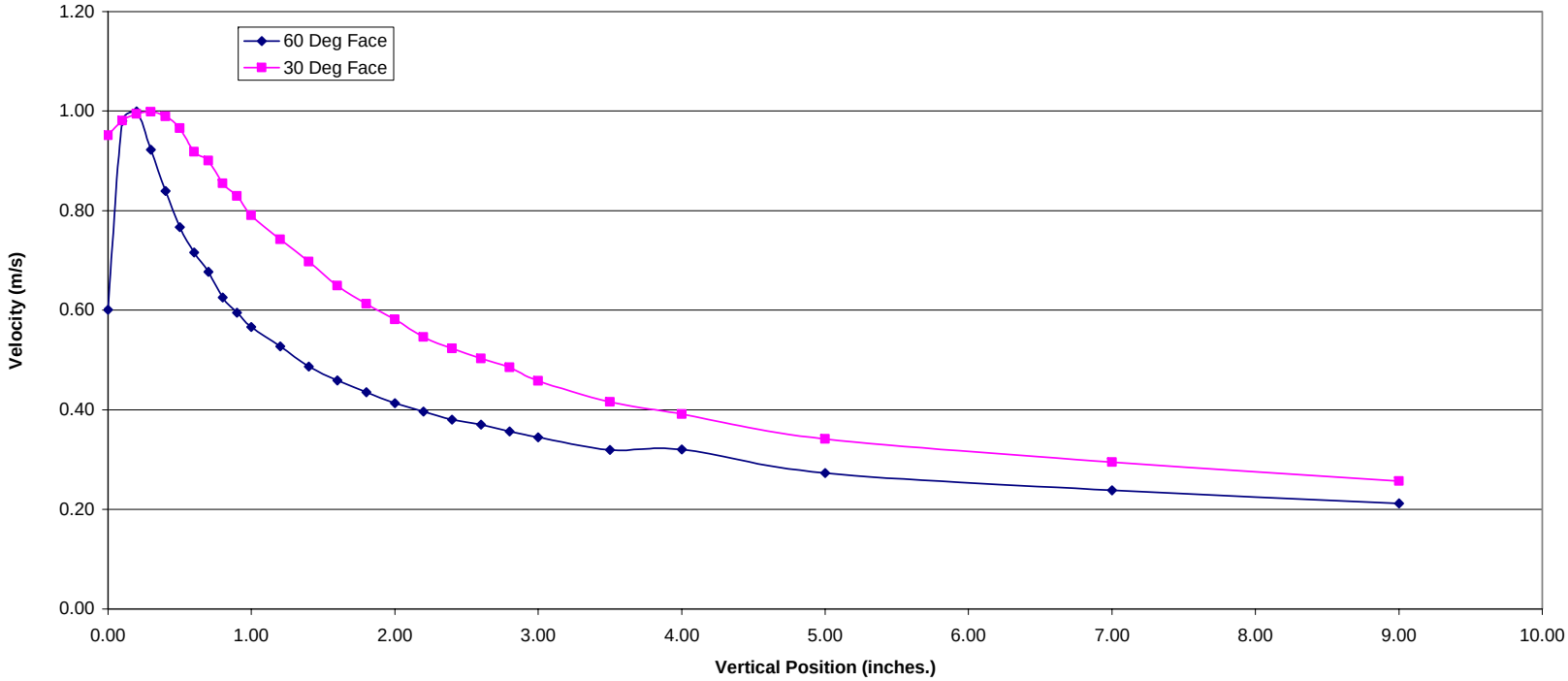

Figure A-10
Normalized Centerline Velocity

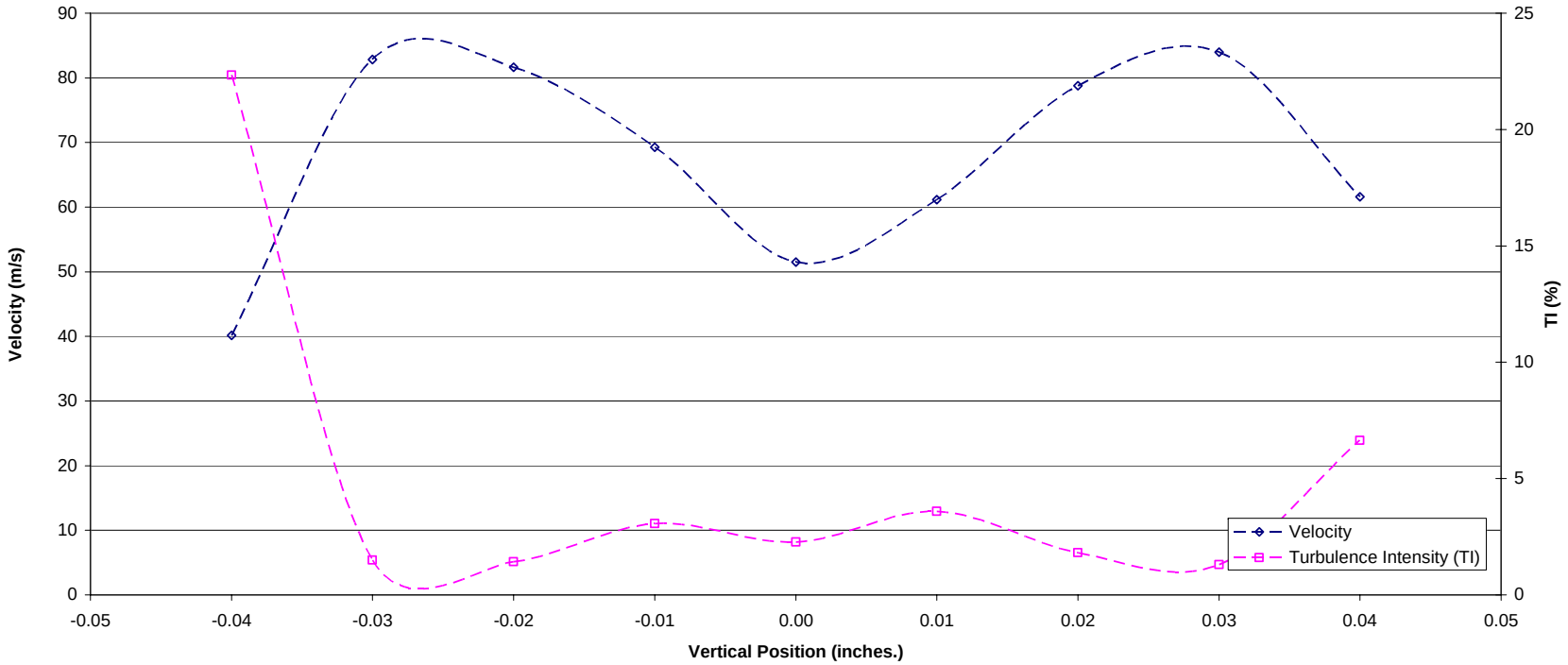

Figure A-11
Velocity and Turbulence Intensity as a Function of Vertical Position at a Horizontal Position of 0 Inches
(60 Degree Die – 2 psig Back Pressure)

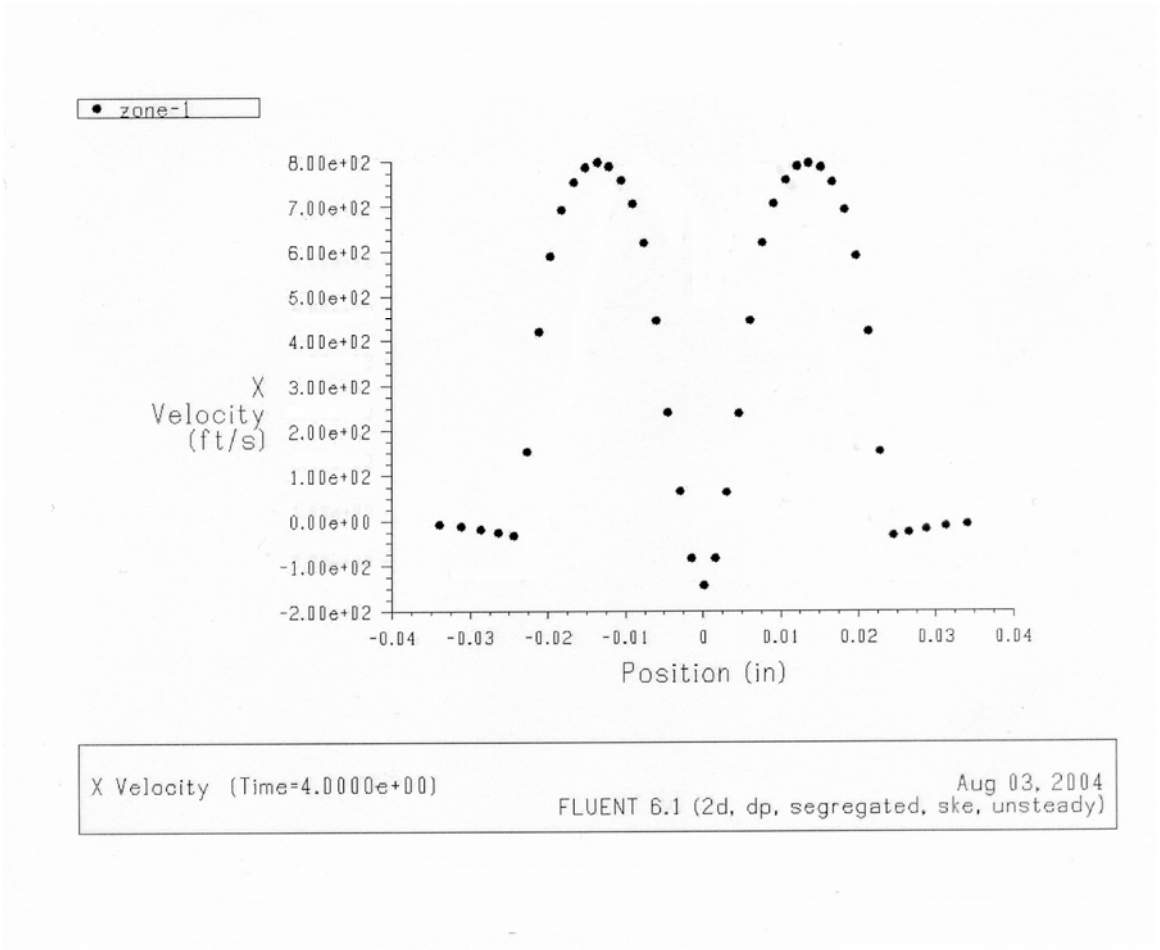

Figure A-12
FLUENT Simulation (30 Degree Die – 10 psig Back Pressure) [3]

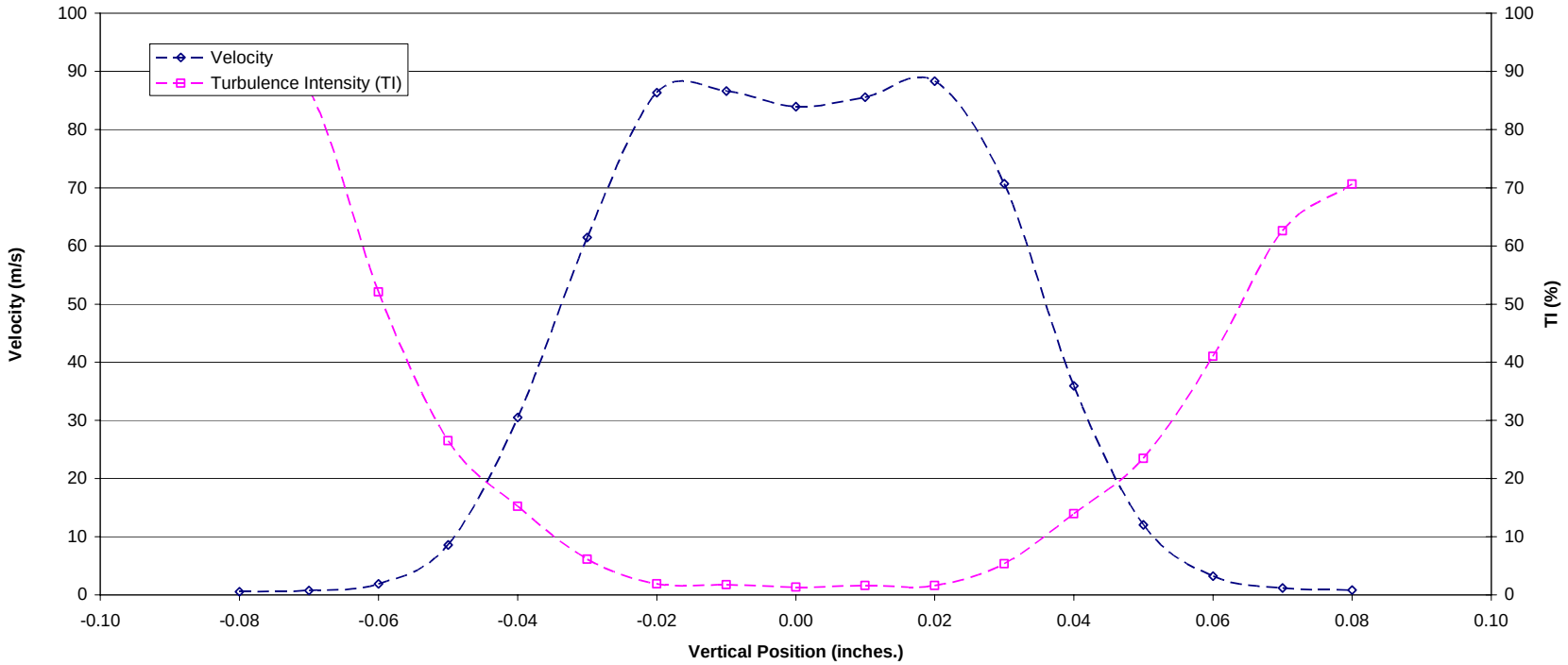

Figure A-13
Velocity and Turbulence Intensity as a Function of Vertical Position at a Horizontal Position of .1 Inches
(60 Degree Die – 2 psig Back Pressure)

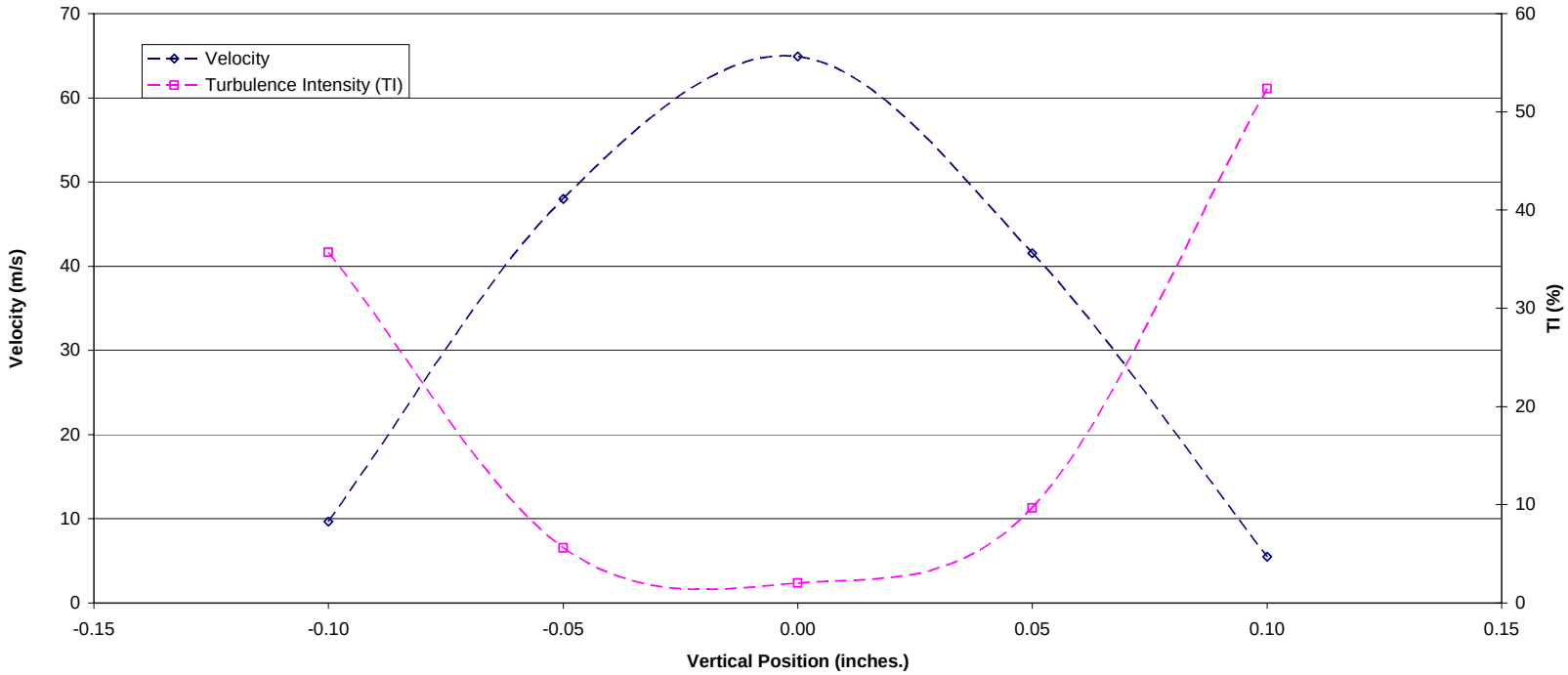

Figure A-14
Velocity and Turbulence Intensity as a Function of Vertical Position at a Horizontal Position of 3.0 Inches
(30 Degree Die – 2 psig Back Pressure)

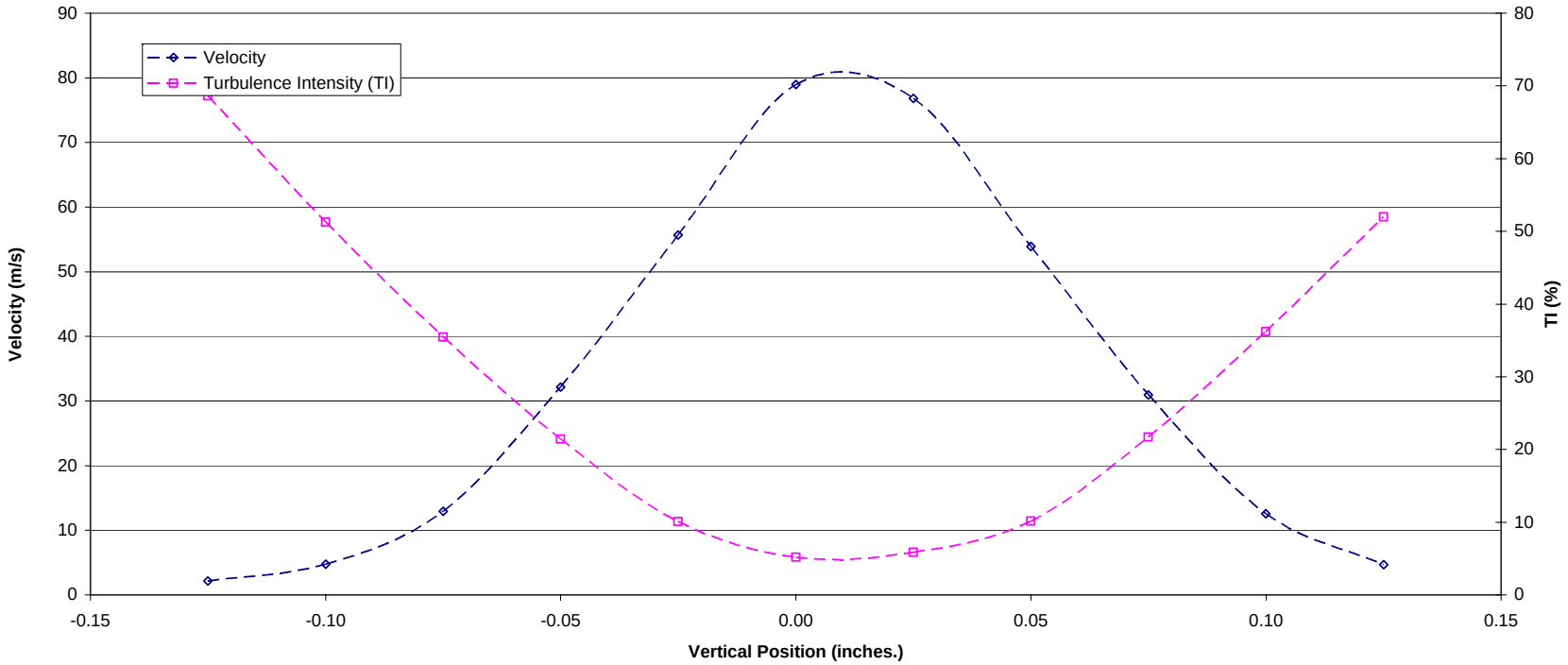

Figure A-15
Velocity and Turbulence Intensity as a Function of Vertical Position at a Horizontal Position of 3.0 Inches
(60 Degree Die – 2 psig Back Pressure)

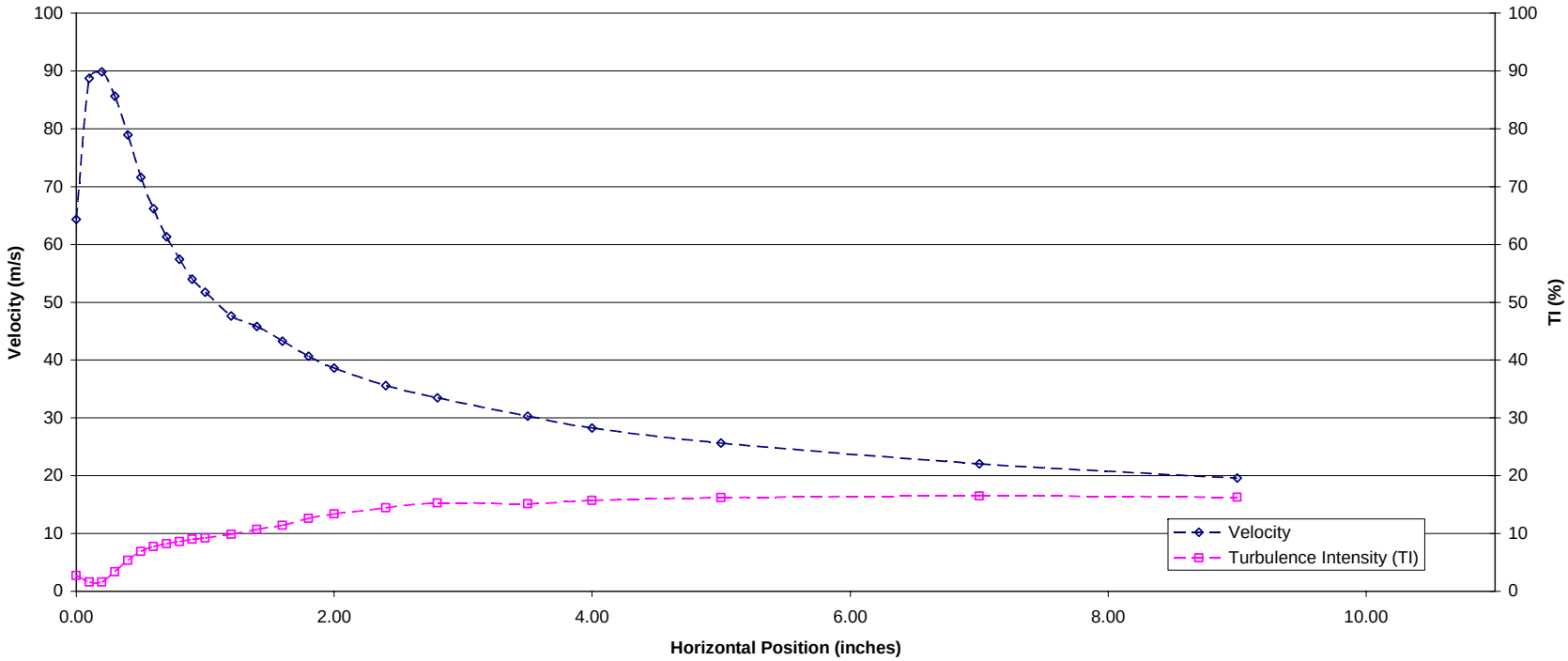

Figure A-16
Centerline Velocity (60 Degree Die – 2.125 psig Back Pressure)

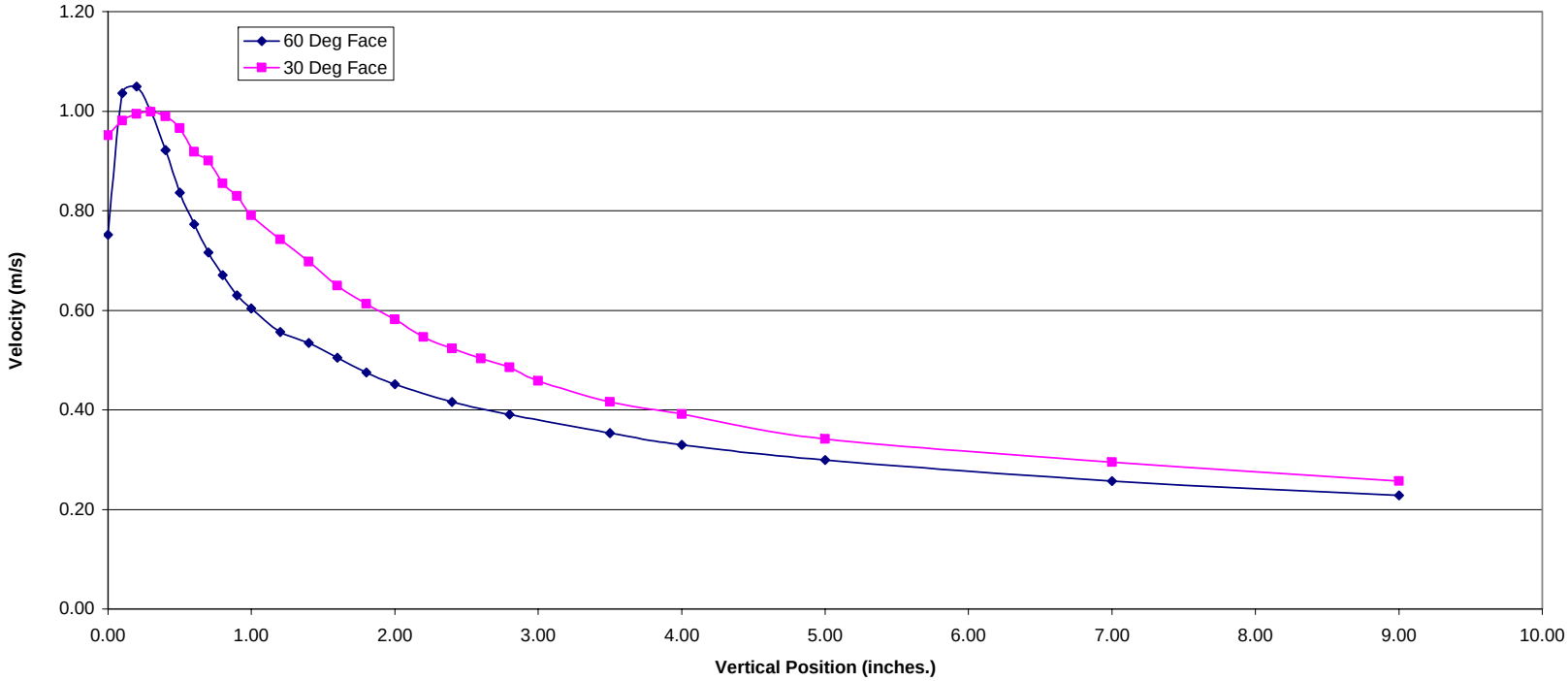

Figure A-17
Normalized Centerline Velocity (Matched Case)

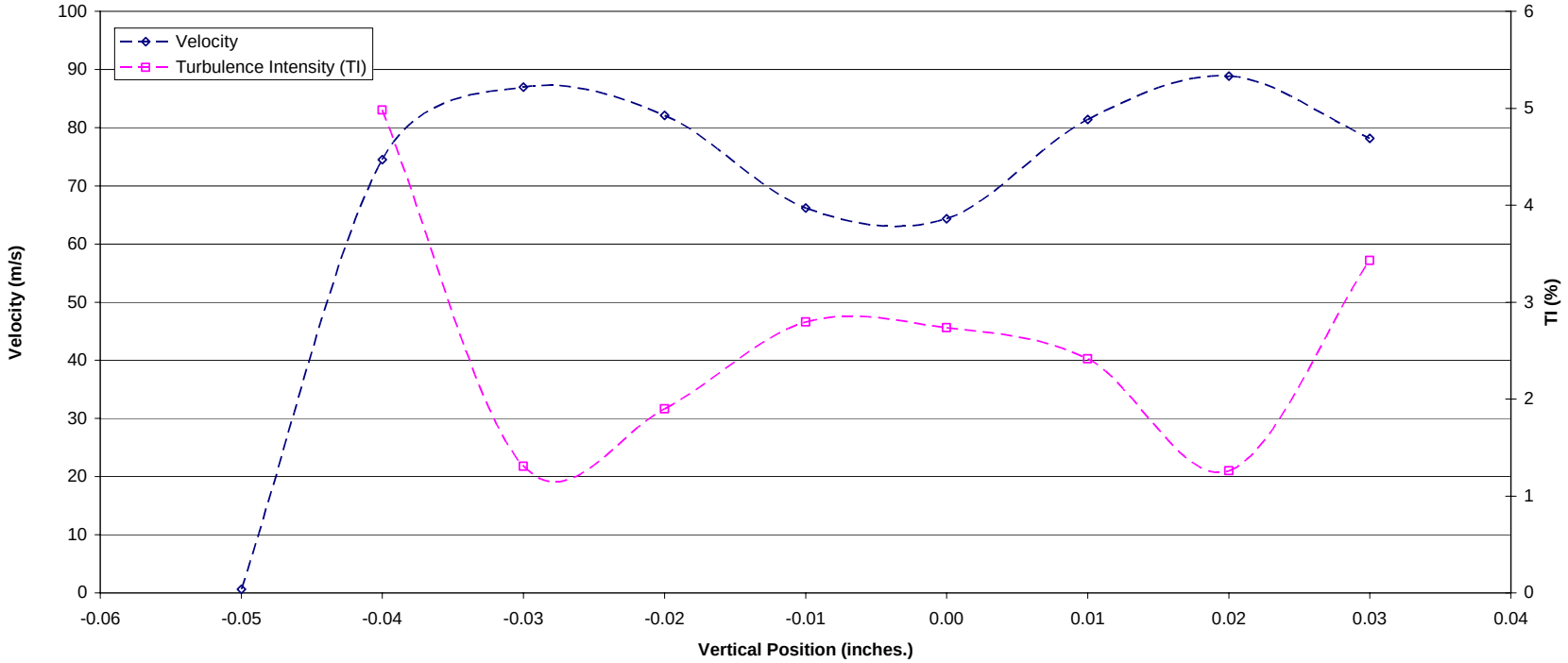

Figure A-18
Velocity and Turbulence Intensity as a Function of Vertical Position at a Horizontal Position of 0 Inches
(60 Degree Die – 2.125 psig Back Pressure)

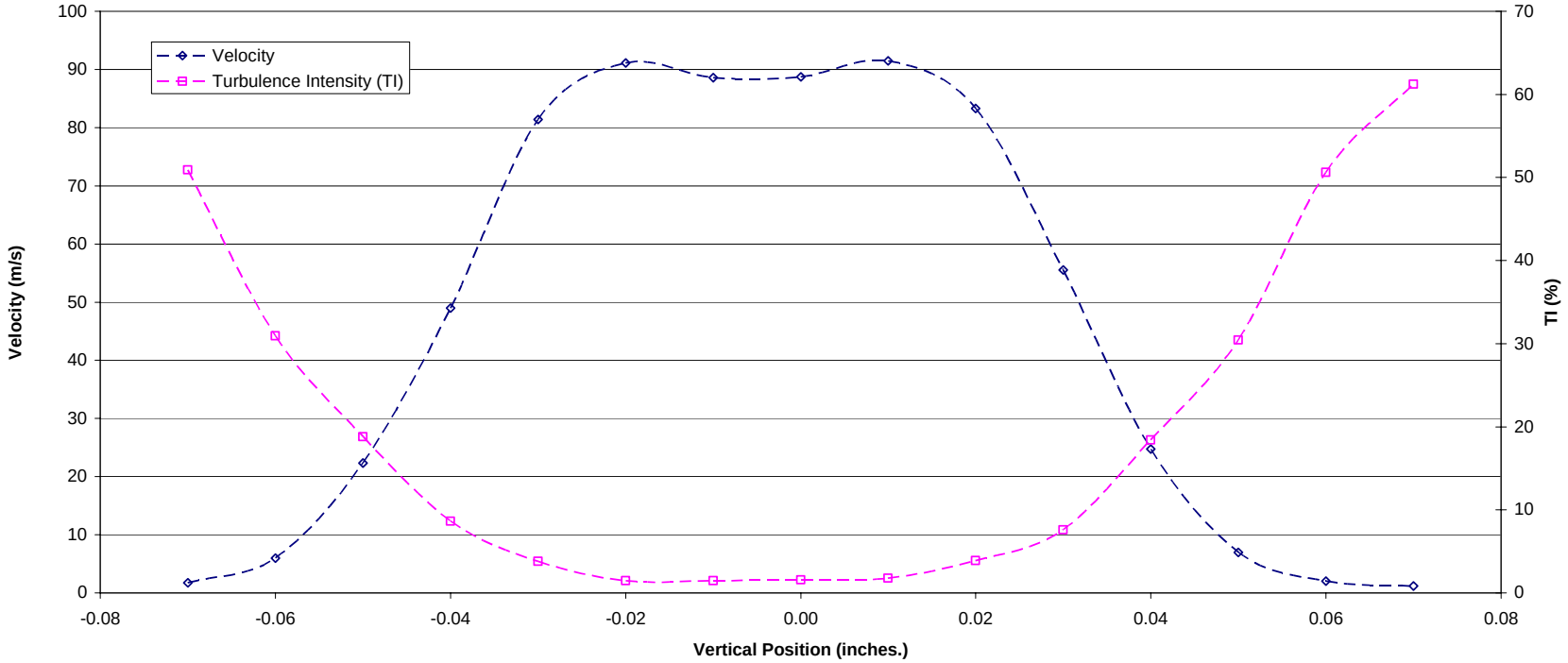

Figure A-19
Velocity and Turbulence Intensity as a Function of Vertical Position at a Horizontal Position of 0.1 Inches
(60 Degree Die – 2.125 psig Back Pressure)

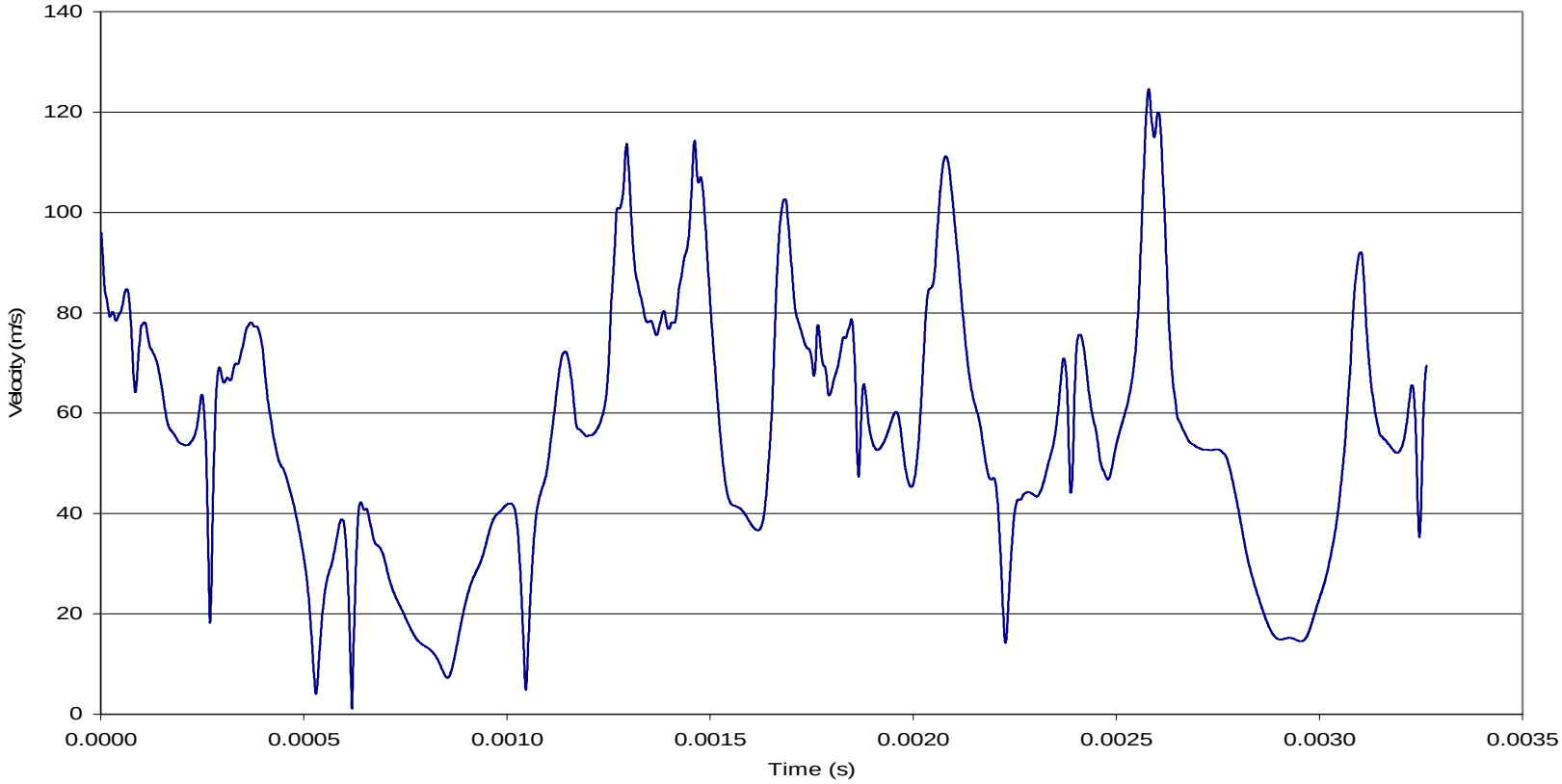

Figure A-20
CFD Time Dependent Velocity at a Horizontal Centerline Position of 1.0 Inches
(60 Degree Die – 2 psig Back Pressure) [4]

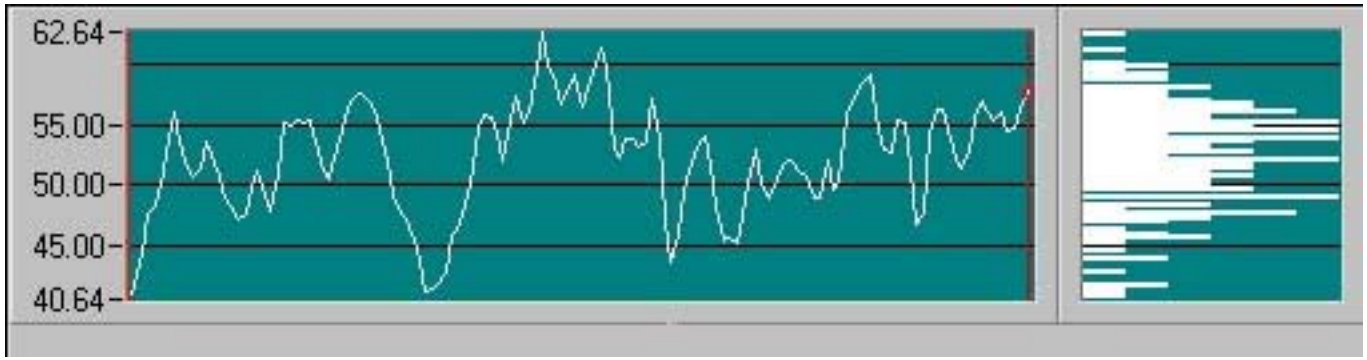

Figure A-21
Experimental Time Dependent Velocity at a Horizontal Centerline Position of 1 Inch
(60 Degree Die – 2 psig Back Pressure)

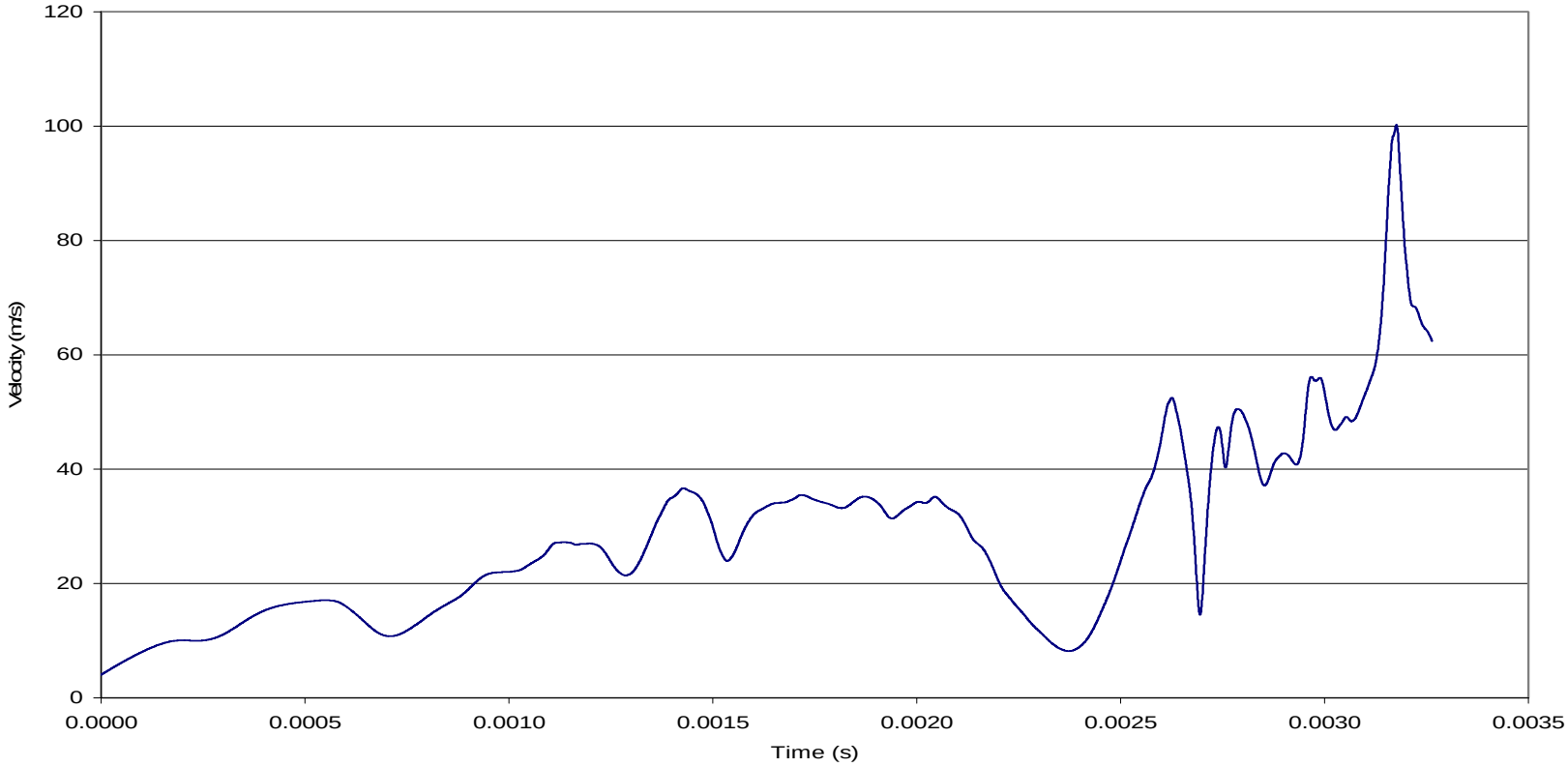

Figure A-22
CFD Time Dependent Velocity at a Horizontal Centerline Position of 2 Inches
(60 Degree Die – 2 psig Back Pressure) [4]

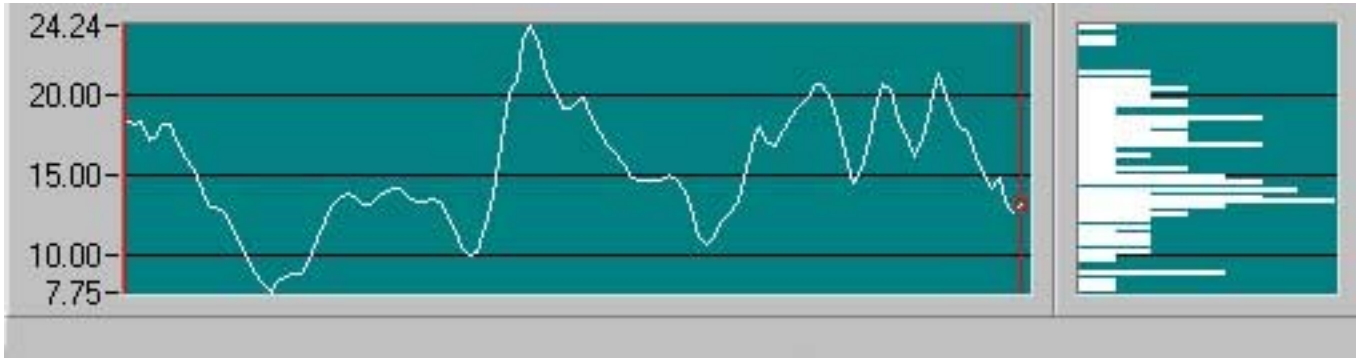

Figure A-23
Experimental Time Dependent Velocity at a Horizontal Centerline Position of 2 Inches
(60 Degree Die – 2 psig Back Pressure)

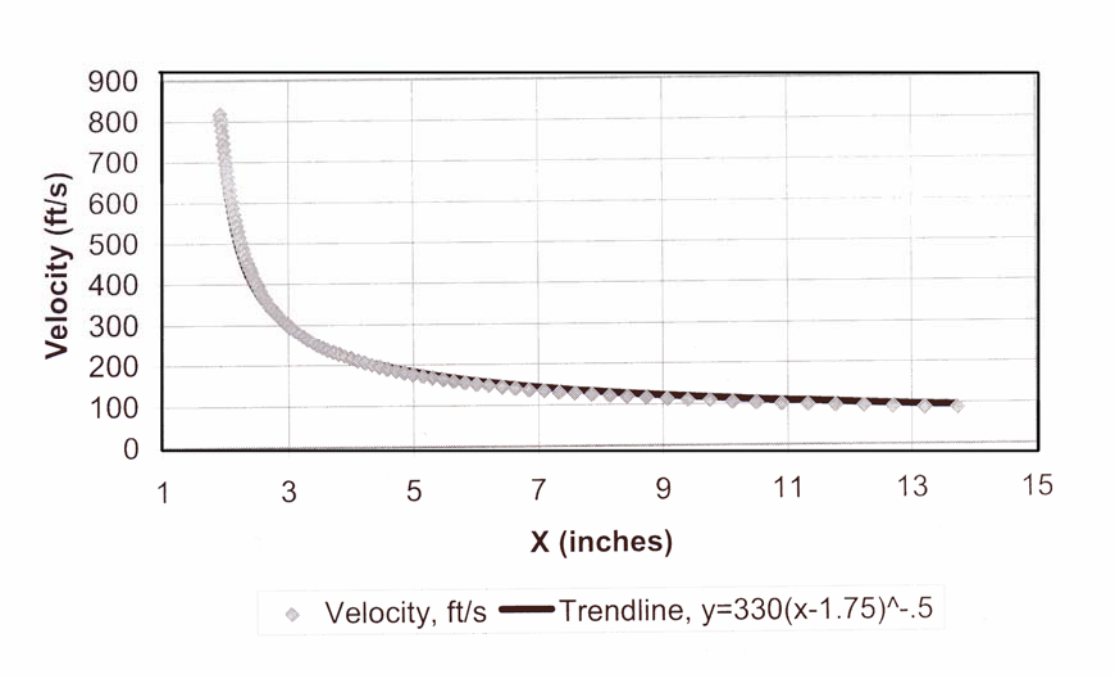

Figure A-24
CFD Centerline Velocity Curve Fit
(30 Degree Die – 10 psig Back Pressure) [3]

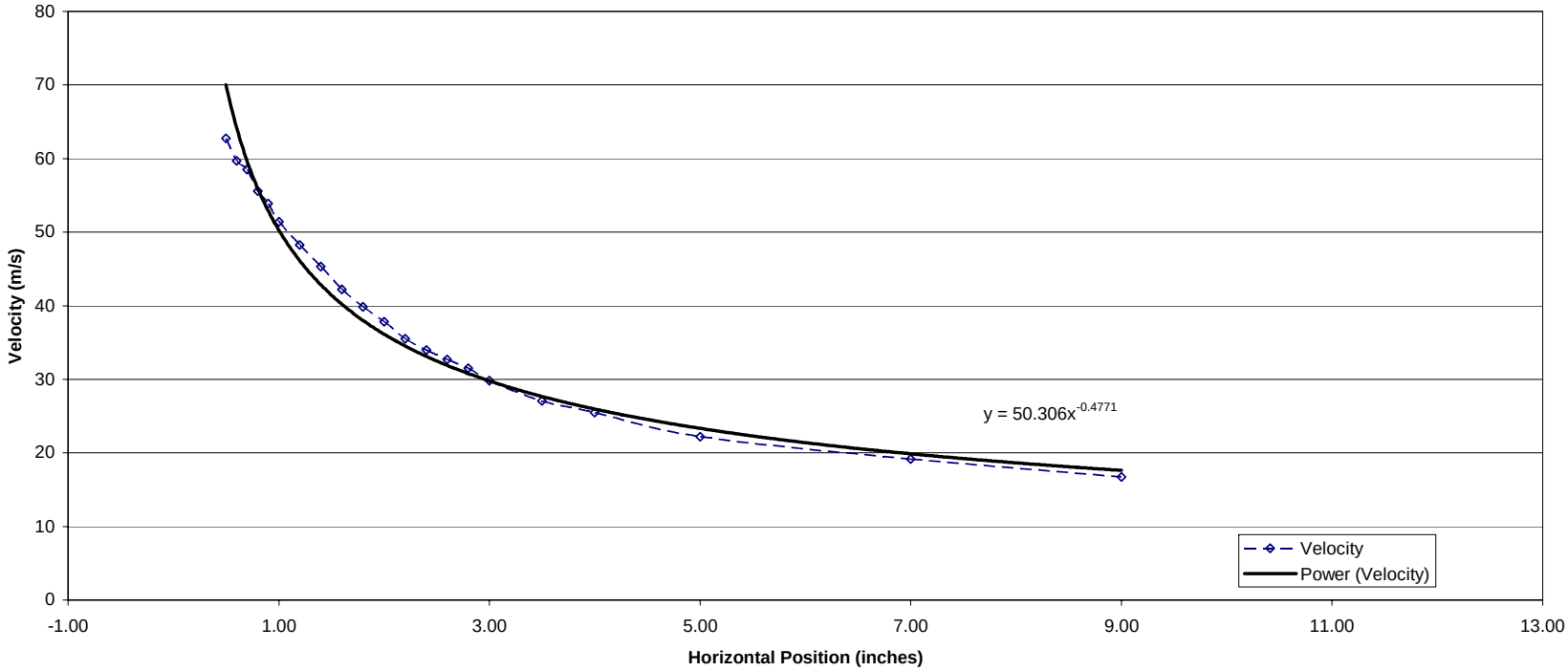

Figure A-25
Experimental Centerline Velocity Curve Fit
(30 Degree Die – 2 psig Back Pressure)

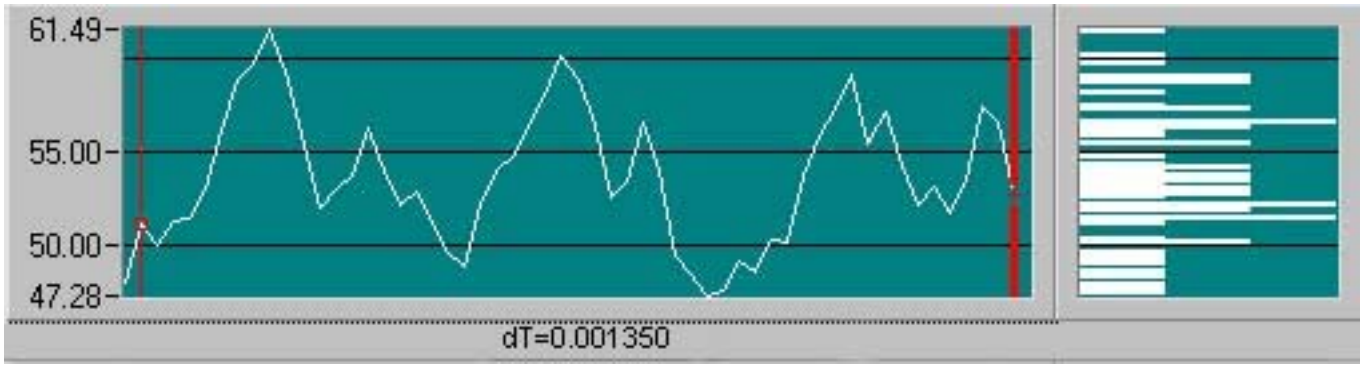

Figure A-26
Experimental Time Dependent Velocity at a Horizontal Centerline Position of 1 Inches
(60 Degree Die – 2 psig Back Pressure)

APPENDIX B: SUPPLEMENTAL FIGURES

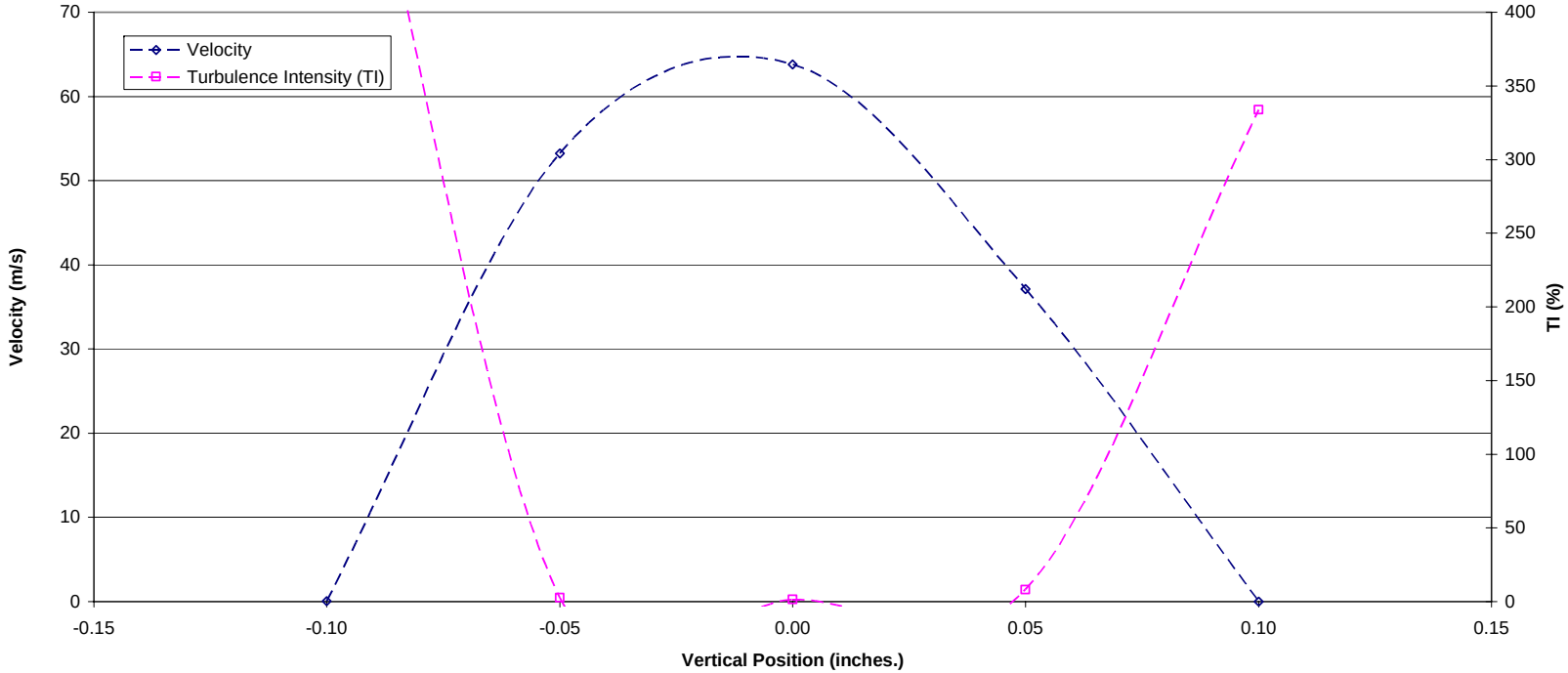

Figure B-1
Velocity and Turbulence Intensity as a Function of Vertical Position at a Horizontal Position of .1 Inches
(30 Degree Die – 2 psig Back Pressure)

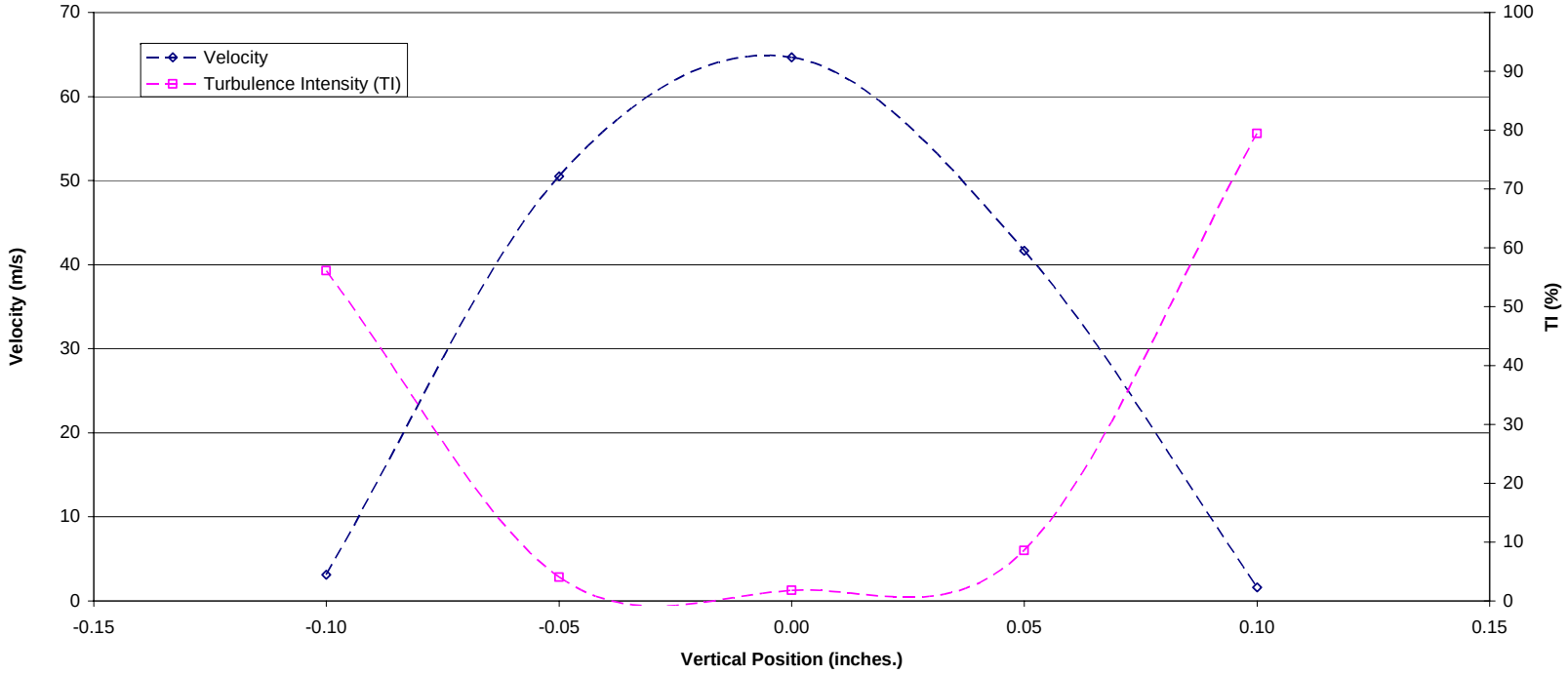

Figure B-2
Velocity and Turbulence Intensity as a Function of Vertical Position at a Horizontal Position of .2 Inches (30 Degree Die – 2 psig Back Pressure)

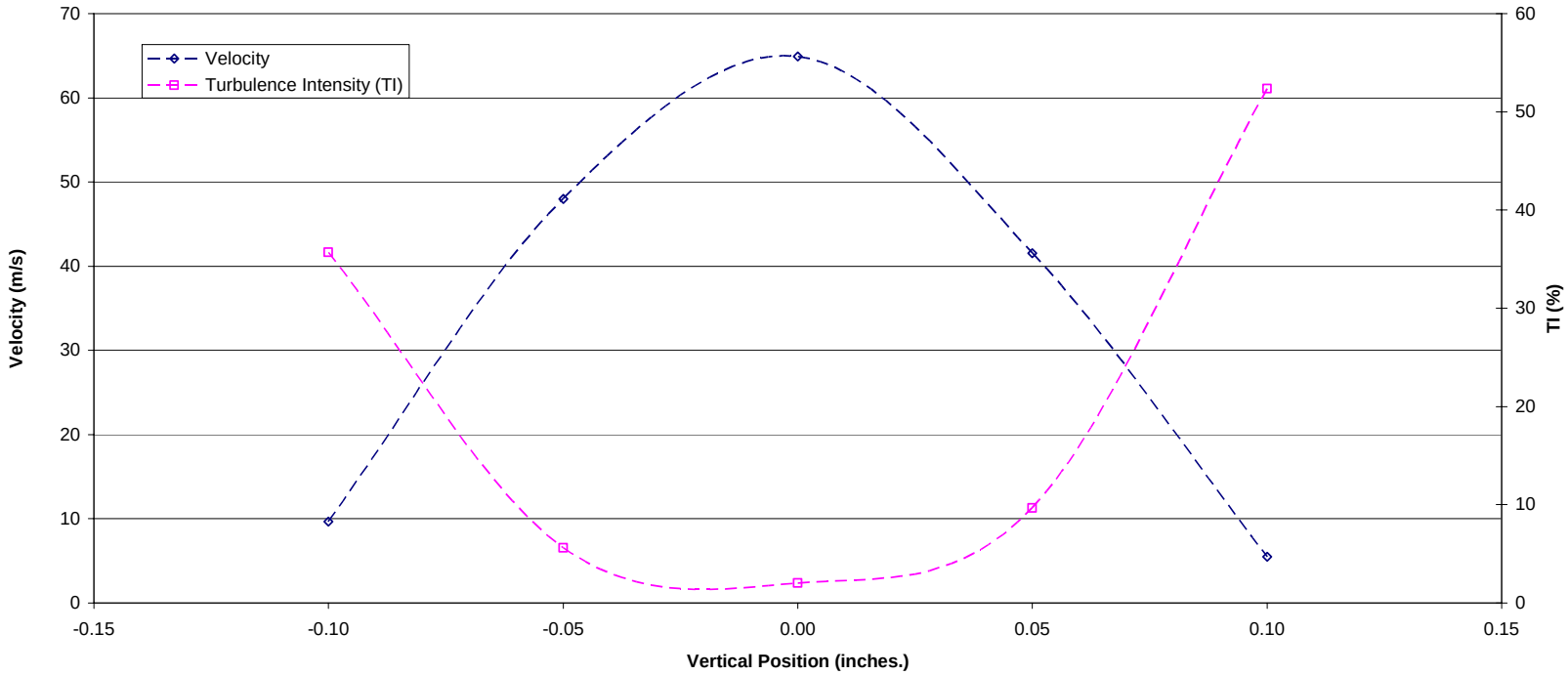

Figure B-3
Velocity and Turbulence Intensity as a Function of Vertical Position at a Horizontal Position of .3 Inches
(30 Degree Die – 2 psig Back Pressure)

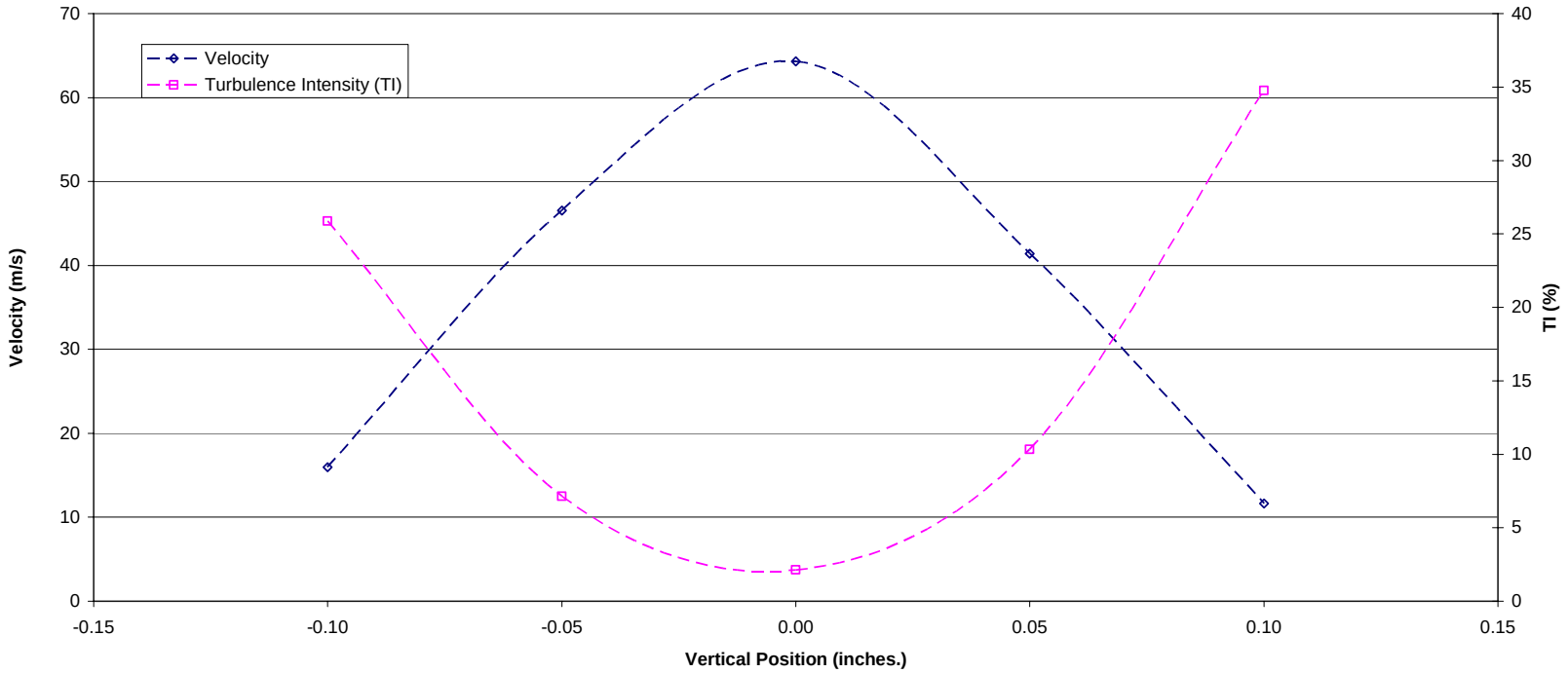

Figure B-4
Velocity and Turbulence Intensity as a Function of Vertical Position at a Horizontal Position of .4 Inches
(30 Degree Die – 2 psig Back Pressure)

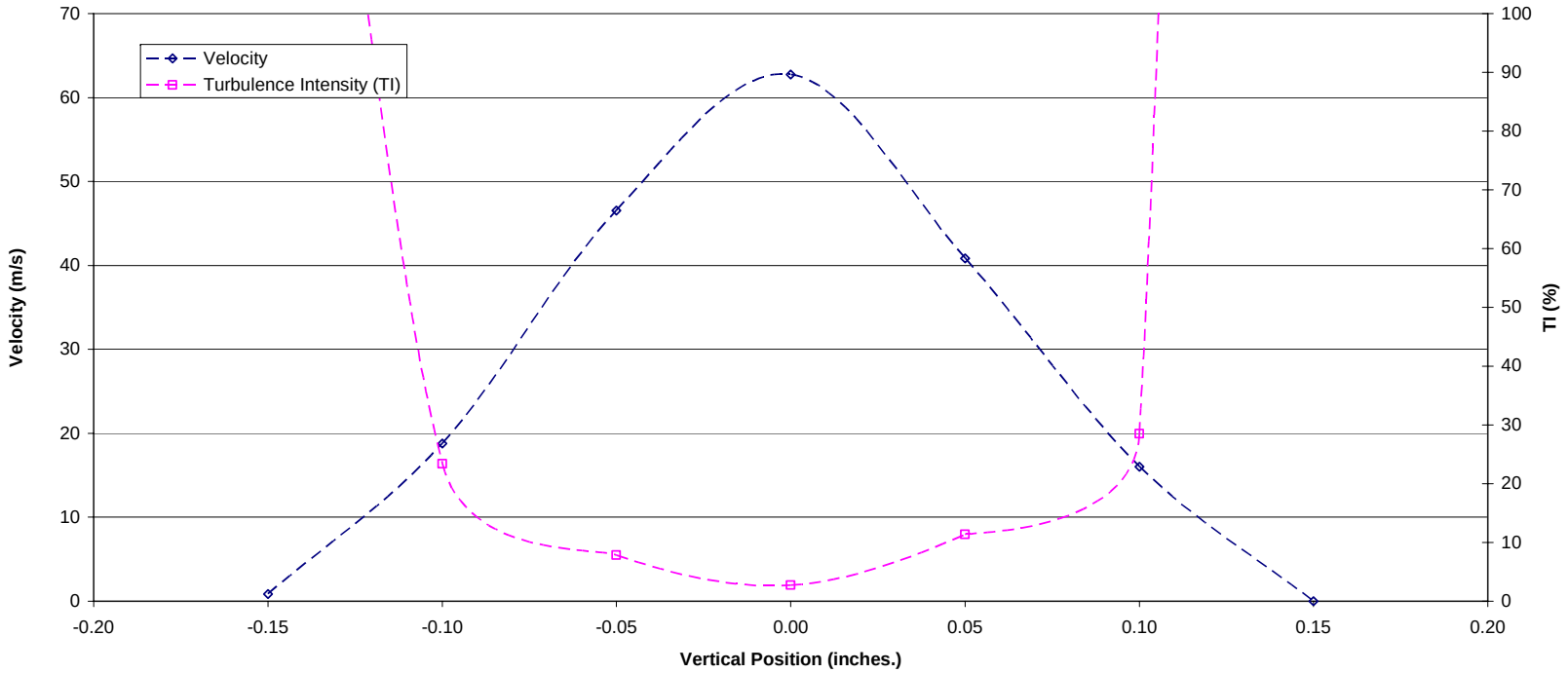

Figure B-5
Velocity and Turbulence Intensity as a Function of Vertical Position at a Horizontal Position of .5 Inches
(30 Degree Die – 2 psig Back Pressure)

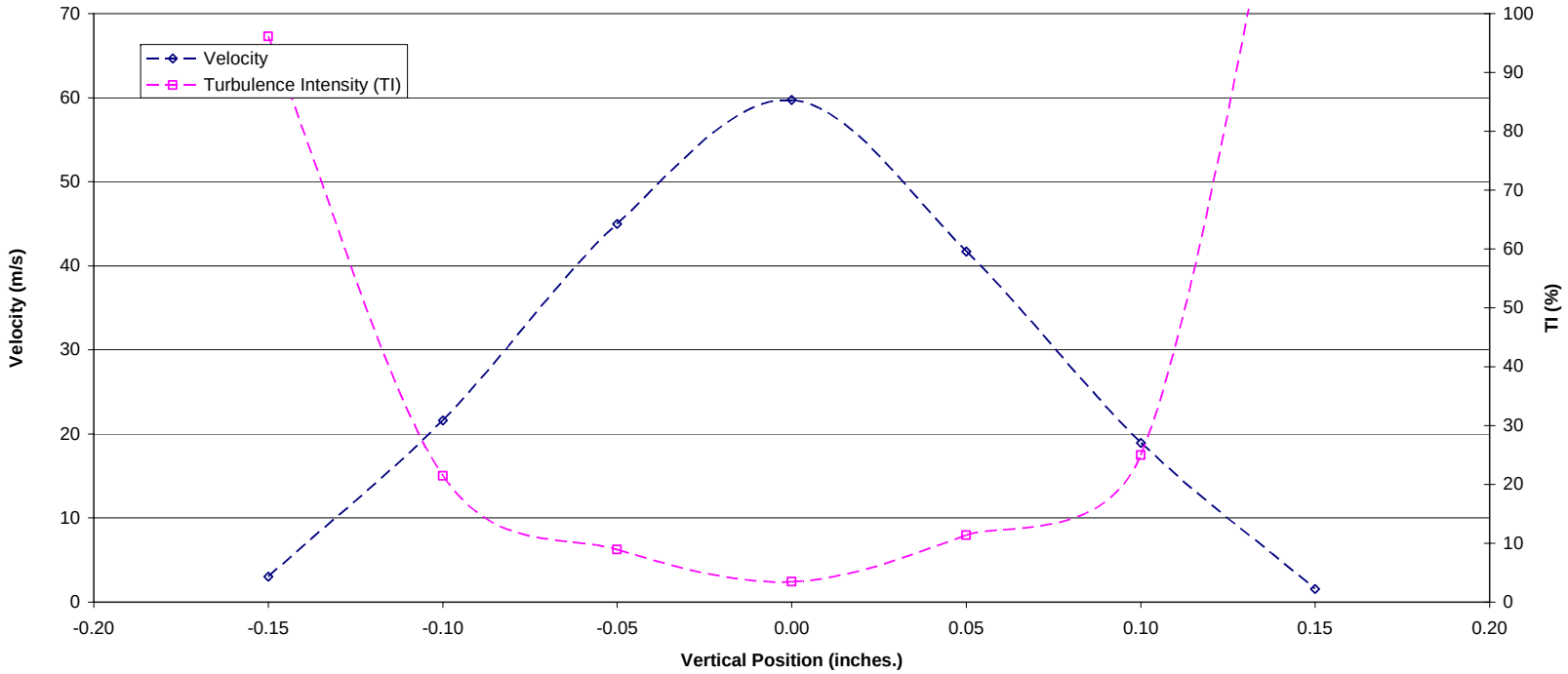

Figure B-6
Velocity and Turbulence Intensity as a Function of Vertical Position at a Horizontal Position of .6 Inches
(30 Degree Die – 2 psig Back Pressure)

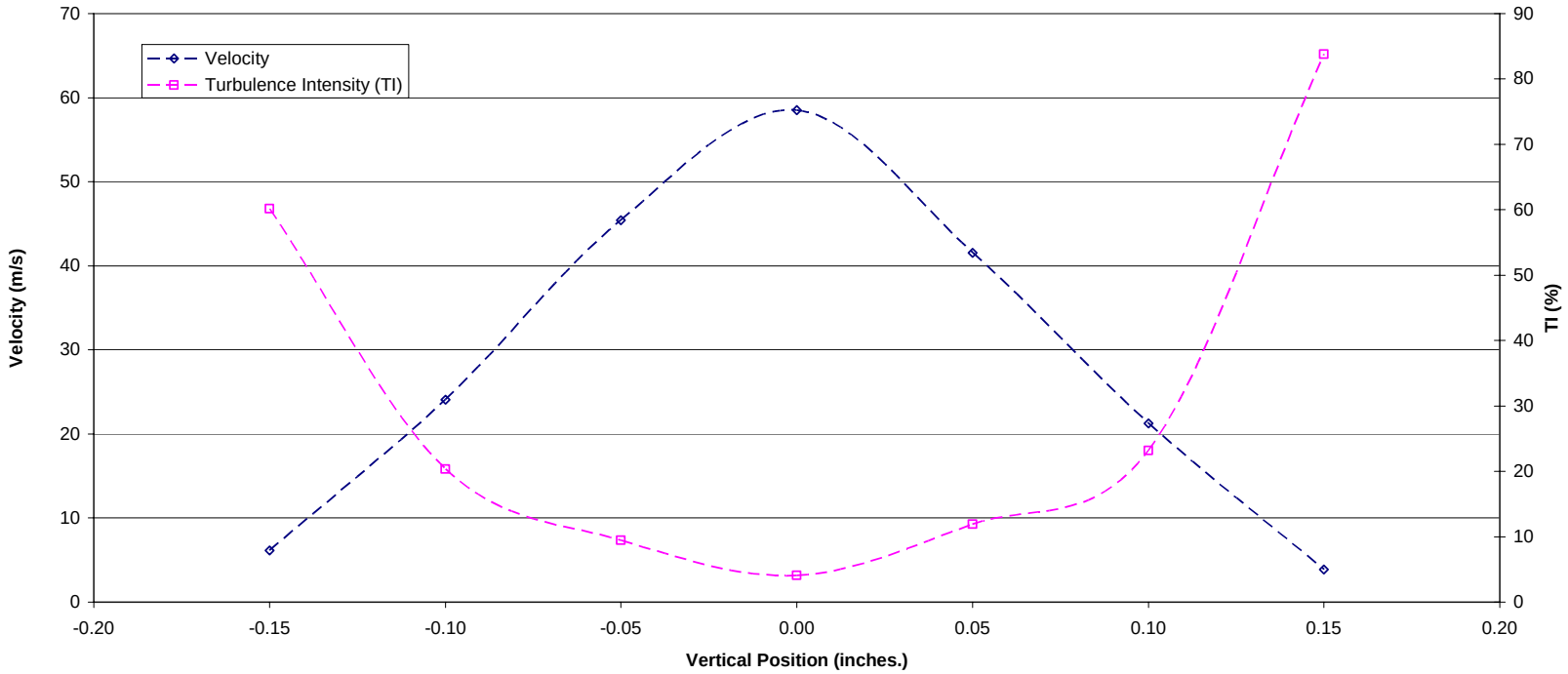

Figure B-7
Velocity and Turbulence Intensity as a Function of Vertical Position at a Horizontal Position of .7 Inches
(30 Degree Die – 2 psig Back Pressure)

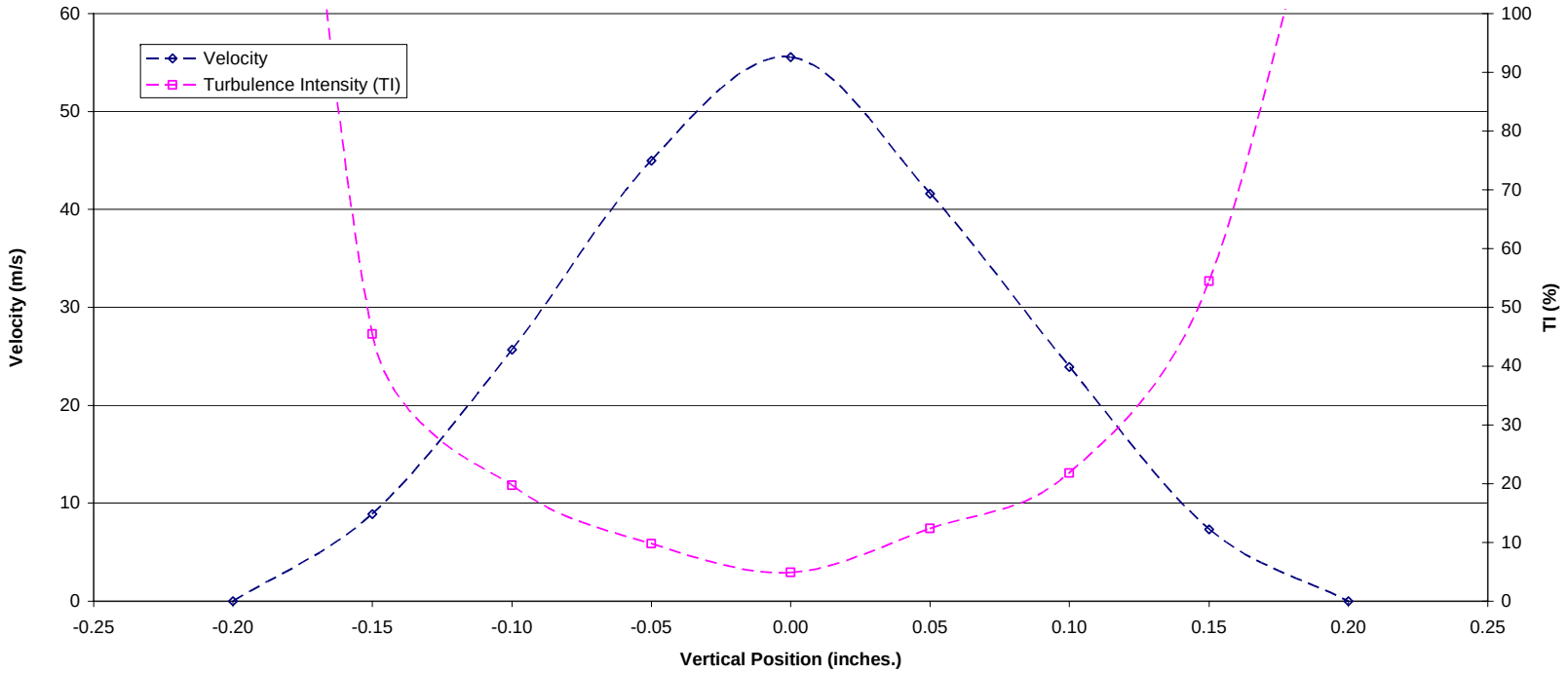

Figure B-8
Velocity and Turbulence Intensity as a Function of Vertical Position at a Horizontal Position of .8 Inches
(30 Degree Die – 2 psig Back Pressure)

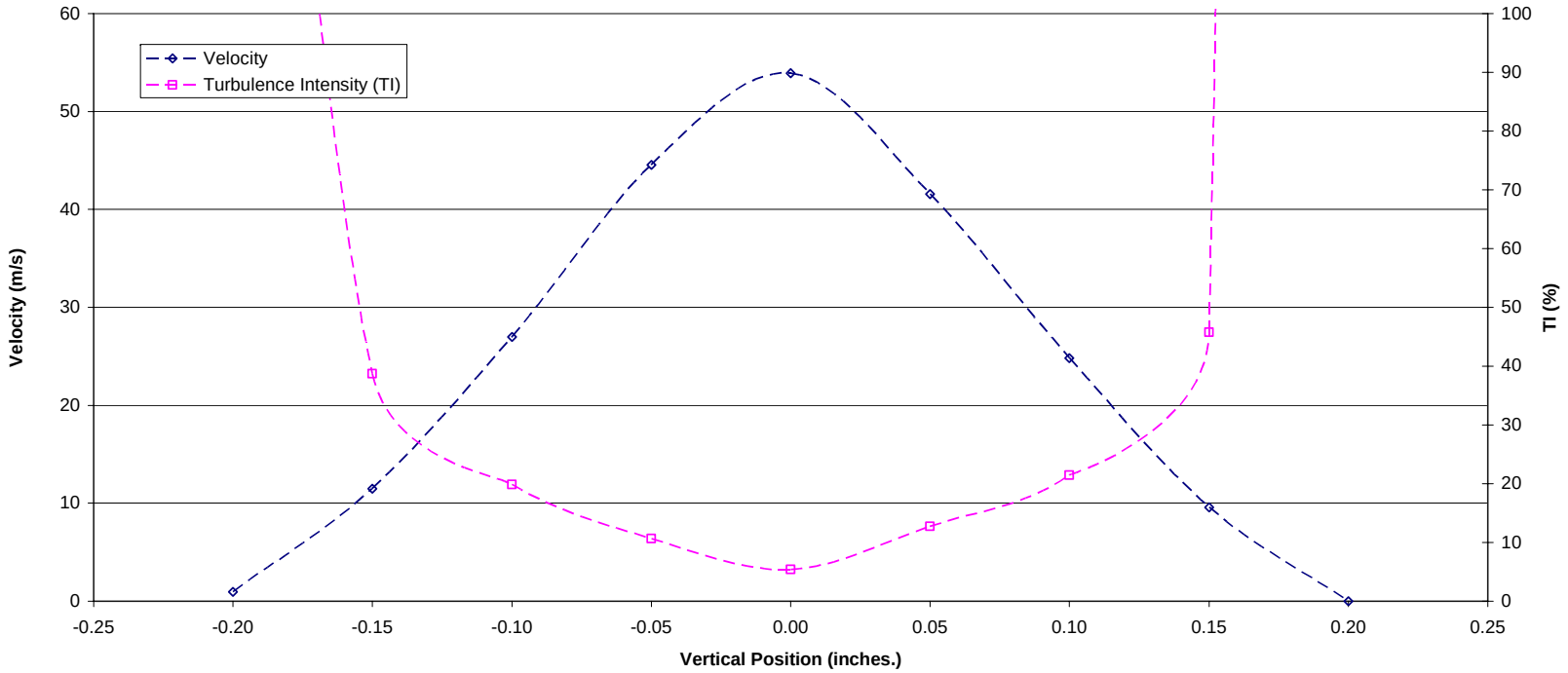

Figure B-9
Velocity and Turbulence Intensity as a Function of Vertical Position at a Horizontal Position of .9 Inches
(30 Degree Die – 2 psig Back Pressure)

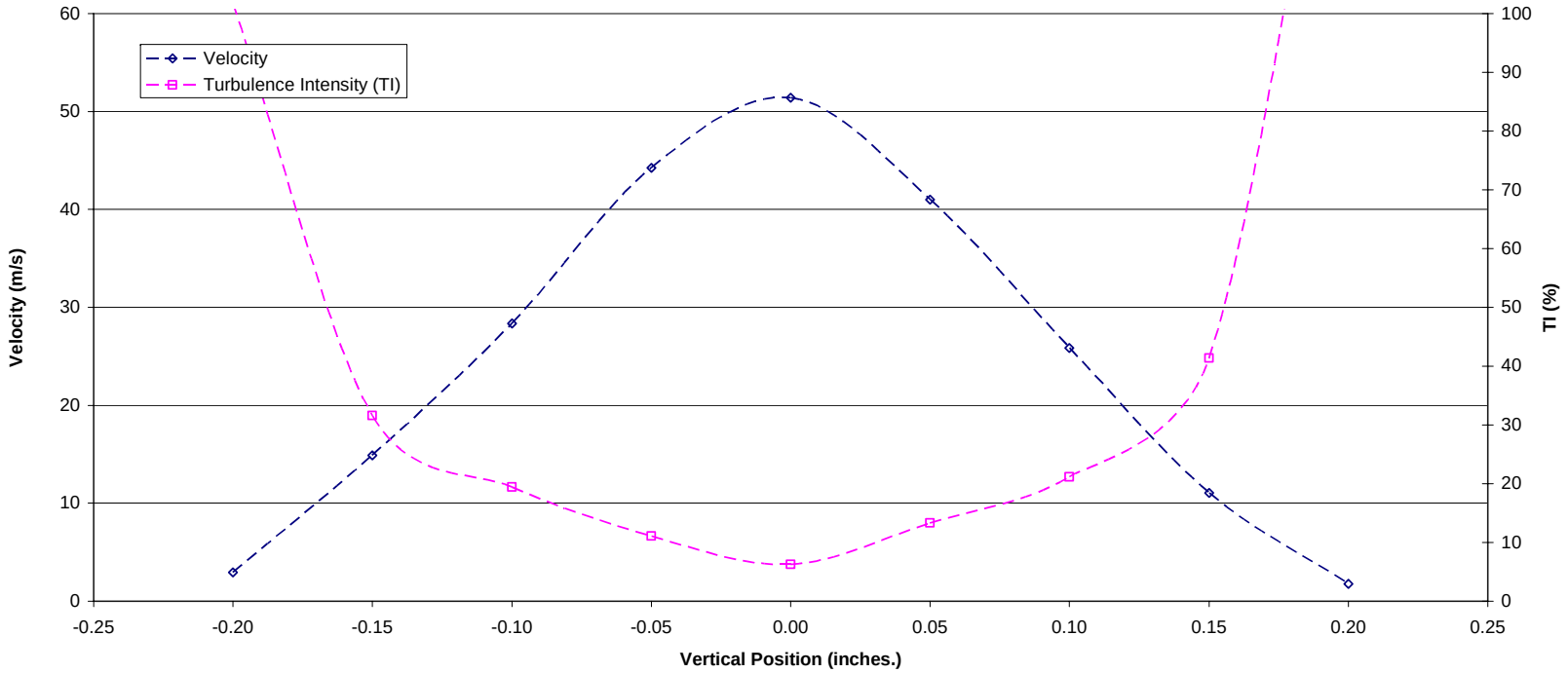

Figure B-10
Velocity and Turbulence Intensity as a Function of Vertical Position at a Horizontal Position of 1.0 Inches
(30 Degree Die – 2 psig Back Pressure)

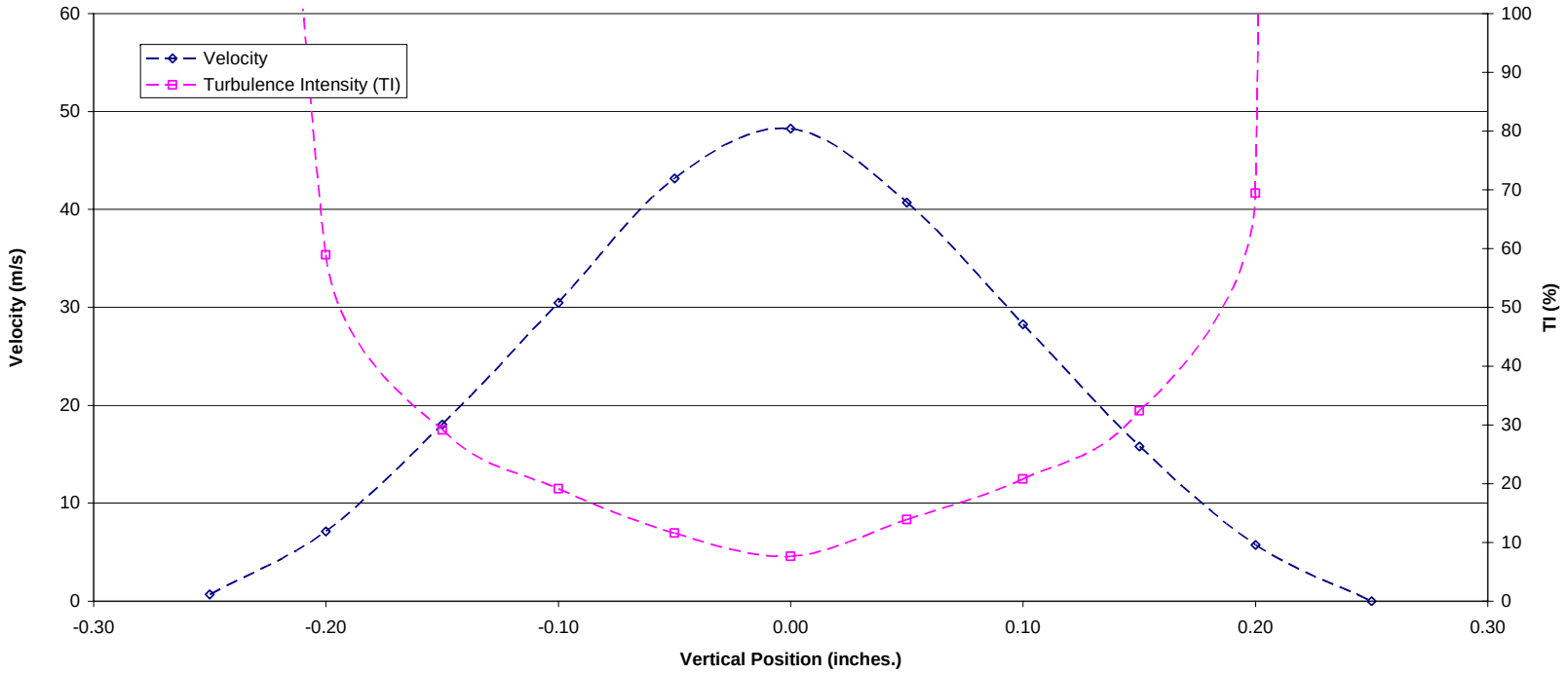

Figure B-11
Velocity and Turbulence Intensity as a Function of Vertical Position at a Horizontal Position of 1.2 Inches
(30 Degree Die – 2 psig Back Pressure)

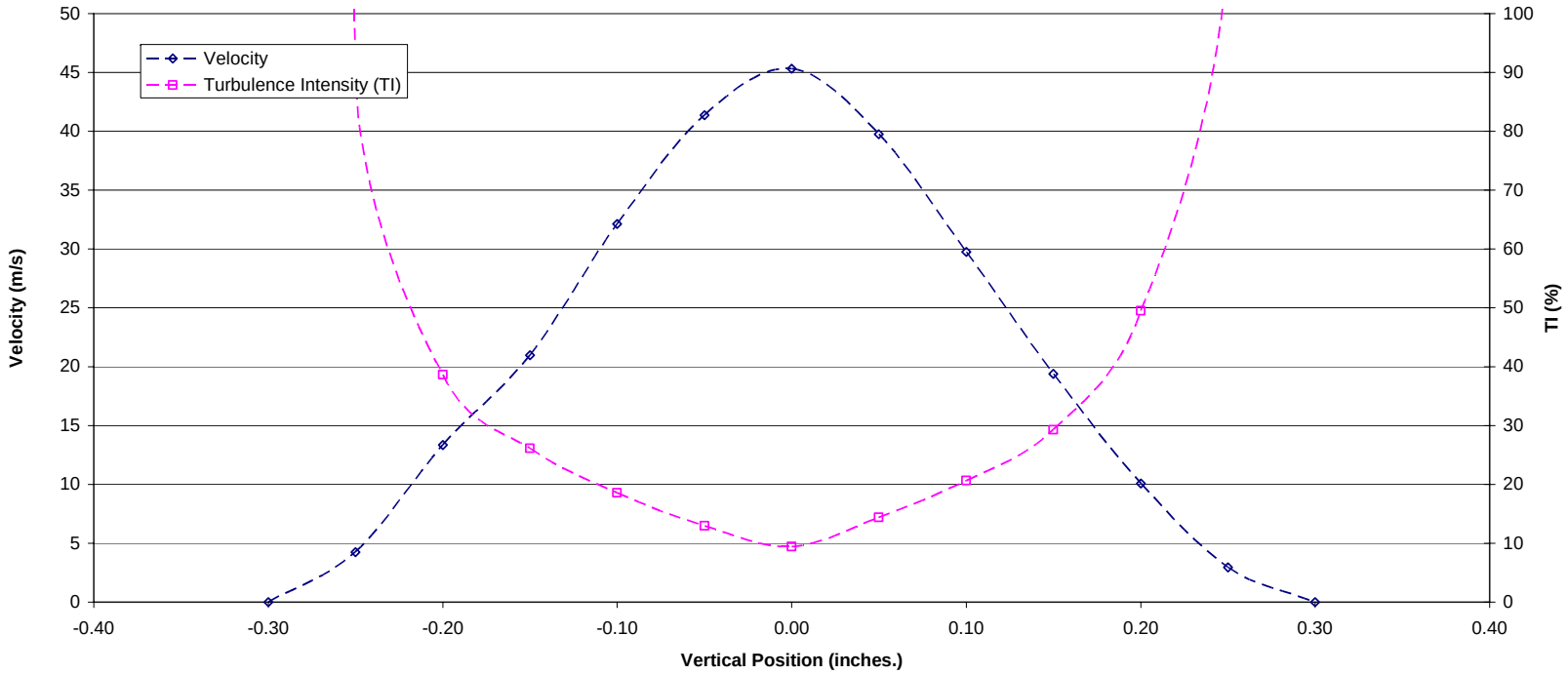

Figure B-12
Velocity and Turbulence Intensity as a Function of Vertical Position at a Horizontal Position of 1.4 Inches
(30 Degree Die – 2 psig Back Pressure)

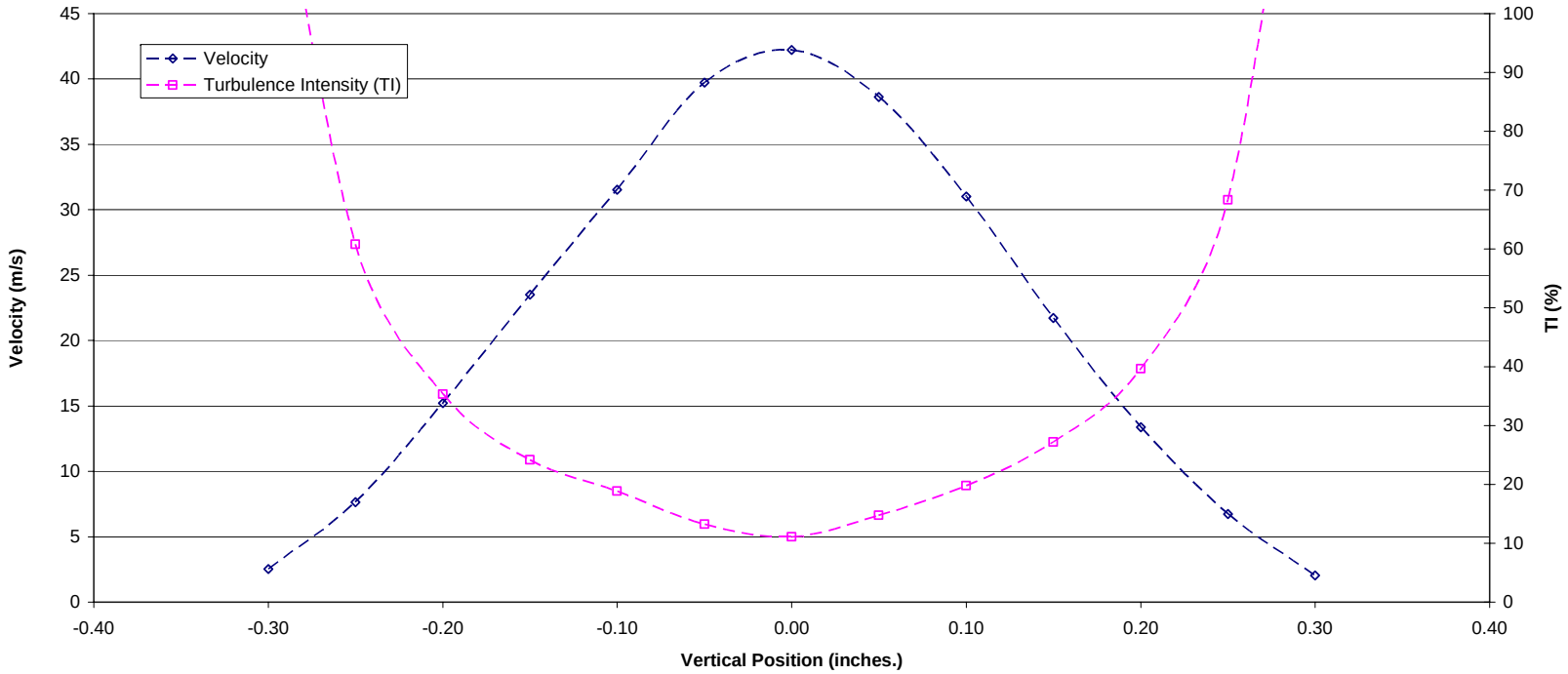

Figure B-13
Velocity and Turbulence Intensity as a Function of Vertical Position at a Horizontal Position of 1.6 Inches
(30 Degree Die – 2 psig Back Pressure)

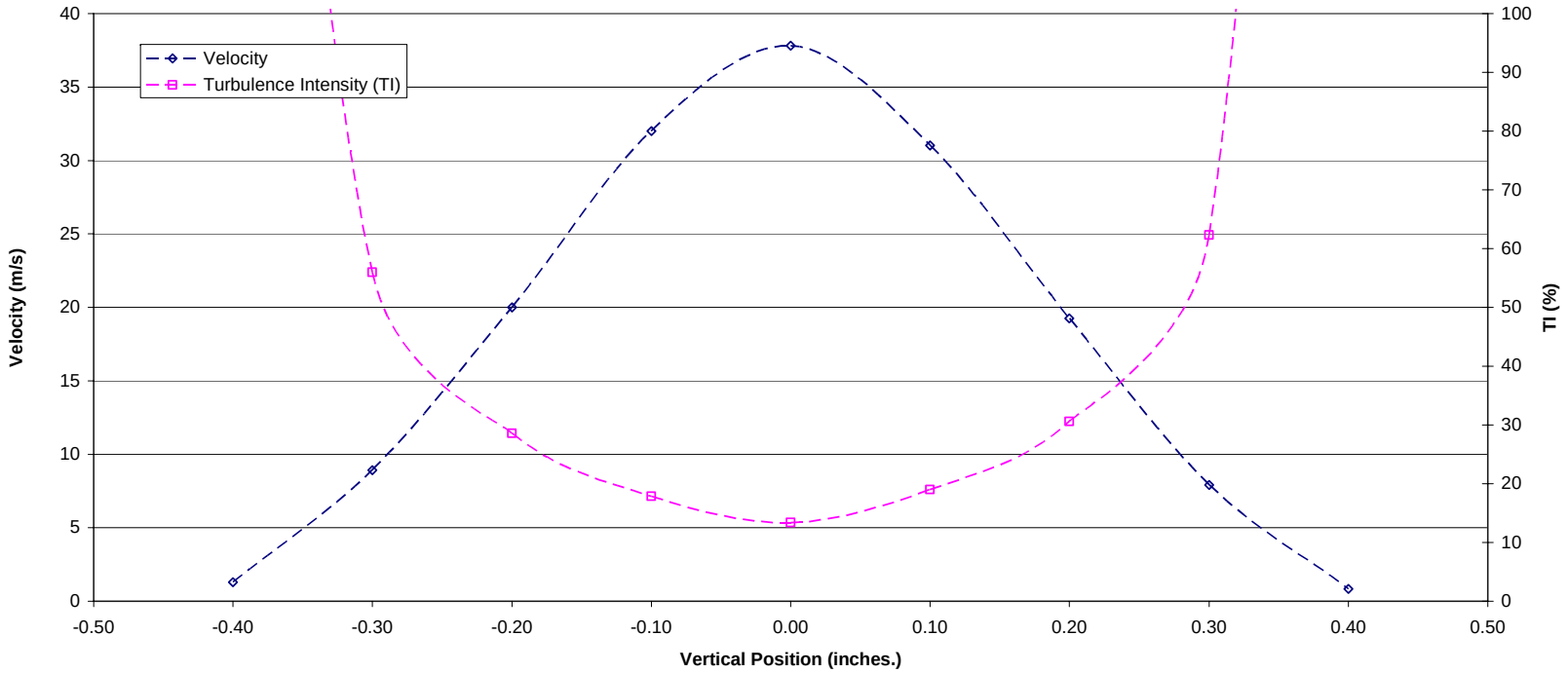

Figure B-14
Velocity and Turbulence Intensity as a Function of Vertical Position at a Horizontal Position of 2.0 Inches
(30 Degree Die – 2 psig Back Pressure)

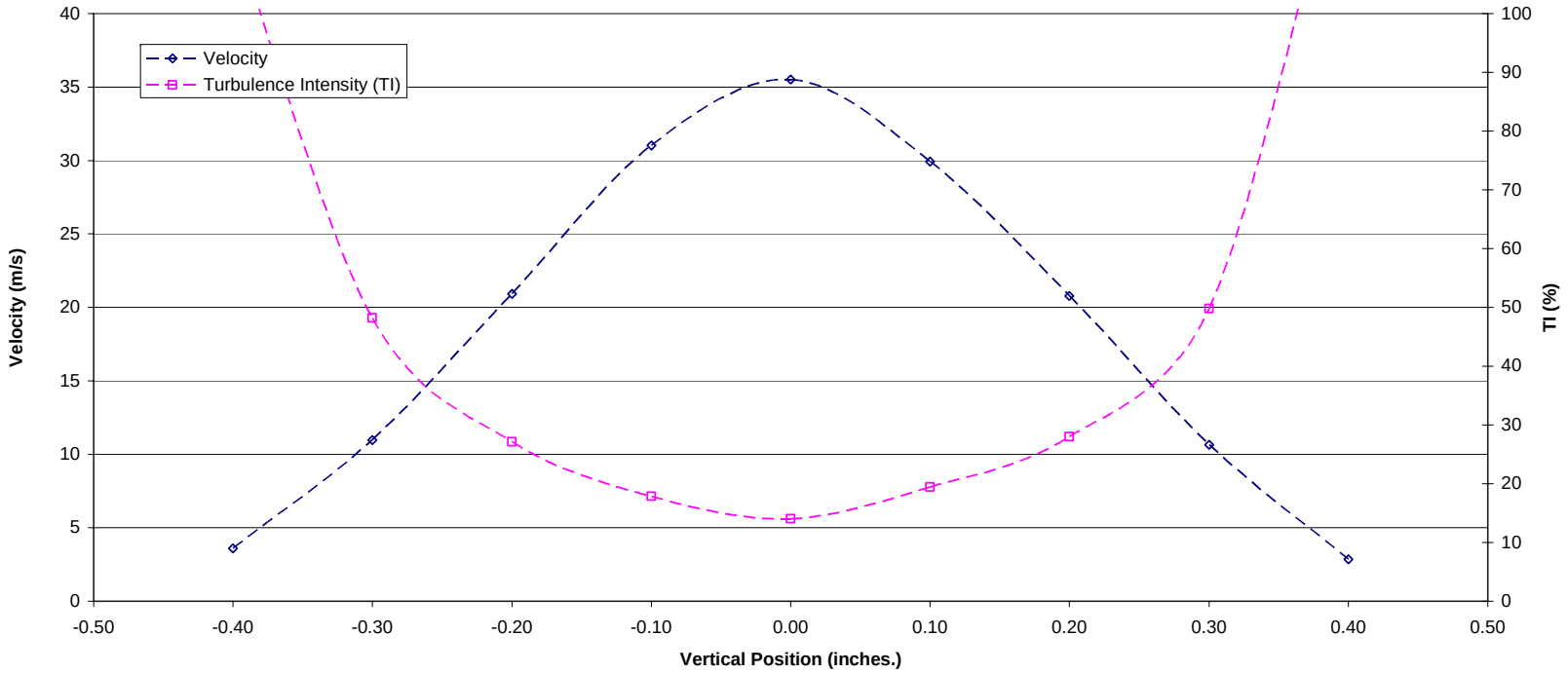

Figure B-15
Velocity and Turbulence Intensity as a Function of Vertical Position at a Horizontal Position of 2.2 Inches
(30 Degree Die – 2 psig Back Pressure)

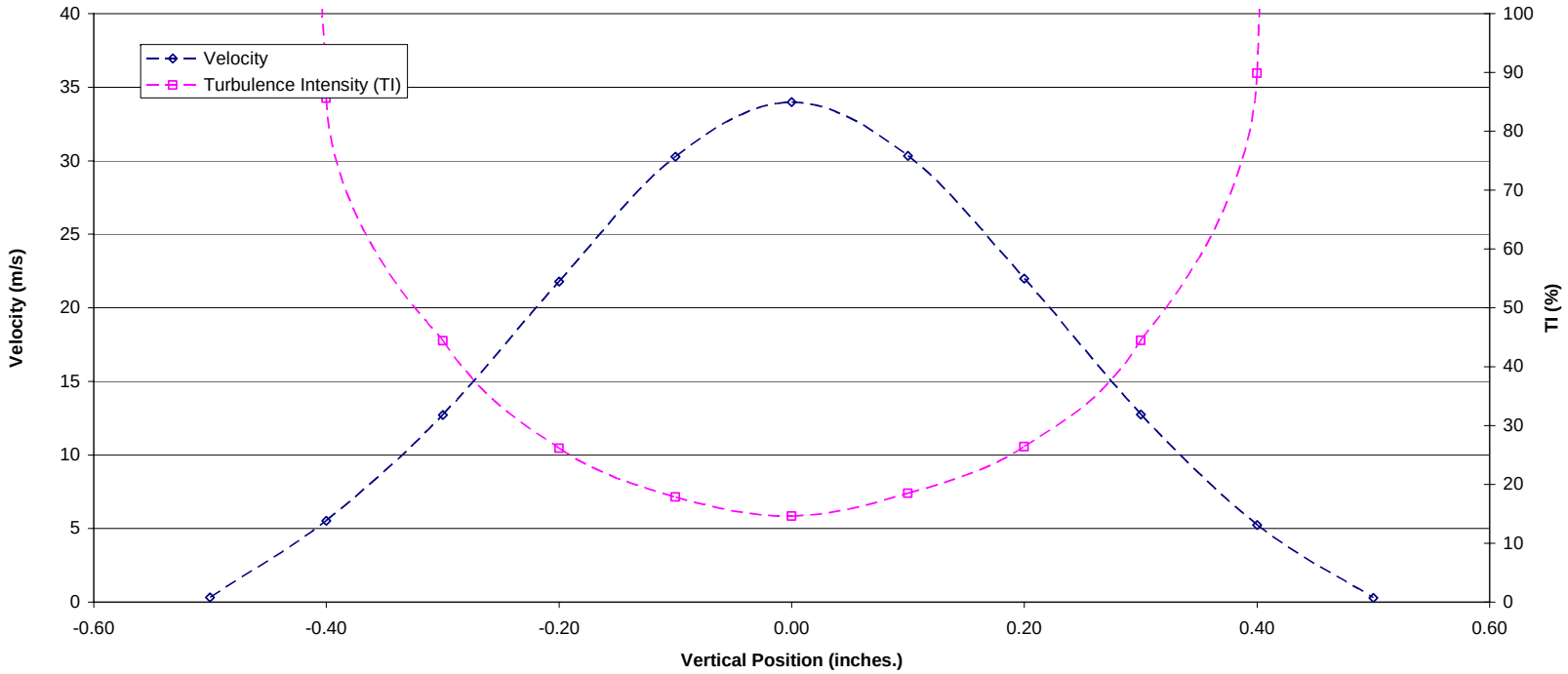

Figure B-16
Velocity and Turbulence Intensity as a Function of Vertical Position at a Horizontal Position of 2.4 Inches
(30 Degree Die – 2 psig Back Pressure)

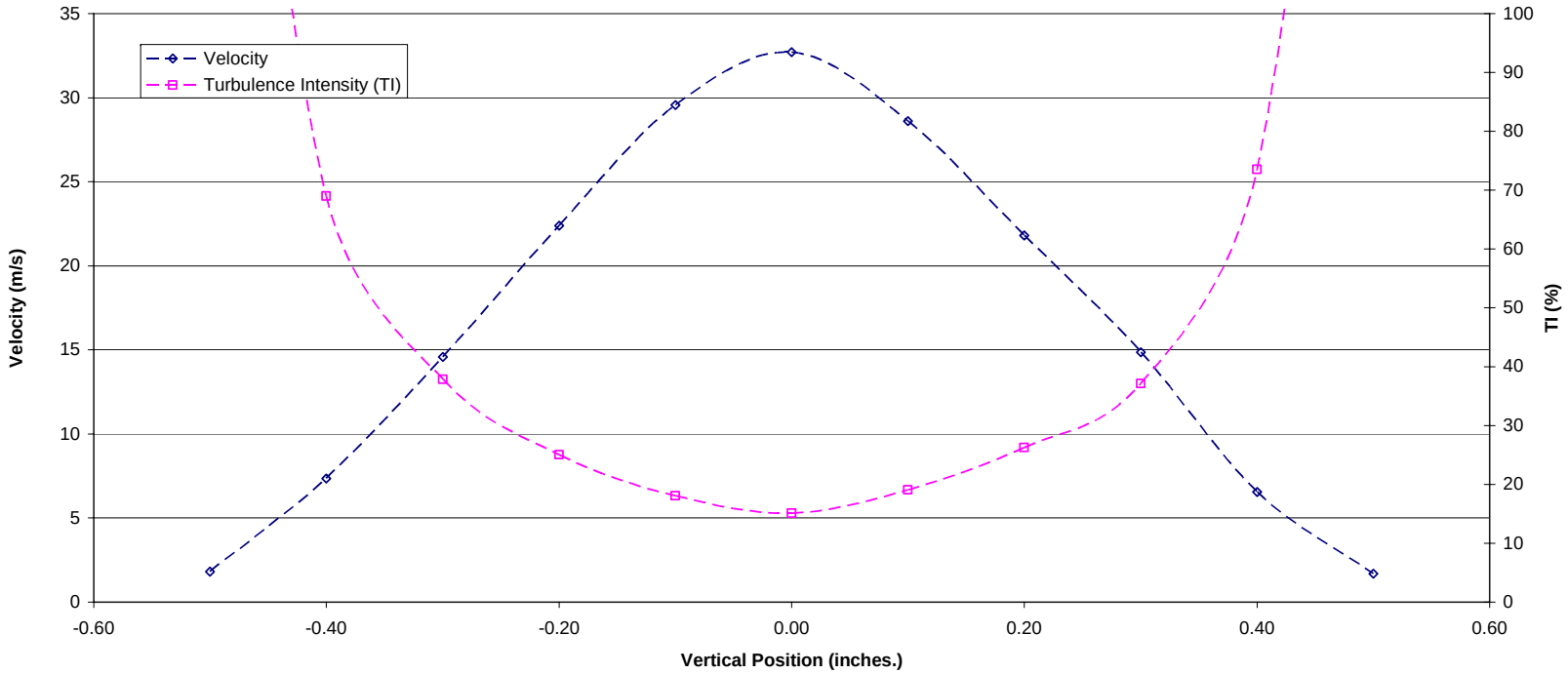

Figure B-17
Velocity and Turbulence Intensity as a Function of Vertical Position at a Horizontal Position of 2.6 Inches
(30 Degree Die – 2 psig Back Pressure)

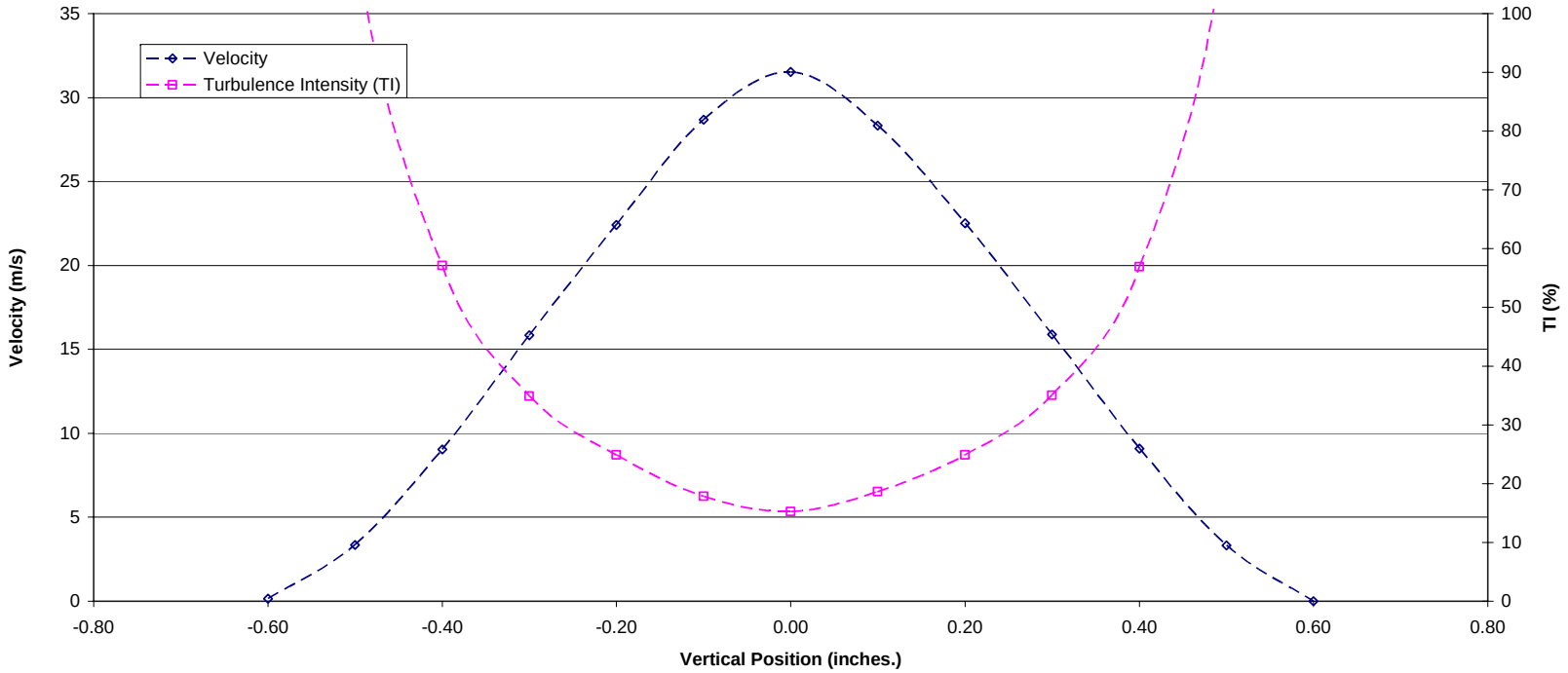

Figure B-18
Velocity and Turbulence Intensity as a Function of Vertical Position at a Horizontal Position of 2.8 Inches
(30 Degree Die – 2 psig Back Pressure)

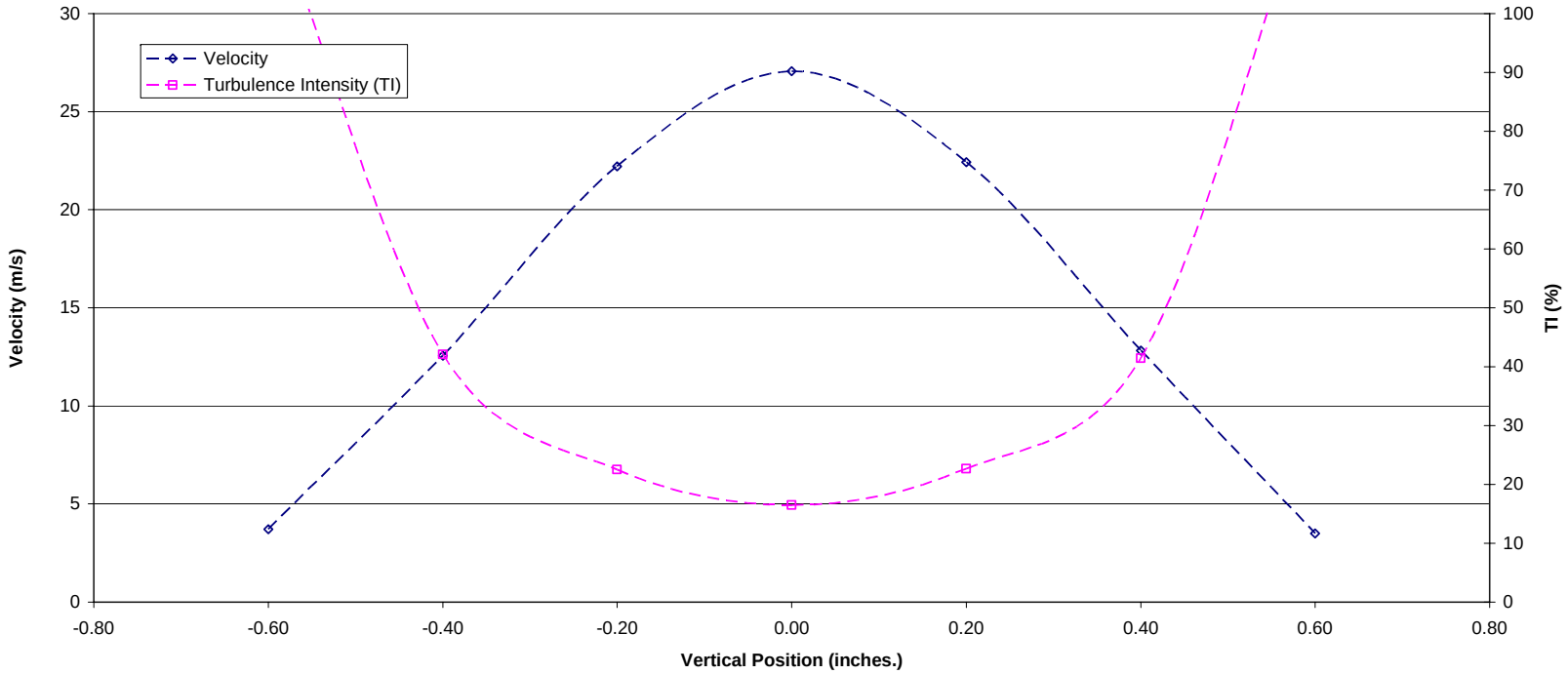

Figure B-19
Velocity and Turbulence Intensity as a Function of Vertical Position at a Horizontal Position of 3.5 Inches
(30 Degree Die – 2 psig Back Pressure)

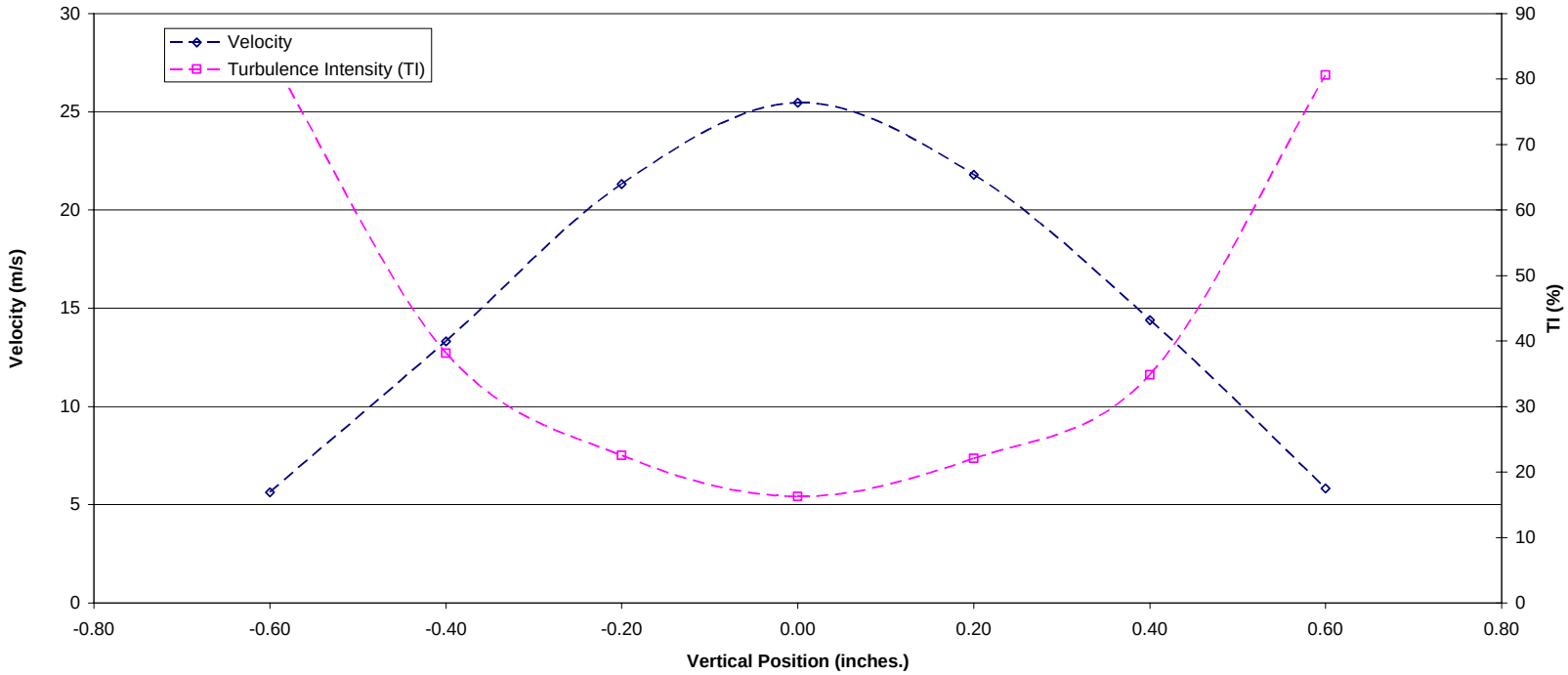

Figure B-20
Velocity and Turbulence Intensity as a Function of Vertical Position at a Horizontal Position of 4.0 Inches
(30 Degree Die – 2 psig Back Pressure)

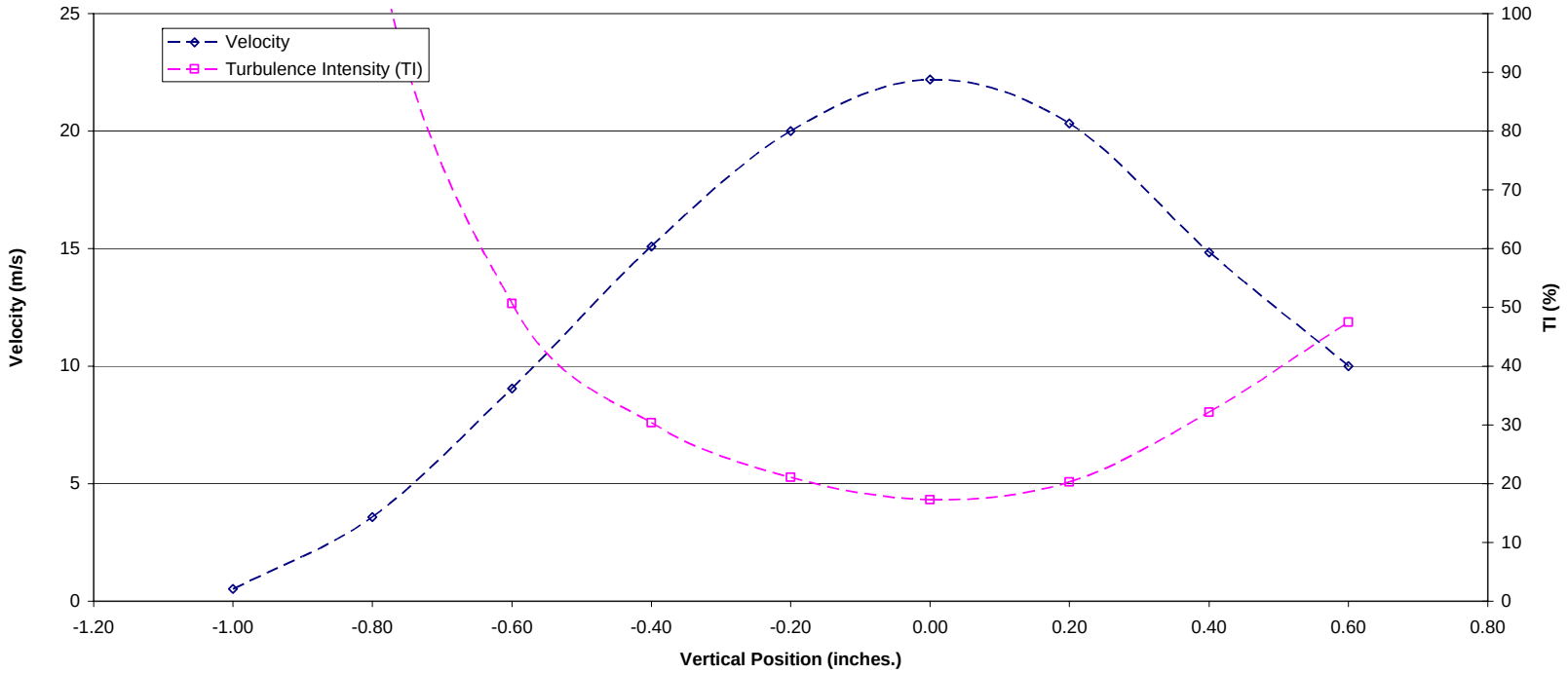

Figure B-21
Velocity and Turbulence Intensity as a Function of Vertical Position at a Horizontal Position of 5.0 Inches
(30 Degree Die – 2 psig Back Pressure)

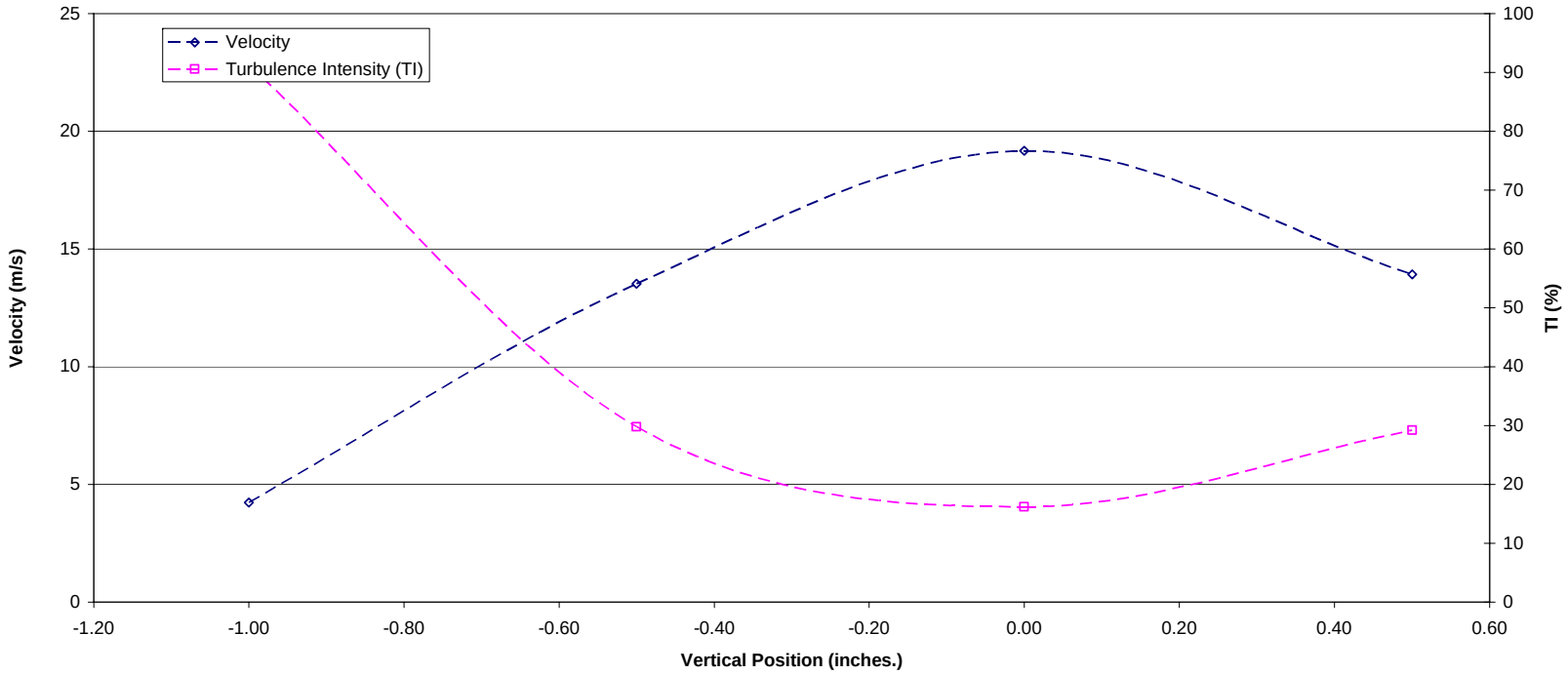

Figure B-22
Velocity and Turbulence Intensity as a Function of Vertical Position at a Horizontal Position of 7.0 Inches
(30 Degree Die – 2 psig Back Pressure)

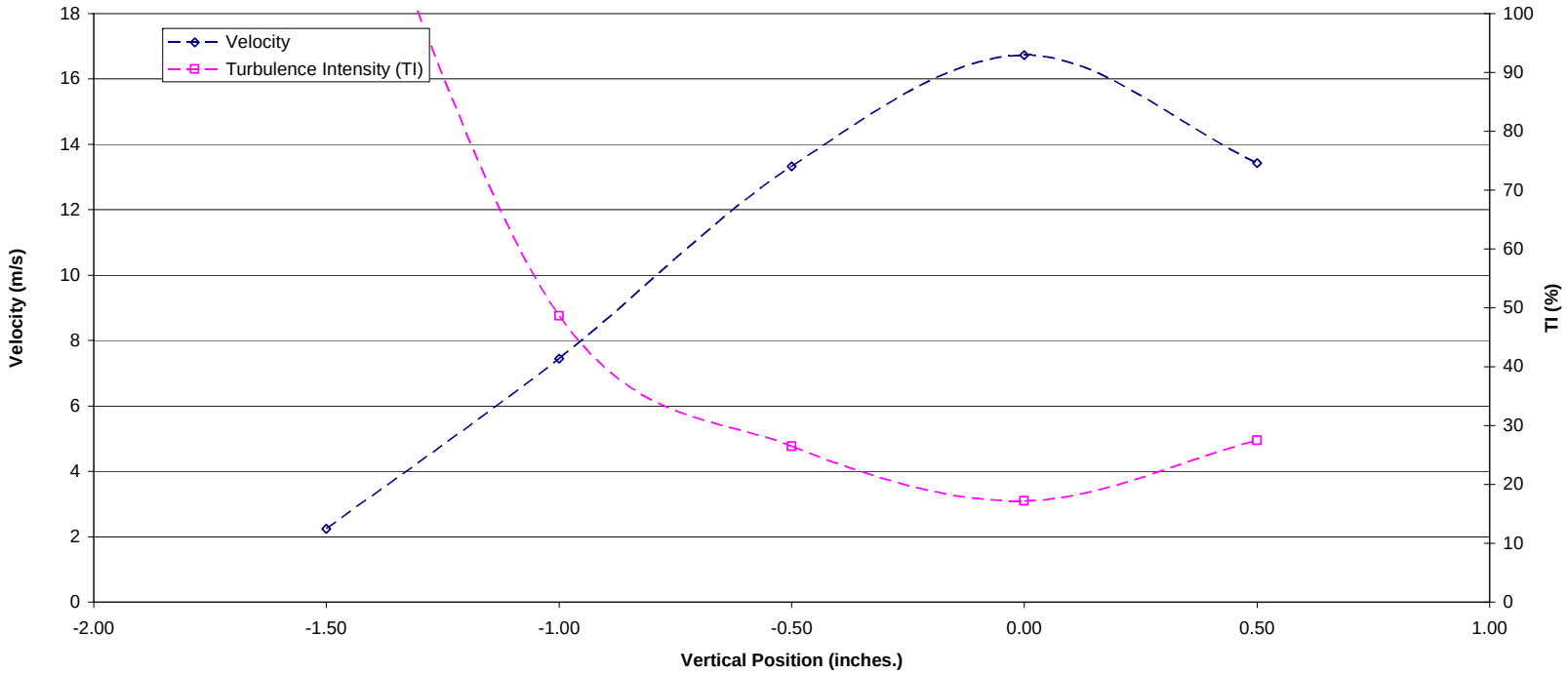

Figure B-23
Velocity and Turbulence Intensity as a Function of Vertical Position at a Horizontal Position of 9.0 Inches
(30 Degree Die – 2 psig Back Pressure)

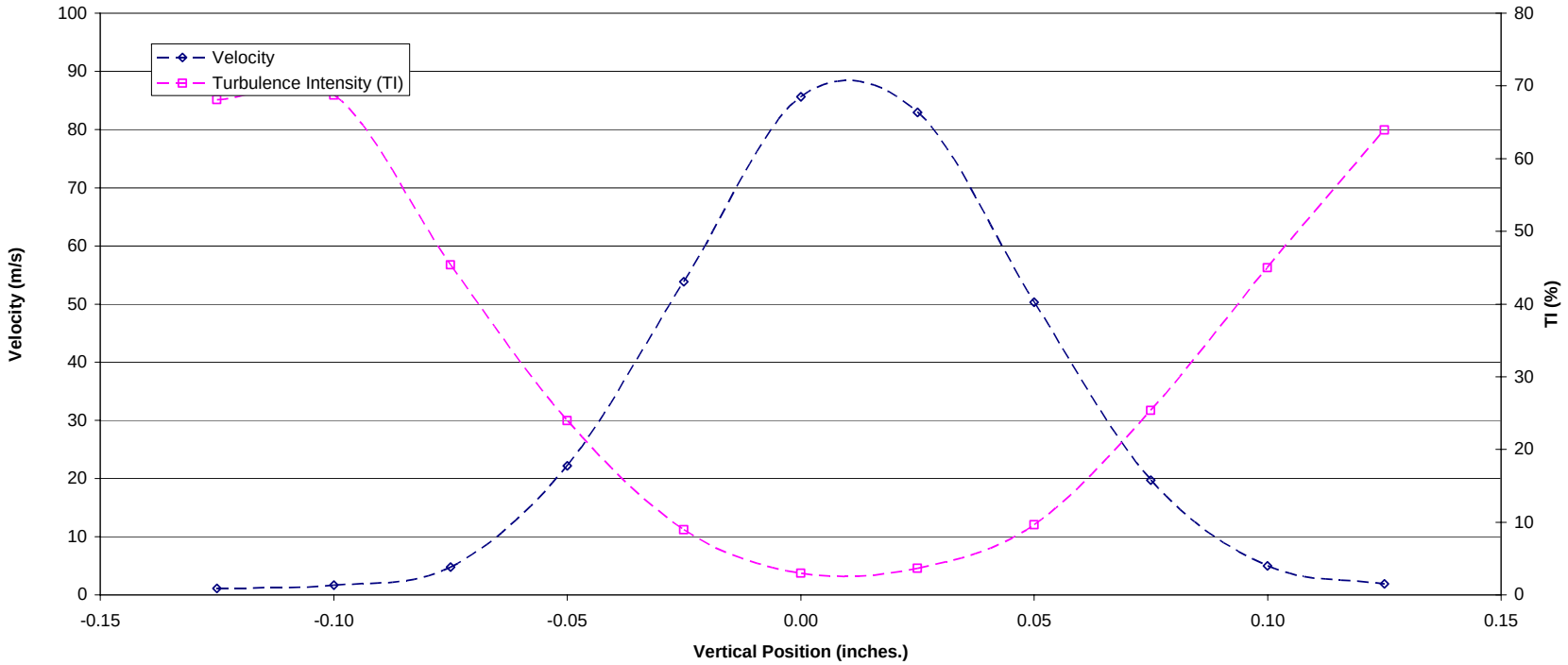

Figure B-24
Velocity and Turbulence Intensity as a Function of Vertical Position at a Horizontal Position of .2 Inches
(60 Degree Die – 2 psig Back Pressure)

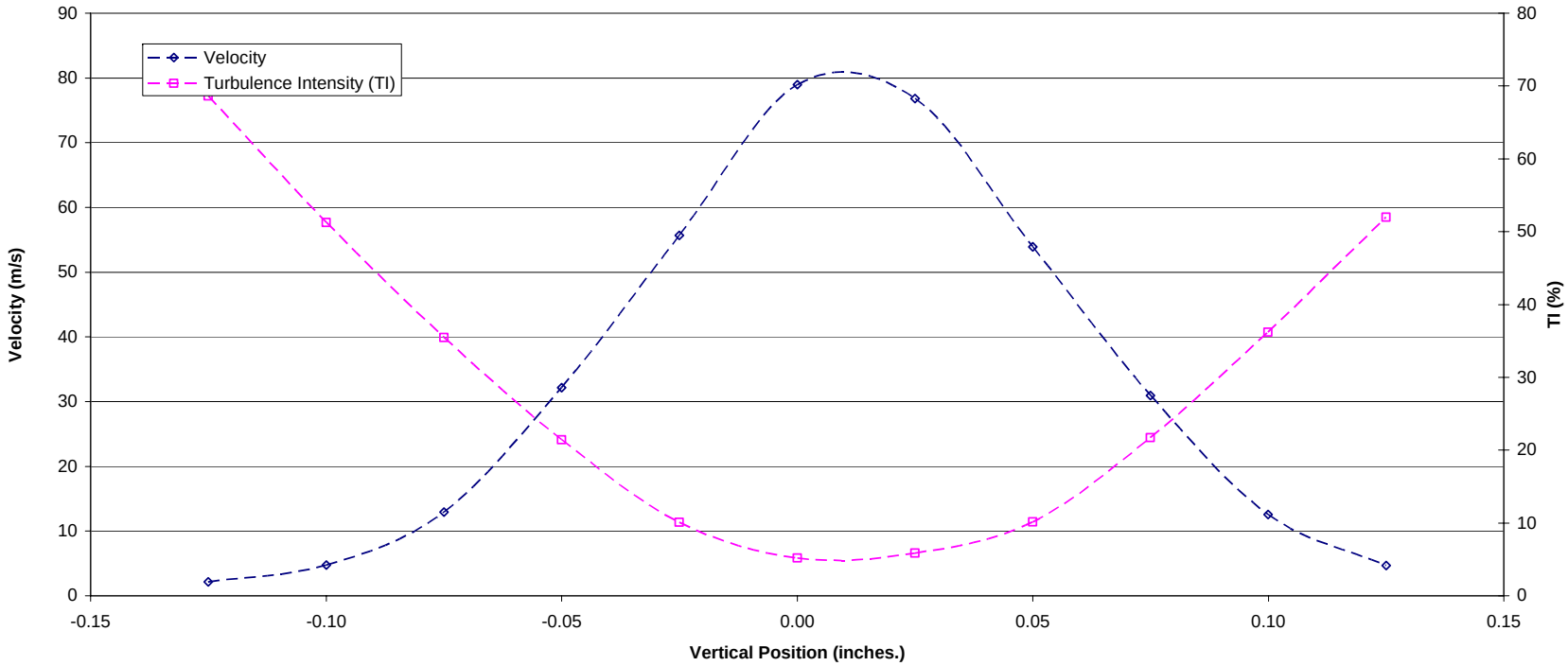

Figure B-25
Velocity and Turbulence Intensity as a Function of Vertical Position at a Horizontal Position of .3 Inches
(60 Degree Die – 2 psig Back Pressure)

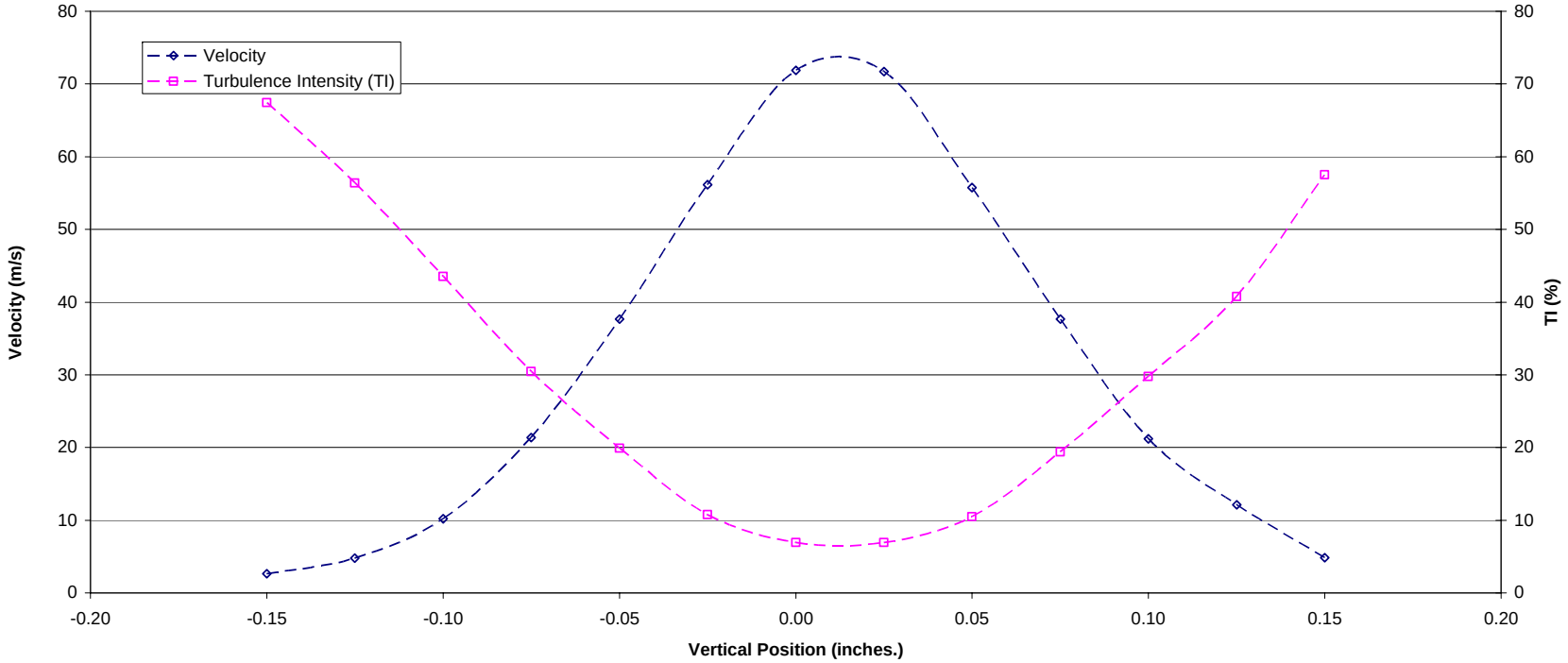

Figure B-26
Velocity and Turbulence Intensity as a Function of Vertical Position at a Horizontal Position of .4 Inches
(60 Degree Die – 2 psig Back Pressure)

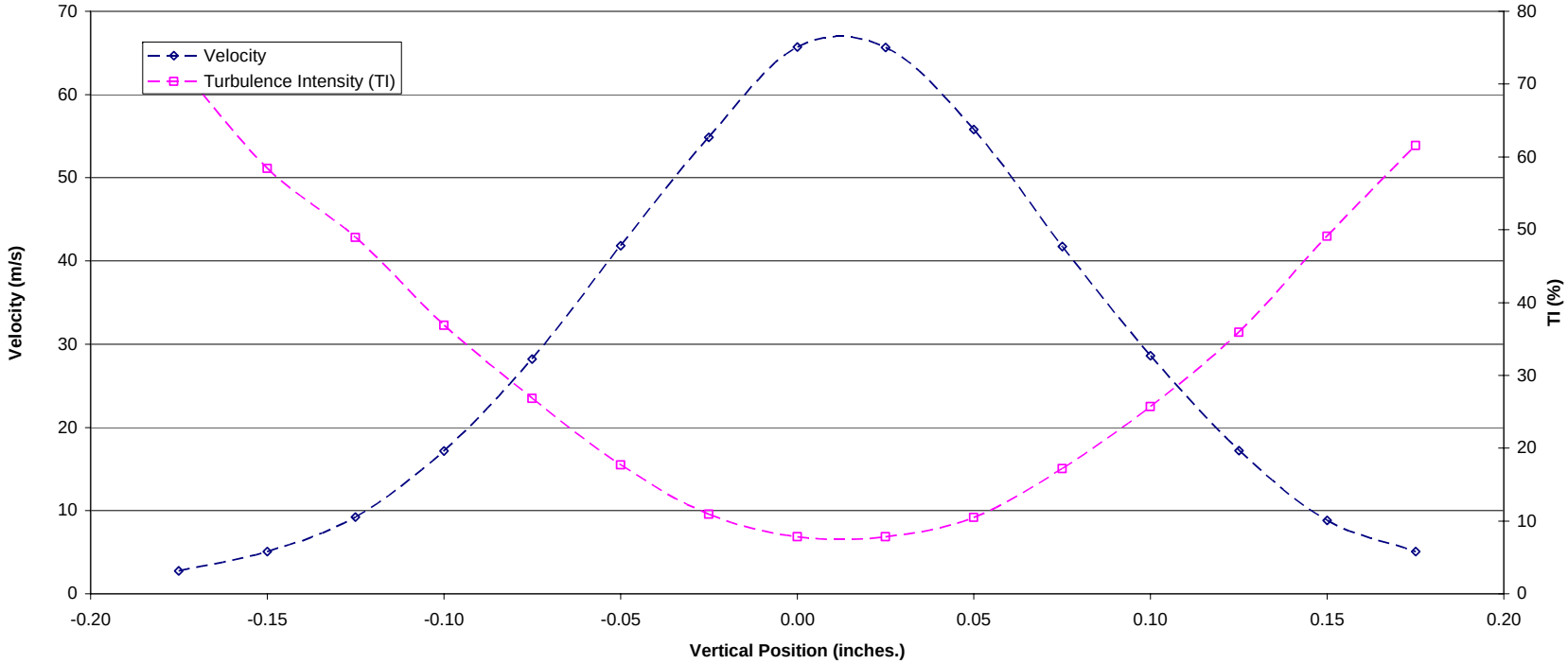

Figure B-27
Velocity and Turbulence Intensity as a Function of Vertical Position at a Horizontal Position of .5 Inches
(60 Degree Die – 2 psig Back Pressure)

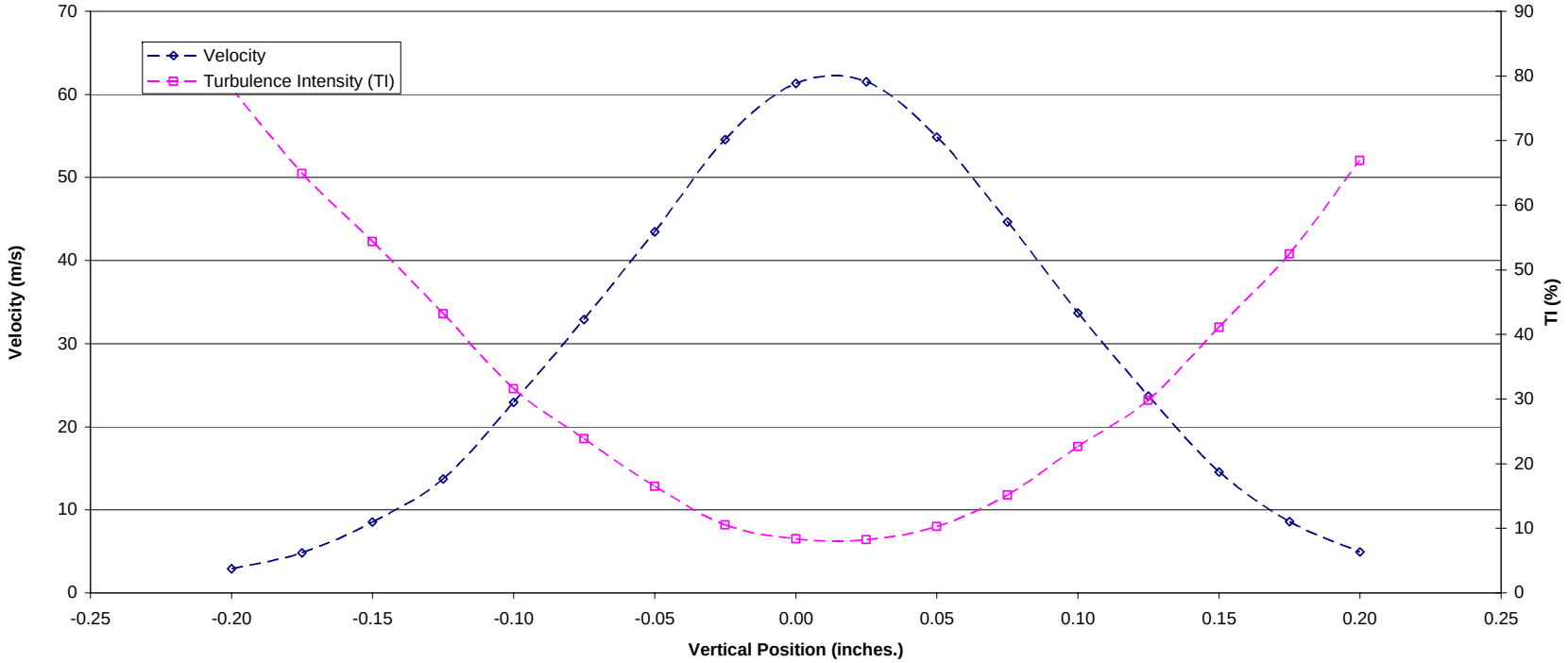

Figure B-28
Velocity and Turbulence Intensity as a Function of Vertical Position at a Horizontal Position of .6 Inches
(60 Degree Die – 2 psig Back Pressure)

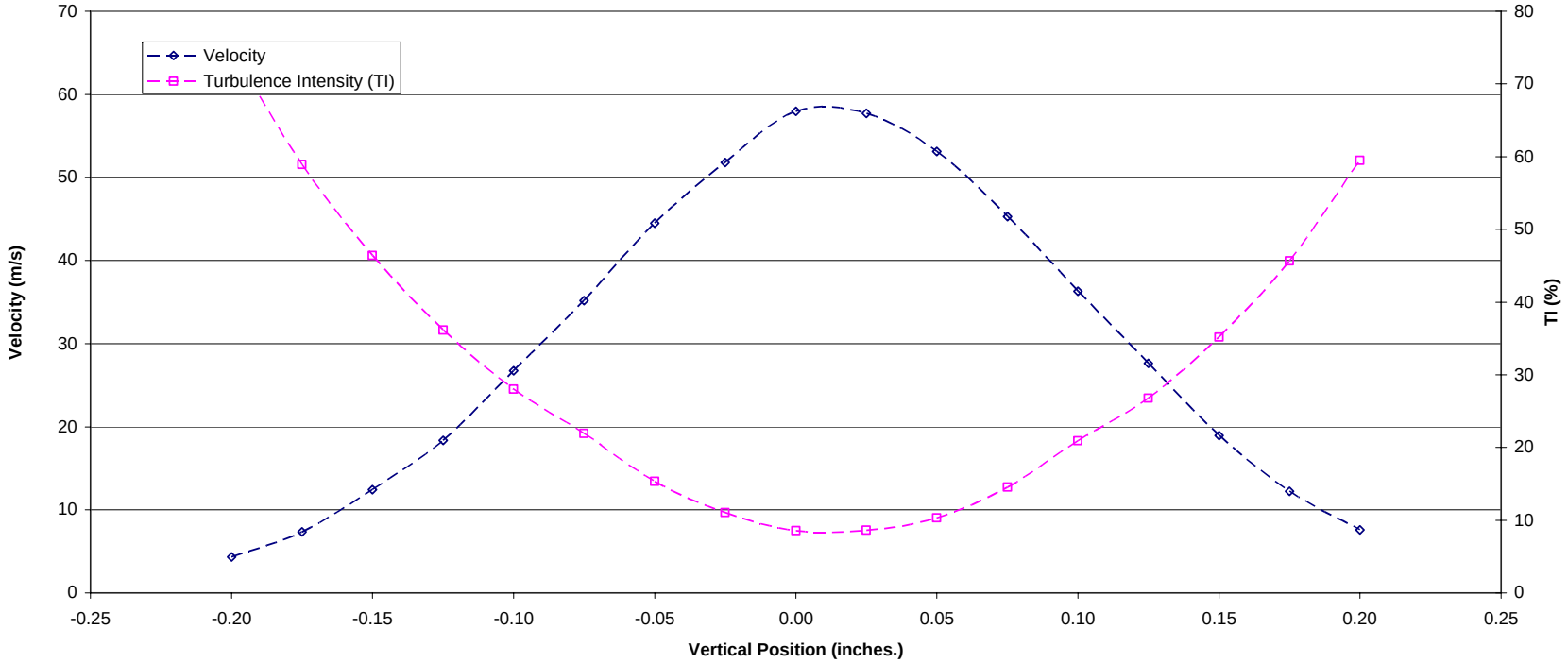

Figure B-29
Velocity and Turbulence Intensity as a Function of Vertical Position at a Horizontal Position of .7 Inches
(60 Degree Die – 2 psig Back Pressure)

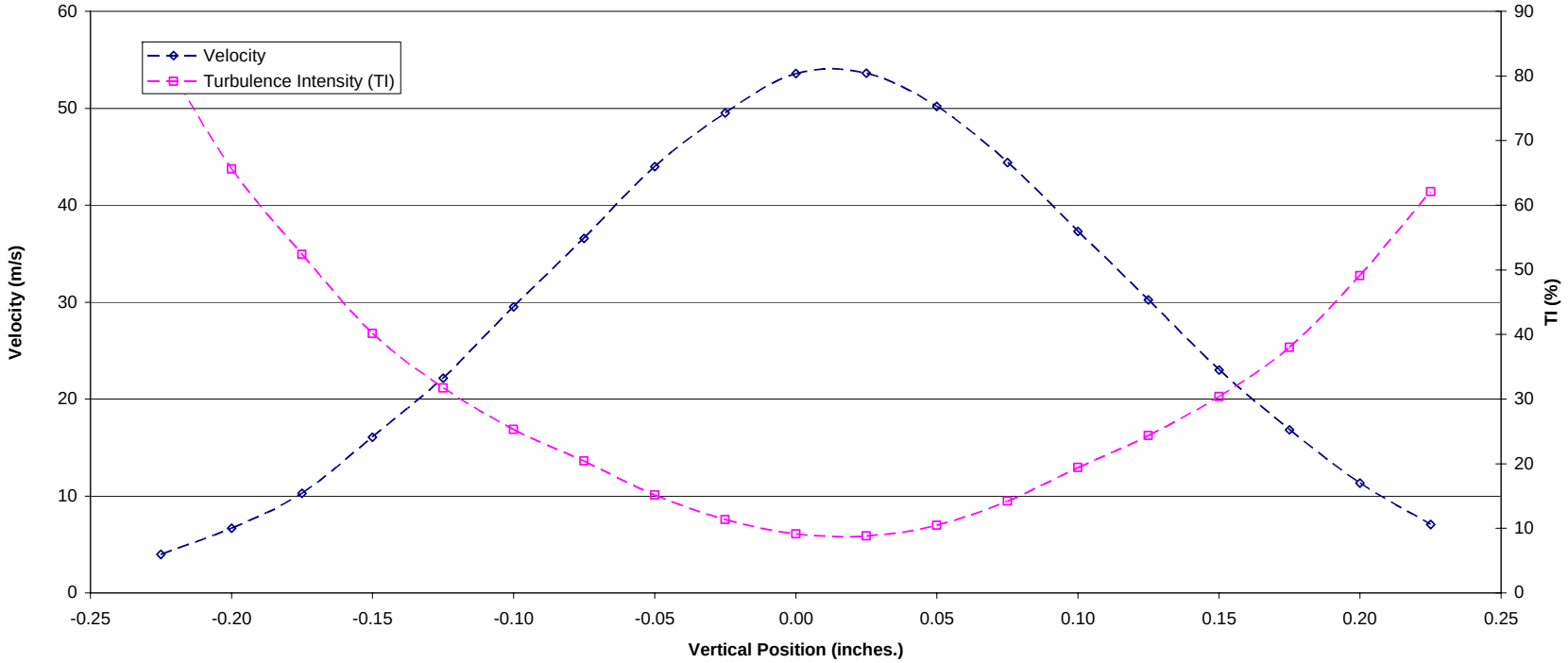

Figure B-30
Velocity and Turbulence Intensity as a Function of Vertical Position at a Horizontal Position of .8 Inches
(60 Degree Die – 2 psig Back Pressure)

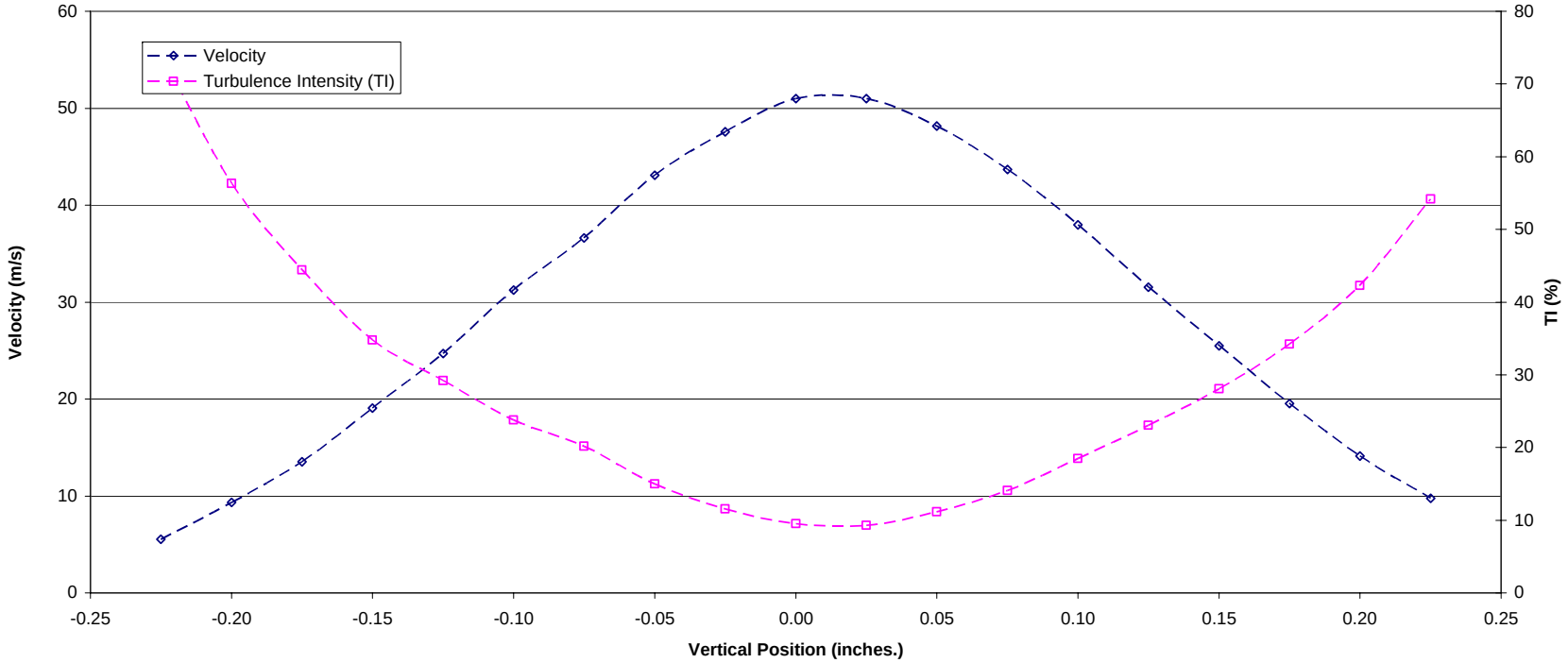

Figure B-31
Velocity and Turbulence Intensity as a Function of Vertical Position at a Horizontal Position of .9 Inches
(60 Degree Die – 2 psig Back Pressure)

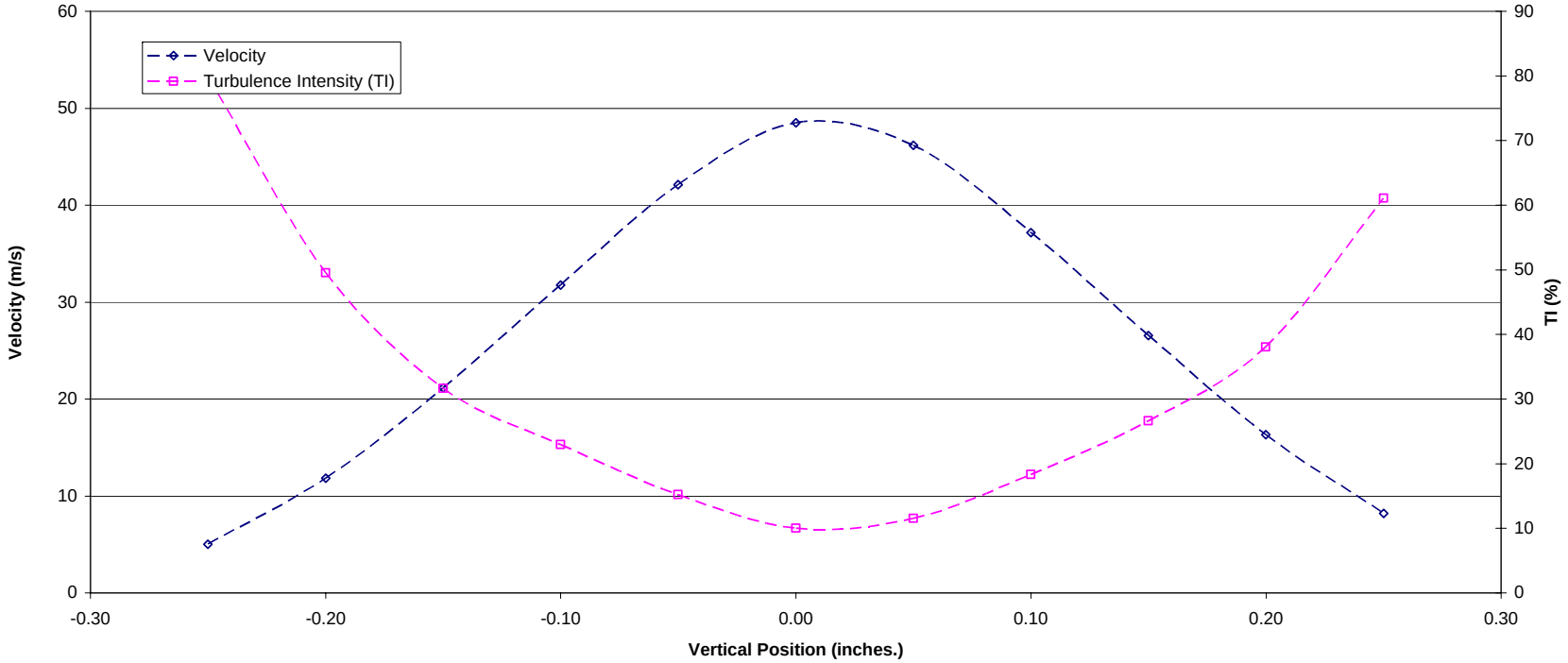

Figure B-32
Velocity and Turbulence Intensity as a Function of Vertical Position at a Horizontal Position of 1.0 Inches
(60 Degree Die – 2 psig Back Pressure)

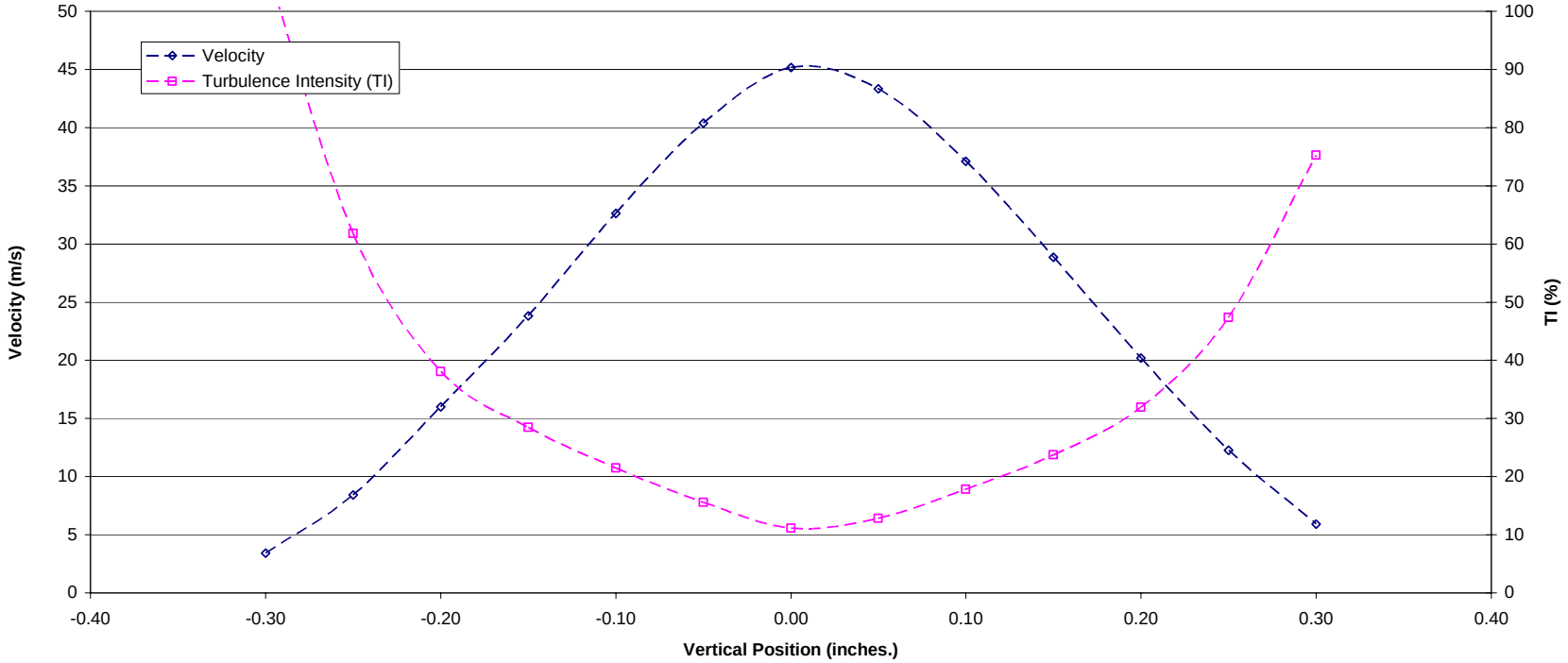

Figure B-33
Velocity and Turbulence Intensity as a Function of Vertical Position at a Horizontal Position of 1.2 Inches
(60 Degree Die – 2 psig Back Pressure)

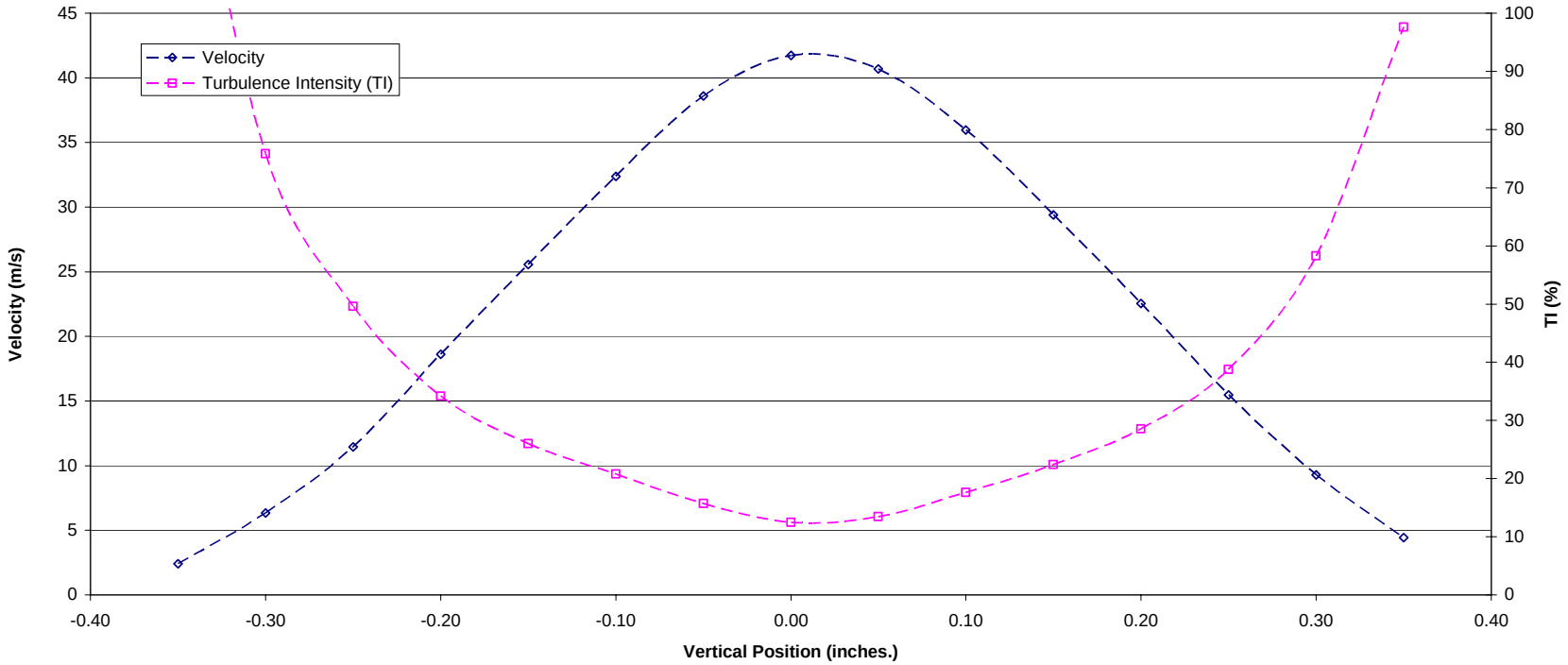

Figure B-34
Velocity and Turbulence Intensity as a Function of Vertical Position at a Horizontal Position of 1.4 Inches
(60 Degree Die – 2 psig Back Pressure)

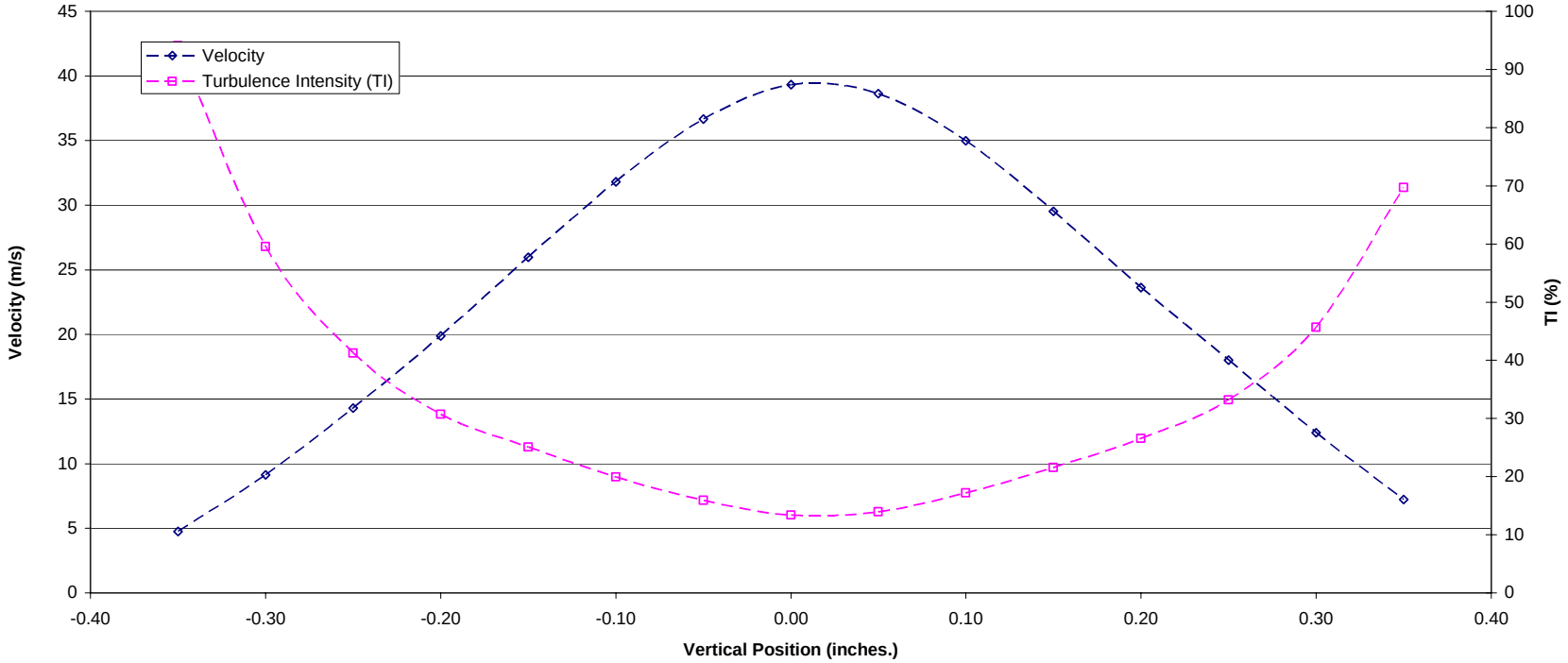

Figure B-35
Velocity and Turbulence Intensity as a Function of Vertical Position at a Horizontal Position of 1.6 Inches
(60 Degree Die – 2 psig Back Pressure)

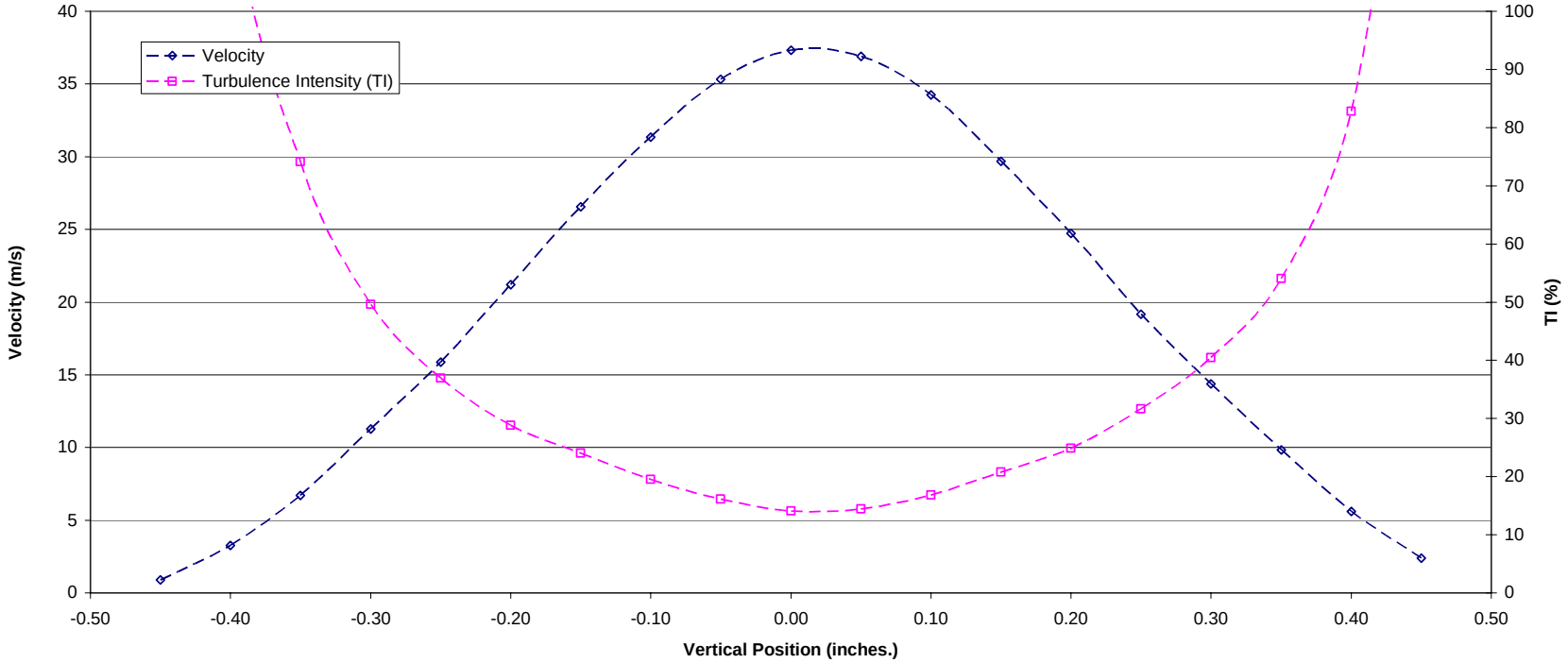

Figure B-36
Velocity and Turbulence Intensity as a Function of Vertical Position at a Horizontal Position of 1.8 Inches
(60 Degree Die – 2 psig Back Pressure)

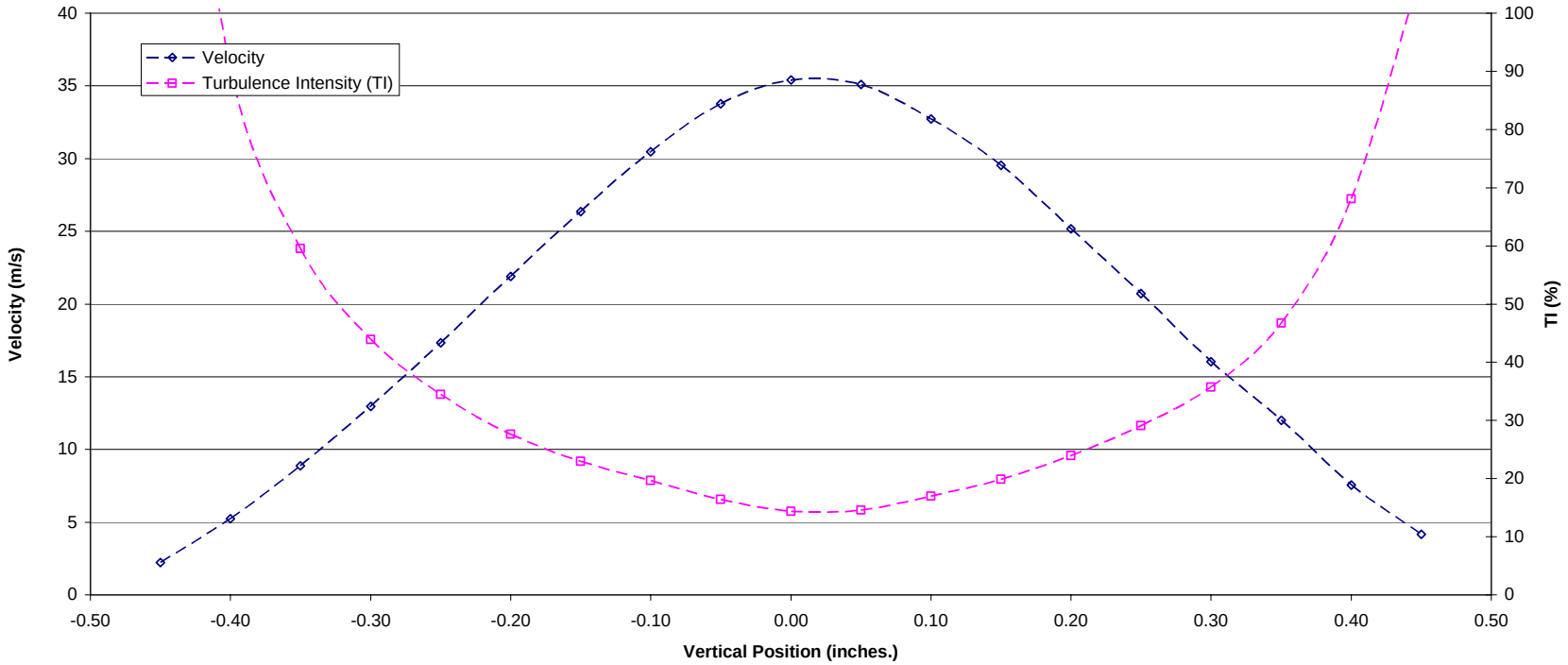

Figure B-37
Velocity and Turbulence Intensity as a Function of Vertical Position at a Horizontal Position of 2.0 Inches
(60 Degree Die – 2 psig Back Pressure)

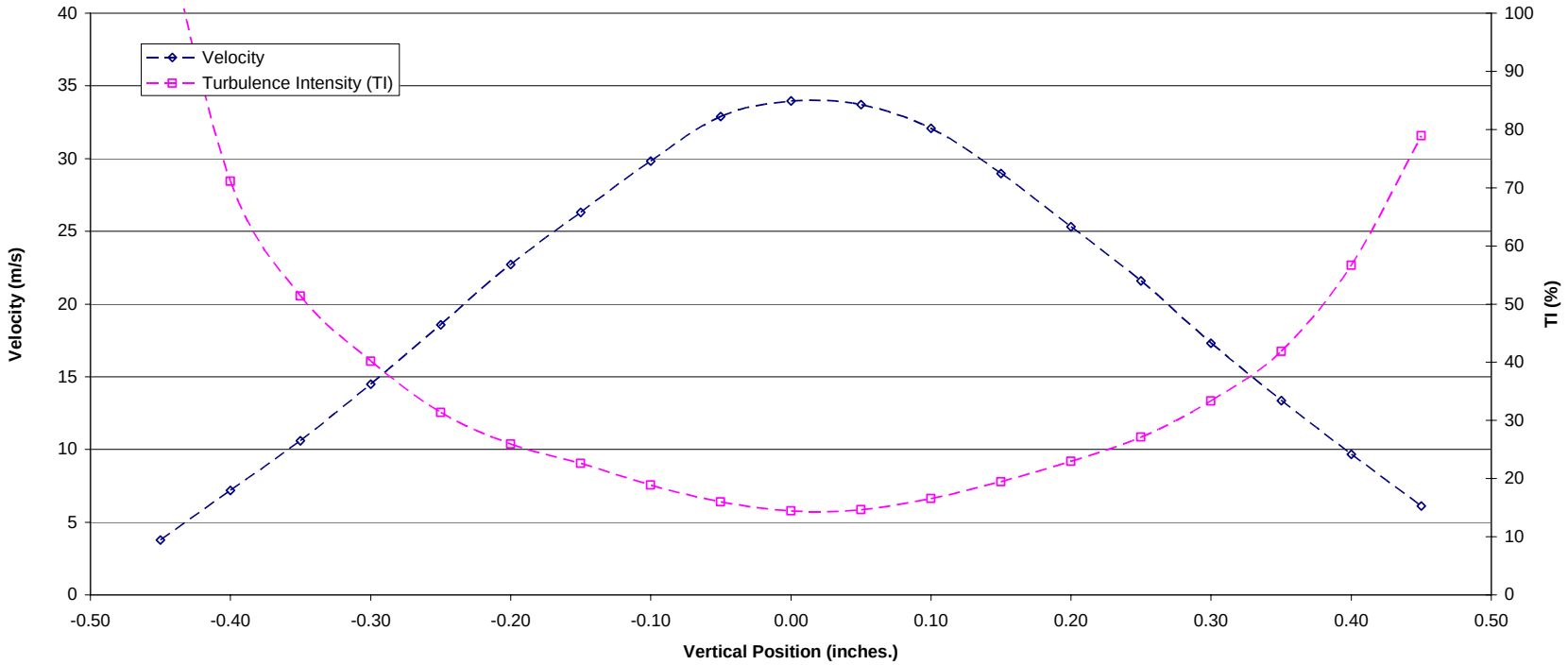

Figure B-38
Velocity and Turbulence Intensity as a Function of Vertical Position at a Horizontal Position of 2.2 Inches
(60 Degree Die – 2 psig Back Pressure)

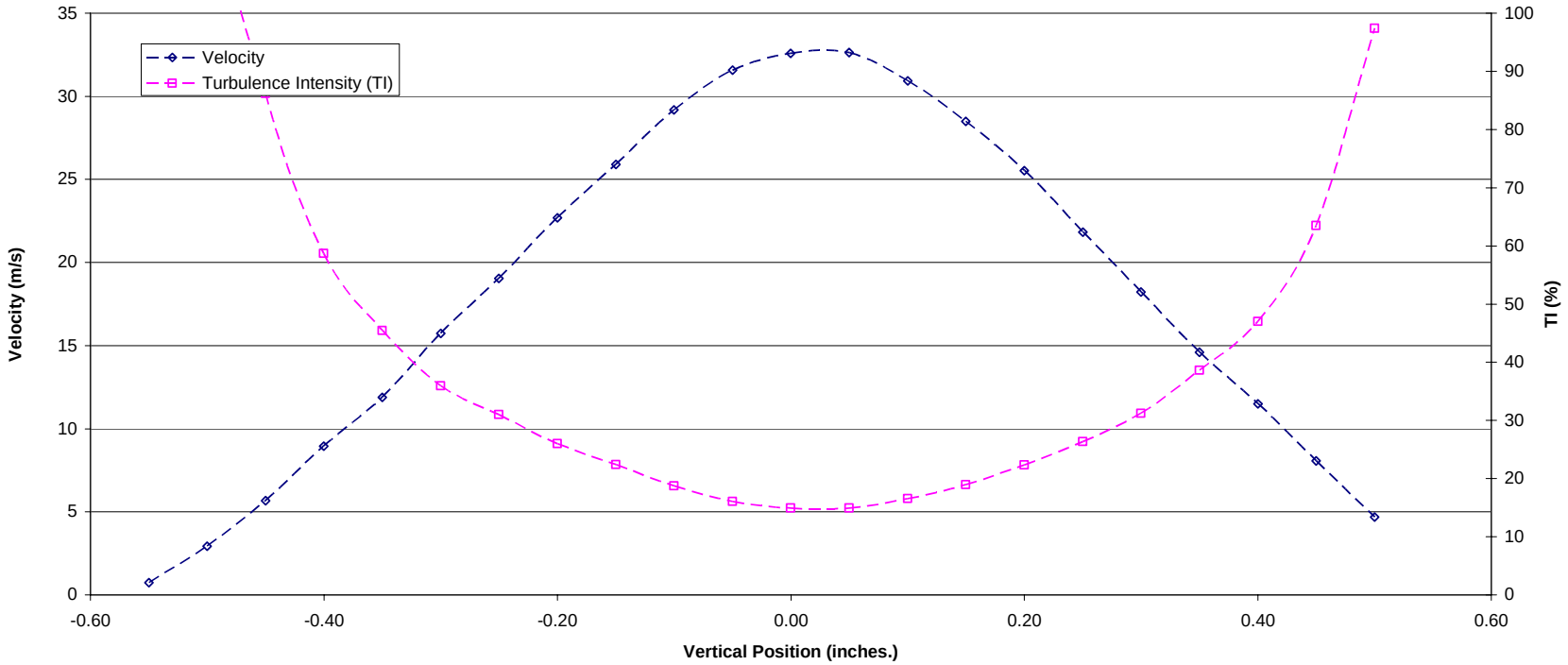

Figure B-39
Velocity and Turbulence Intensity as a Function of Vertical Position at a Horizontal Position of 2.4 Inches
(60 Degree Die – 2 psig Back Pressure)

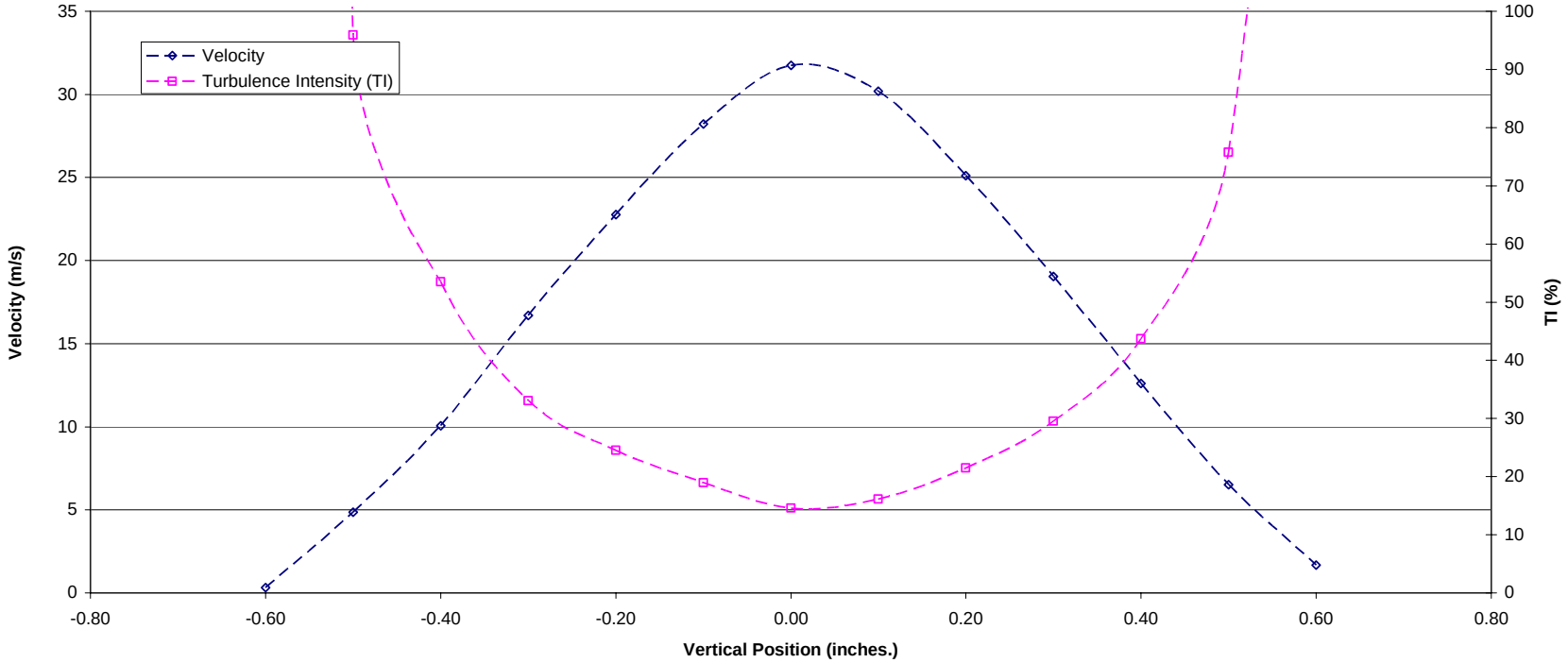

Figure B-40
Velocity and Turbulence Intensity as a Function of Vertical Position at a Horizontal Position of 2.6 Inches
(60 Degree Die – 2 psig Back Pressure)

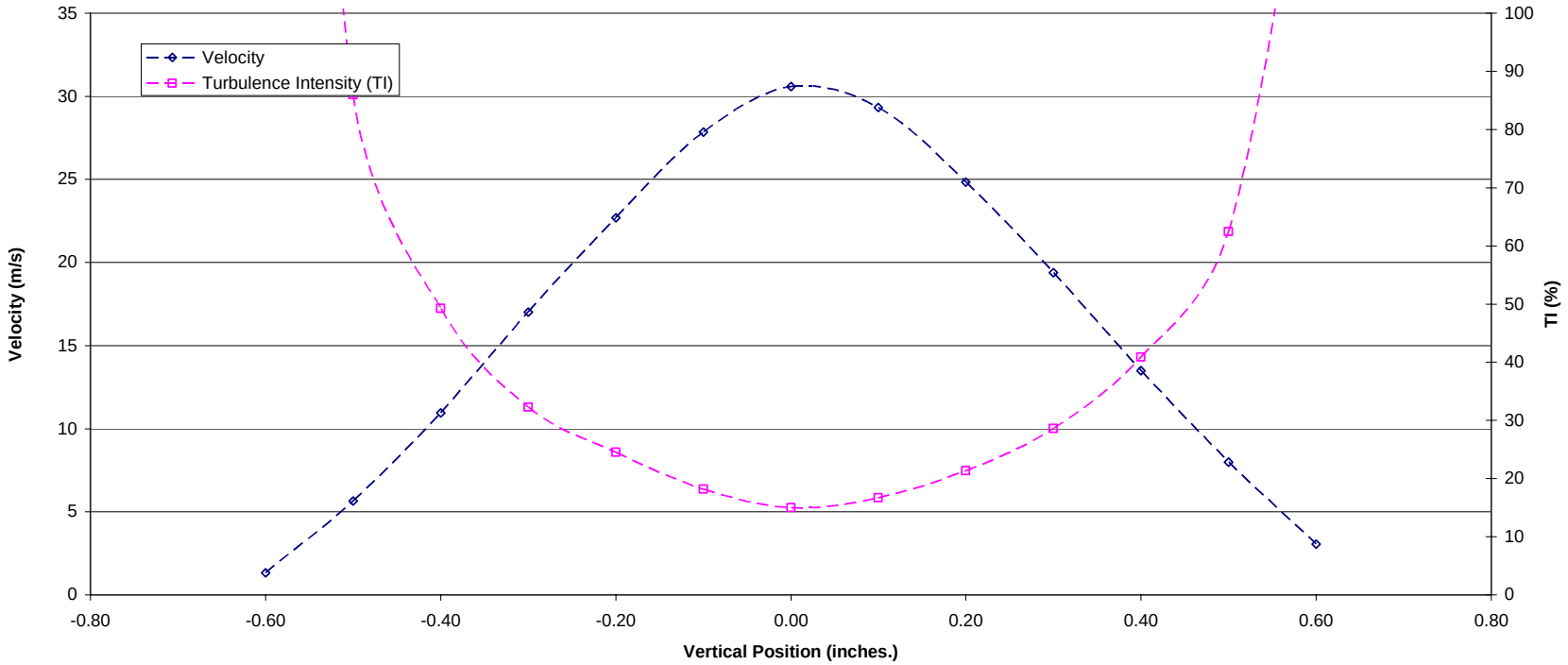

Figure B-41
Velocity and Turbulence Intensity as a Function of Vertical Position at a Horizontal Position of 2.8 Inches
(60 Degree Die – 2 psig Back Pressure)

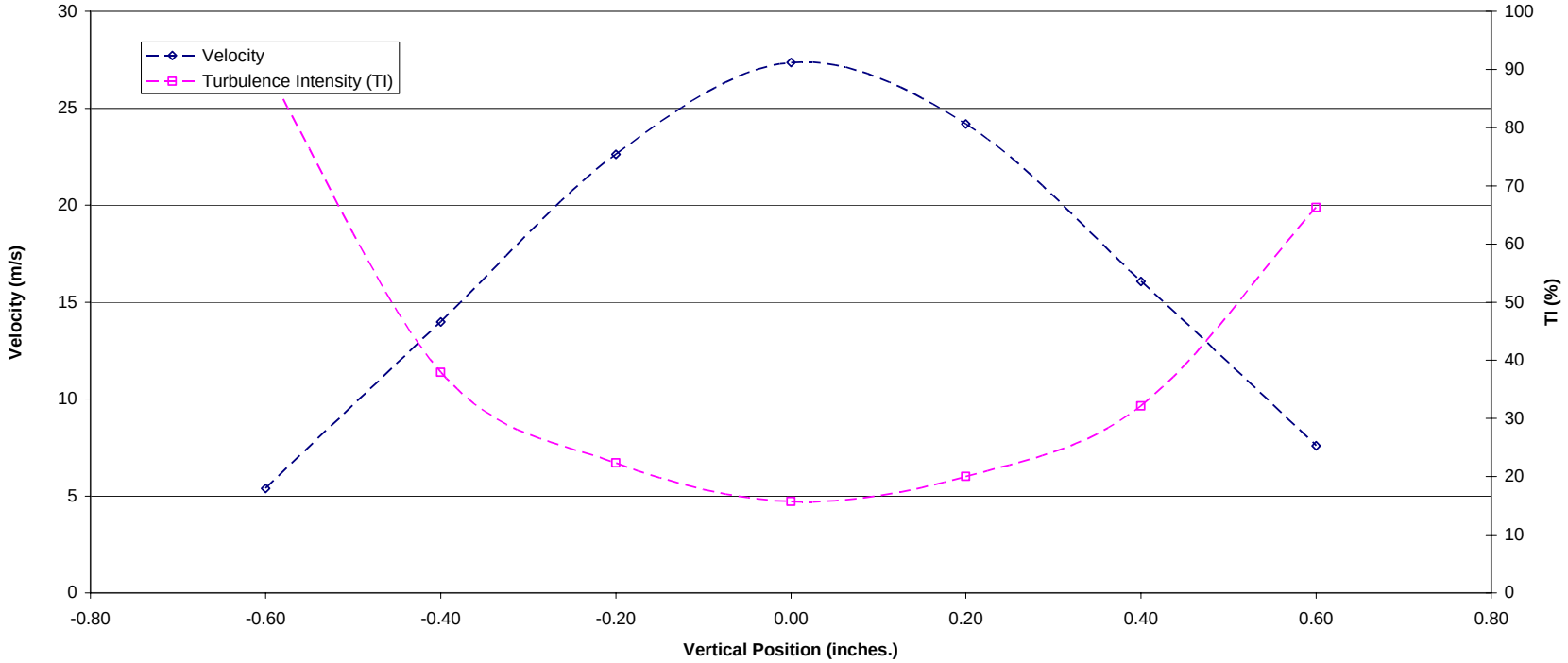

Figure B-42
Velocity and Turbulence Intensity as a Function of Vertical Position at a Horizontal Position of 3.5 Inches
(60 Degree Die – 2 psig Back Pressure)

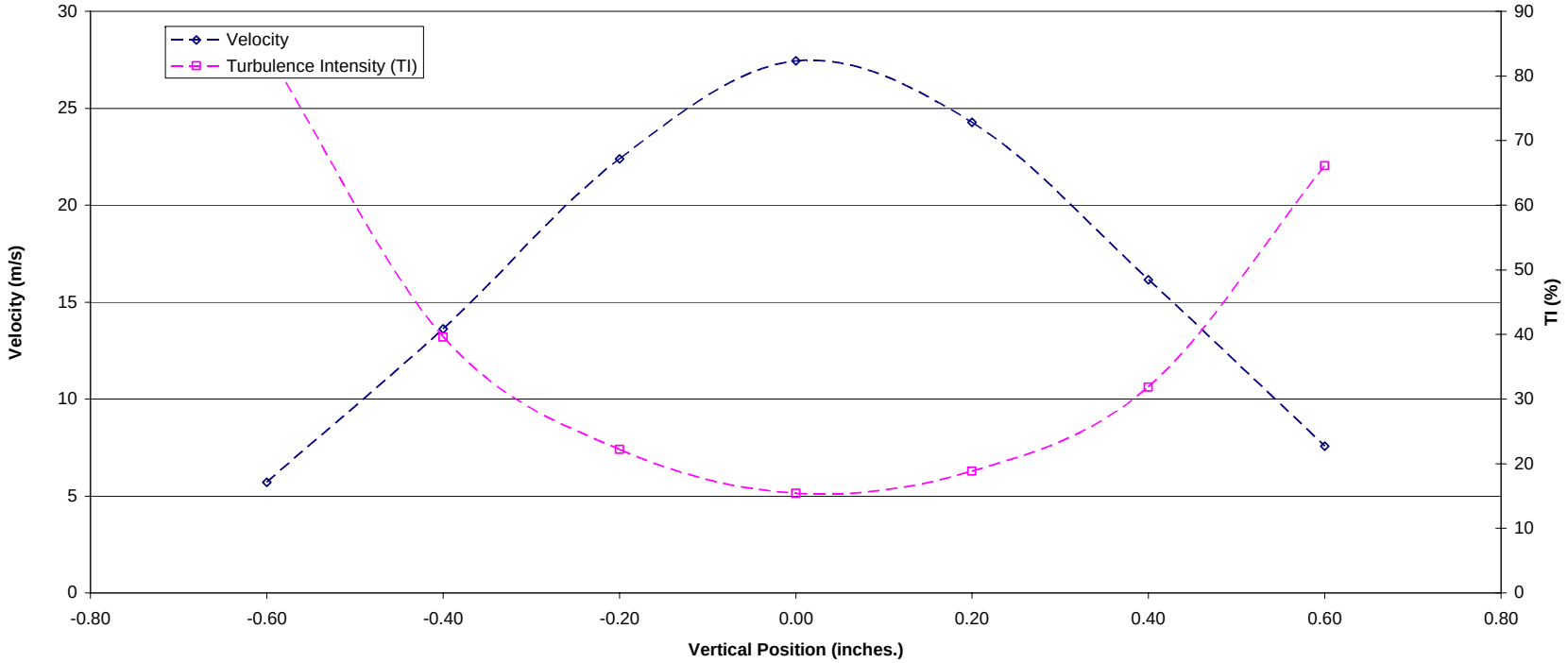

Figure B-43
Velocity and Turbulence Intensity as a Function of Vertical Position at a Horizontal Position of 4.0 Inches
(60 Degree Die – 2 psig Back Pressure)

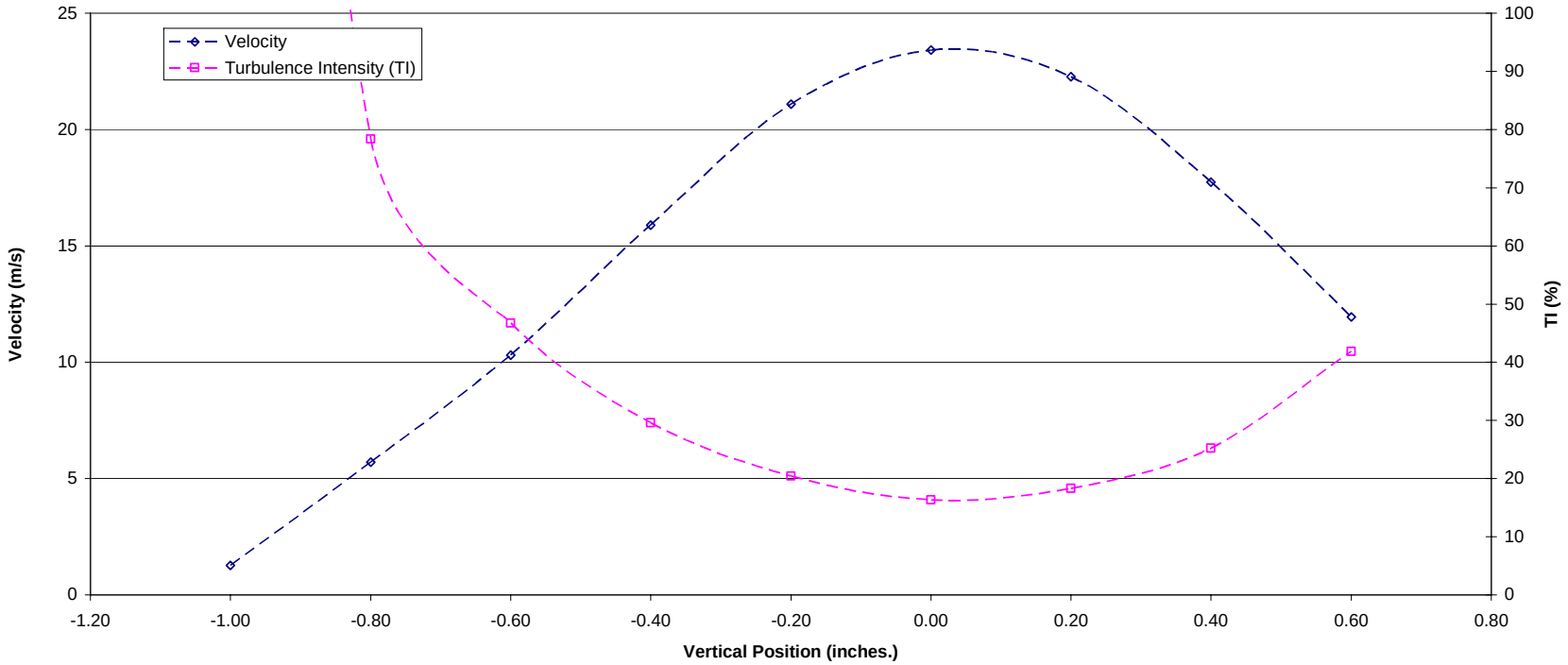

Figure B-44
Velocity and Turbulence Intensity as a Function of Vertical Position at a Horizontal Position of 5.0 Inches
(60 Degree Die – 2 psig Back Pressure)

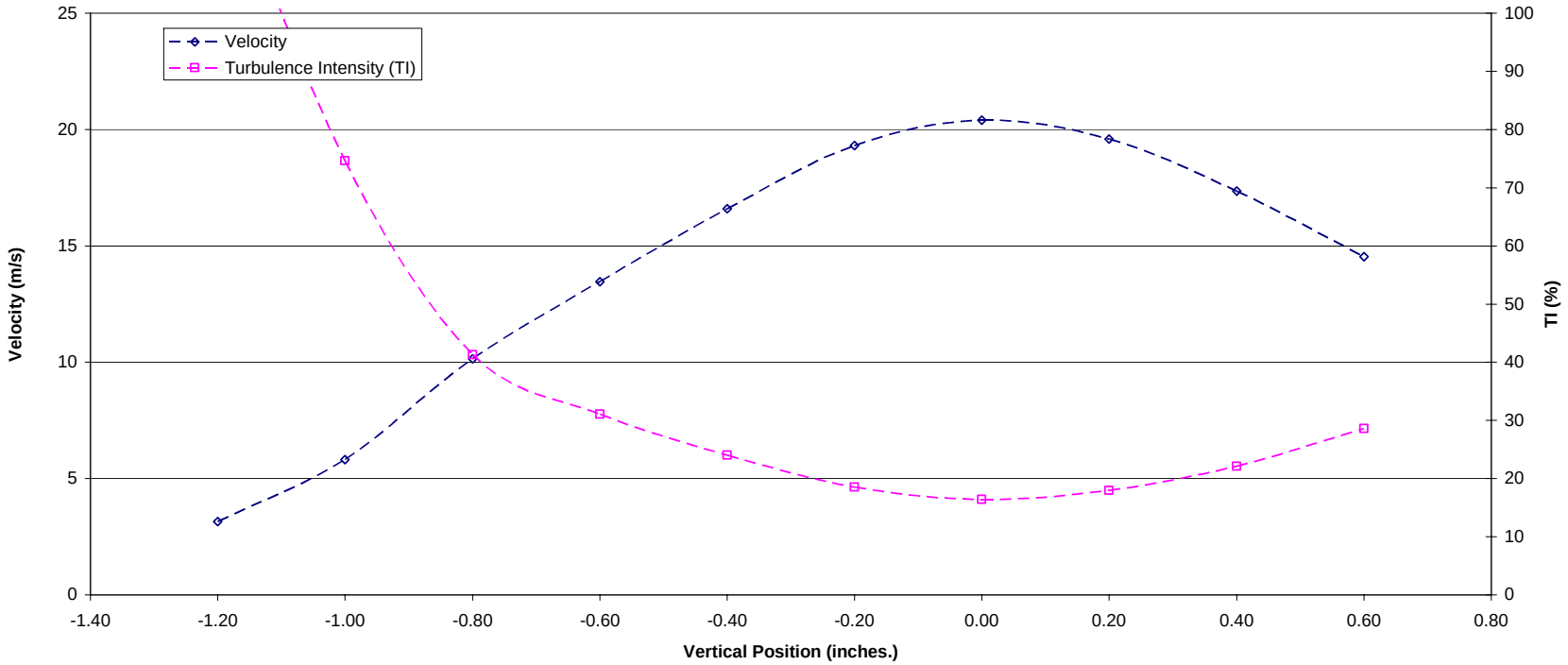

Figure B-45
Velocity and Turbulence Intensity as a Function of Vertical Position at a Horizontal Position of 7.0 Inches
(60 Degree Die – 2 psig Back Pressure)

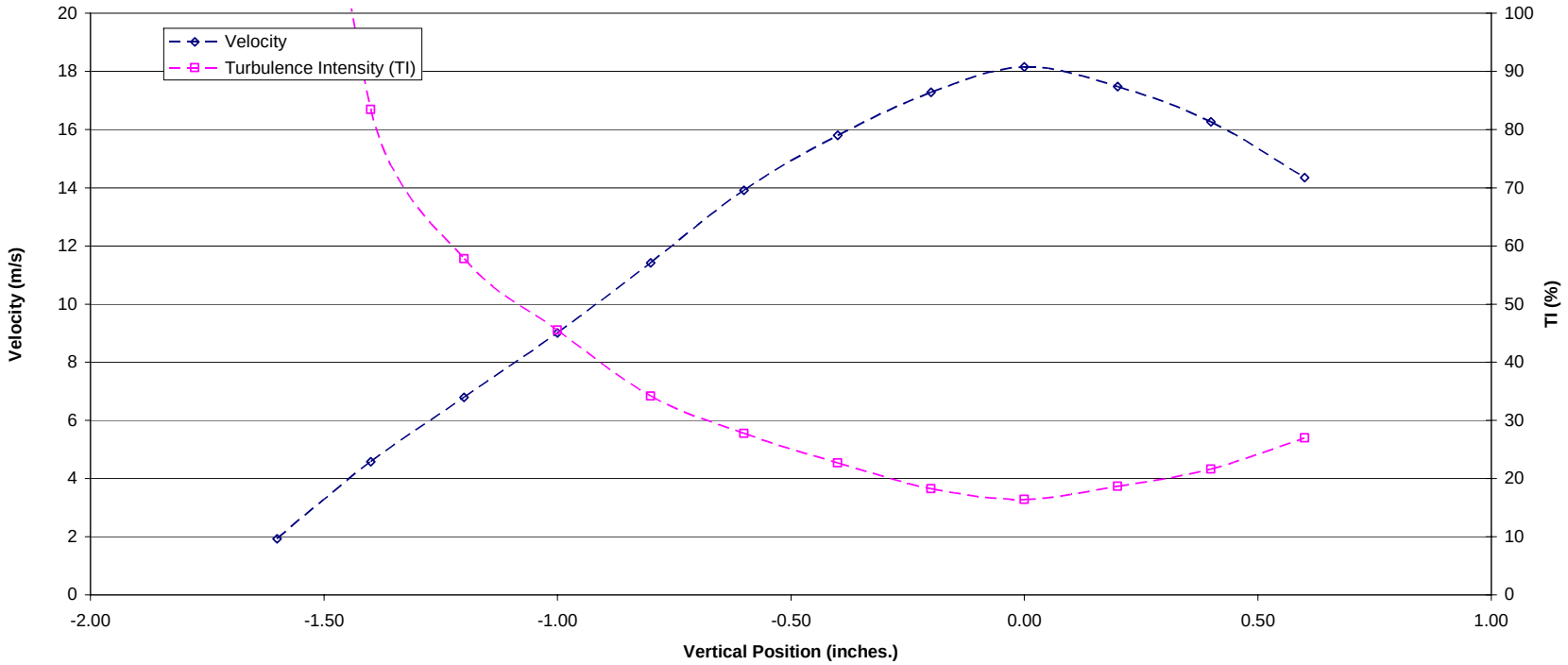

Figure B-46
Velocity and Turbulence Intensity as a Function of Vertical Position at a Horizontal Position of 9.0 Inches
(60 Degree Die – 2 psig Back Pressure)

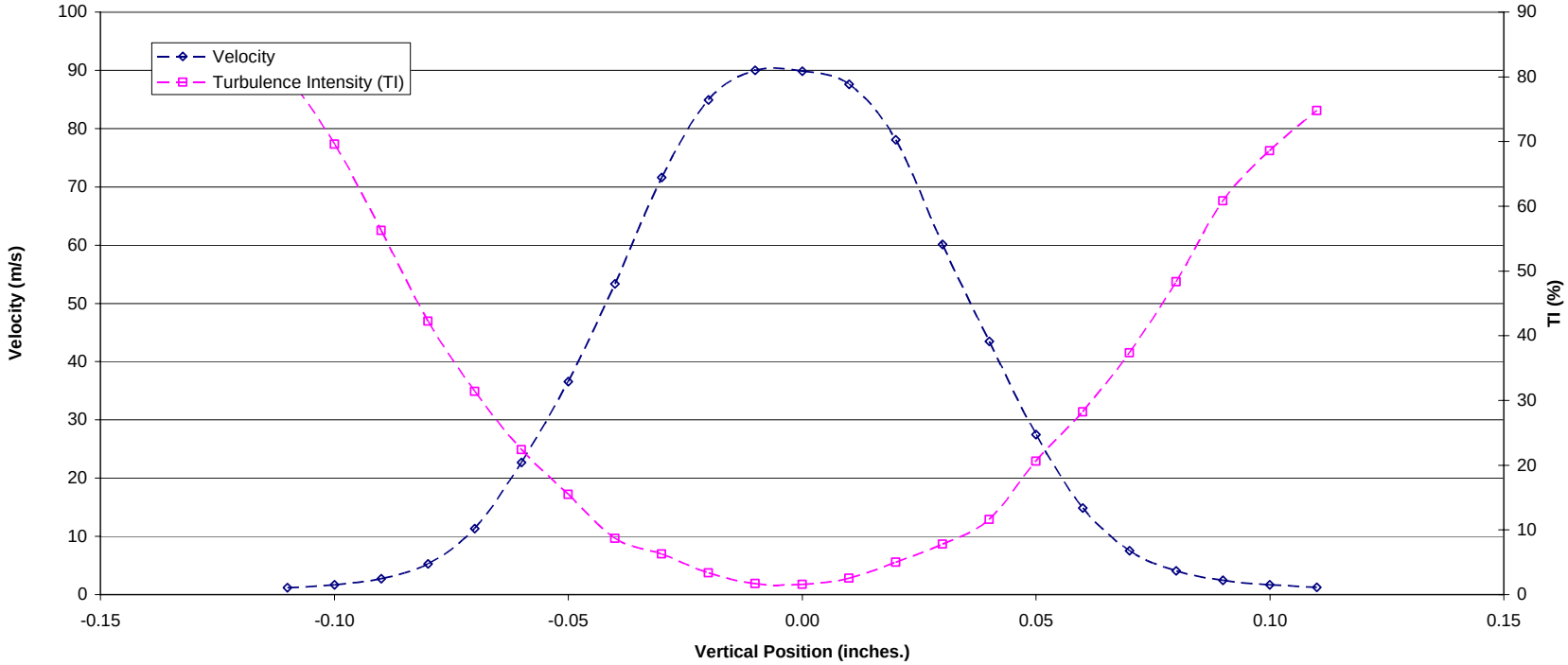

Figure B-47
Velocity and Turbulence Intensity as a Function of Vertical Position at a Horizontal Position of 0.2 Inches
(60 Degree Die – 2.125 psig Back Pressure)

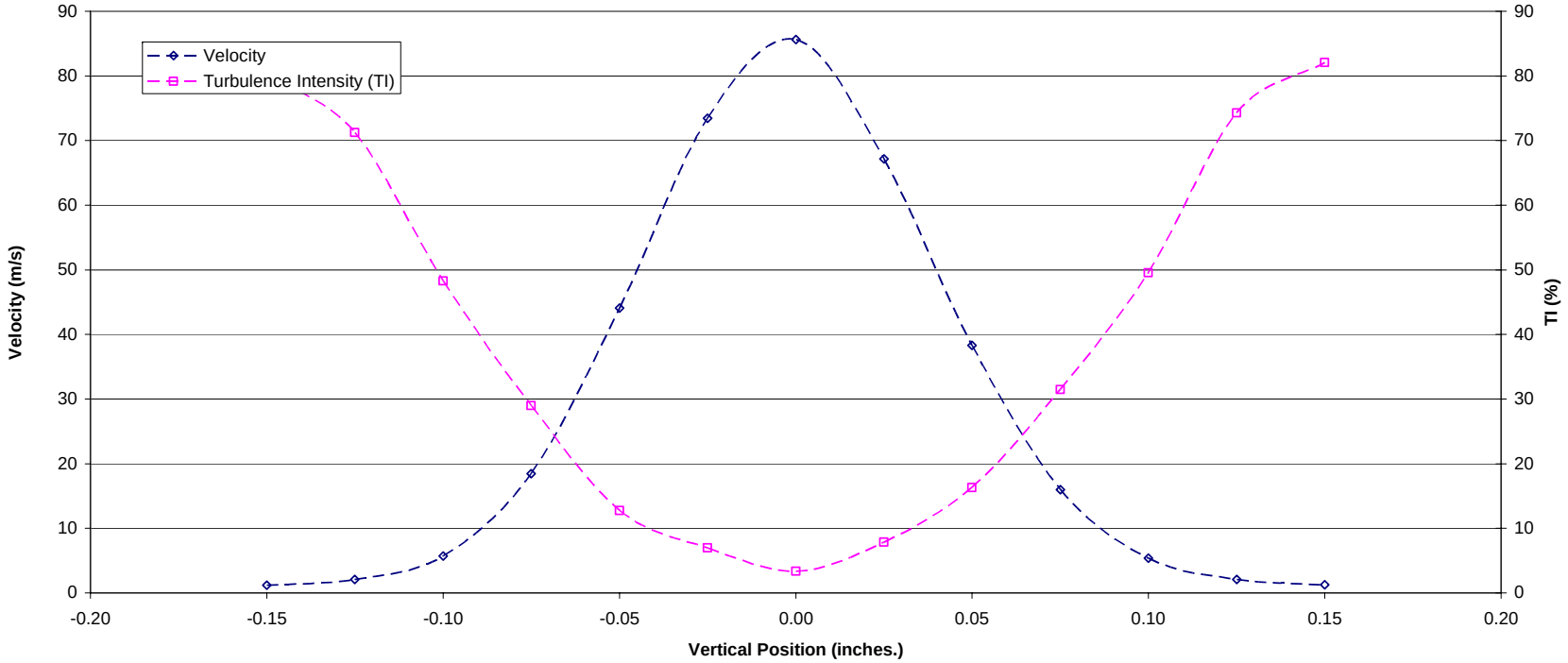

Figure B-48
Velocity and Turbulence Intensity as a Function of Vertical Position at a Horizontal Position of 0.3 Inches
(60 Degree Die – 2.125 psig Back Pressure)

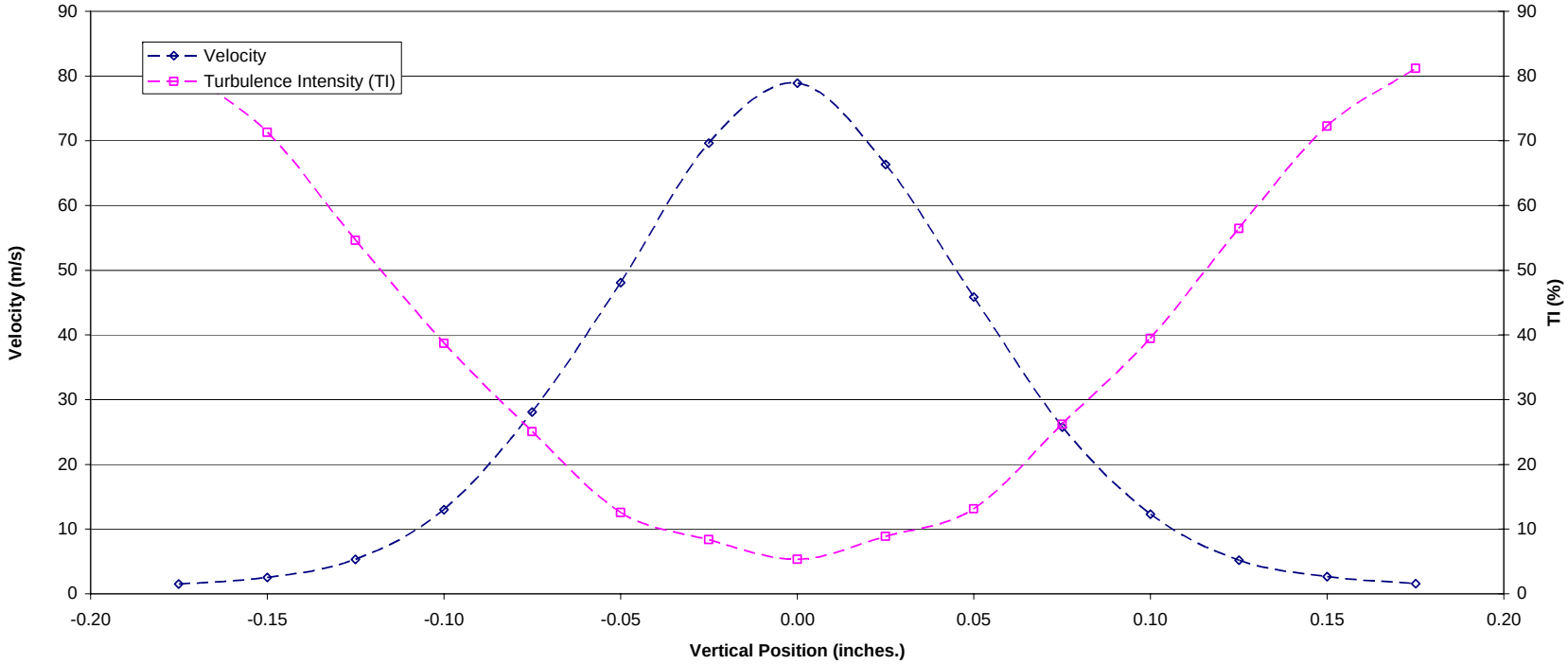

Figure B-49
Velocity and Turbulence Intensity as a Function of Vertical Position at a Horizontal Position of 0.4 Inches
(60 Degree Die – 2.125 psig Back Pressure)

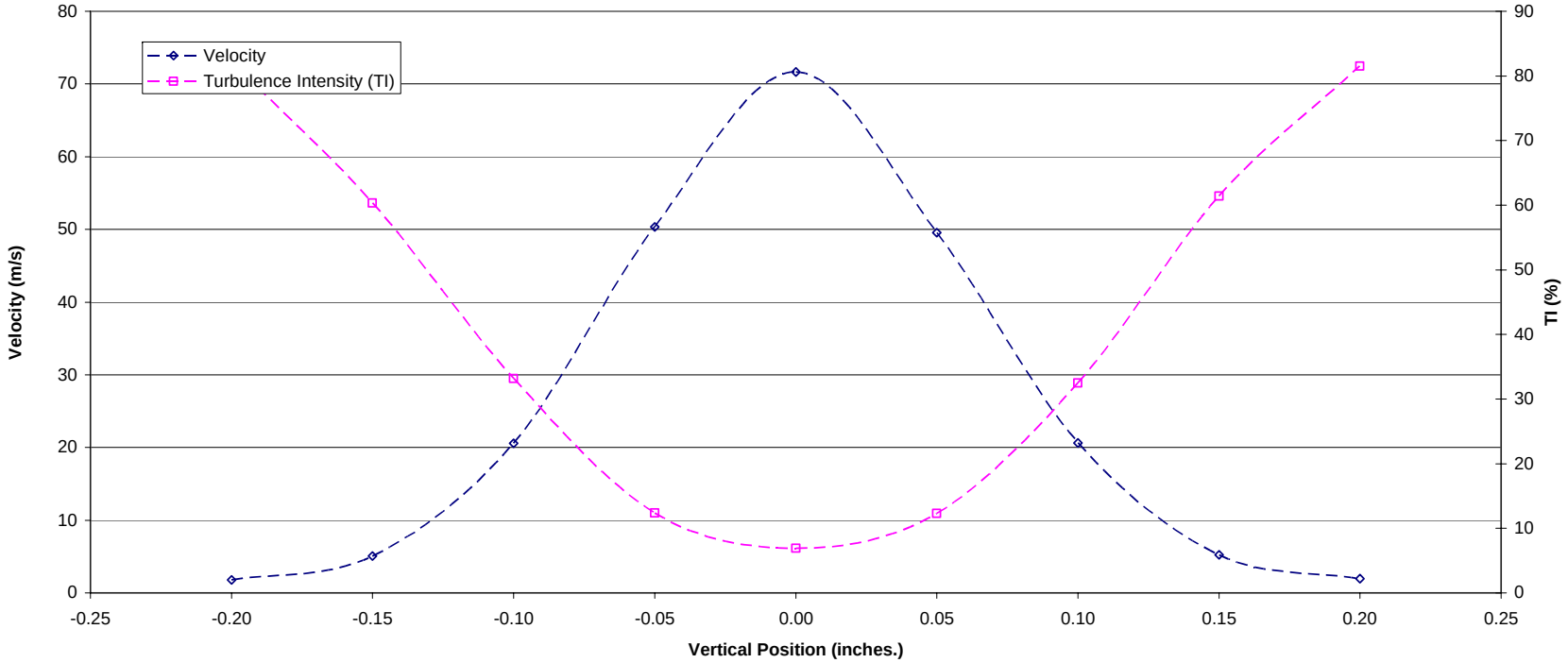

Figure B-50
Velocity and Turbulence Intensity as a Function of Vertical Position at a Horizontal Position of 0.5 Inches
(60 Degree Die – 2.125 psig Back Pressure)

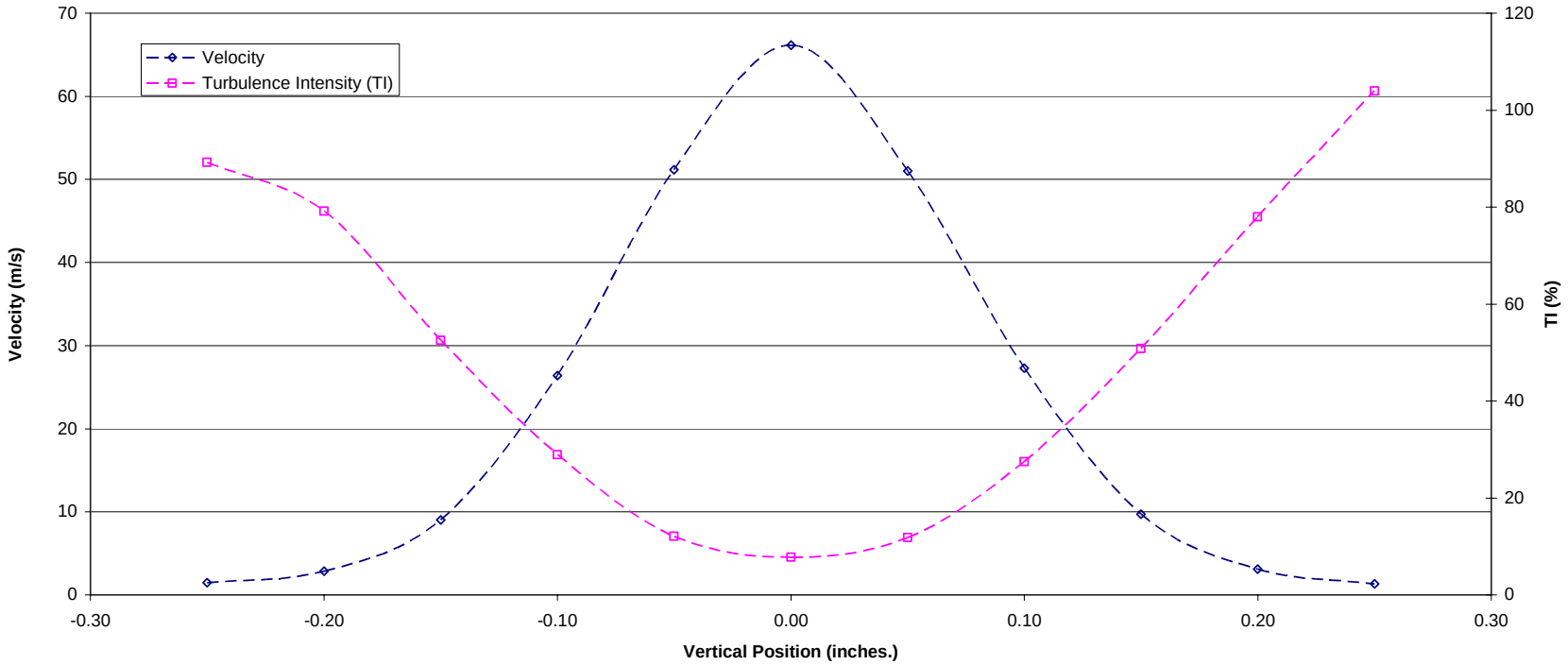

Figure B-51
Velocity and Turbulence Intensity as a Function of Vertical Position at a Horizontal Position of 0.6 Inches
(60 Degree Die – 2.125 psig Back Pressure)

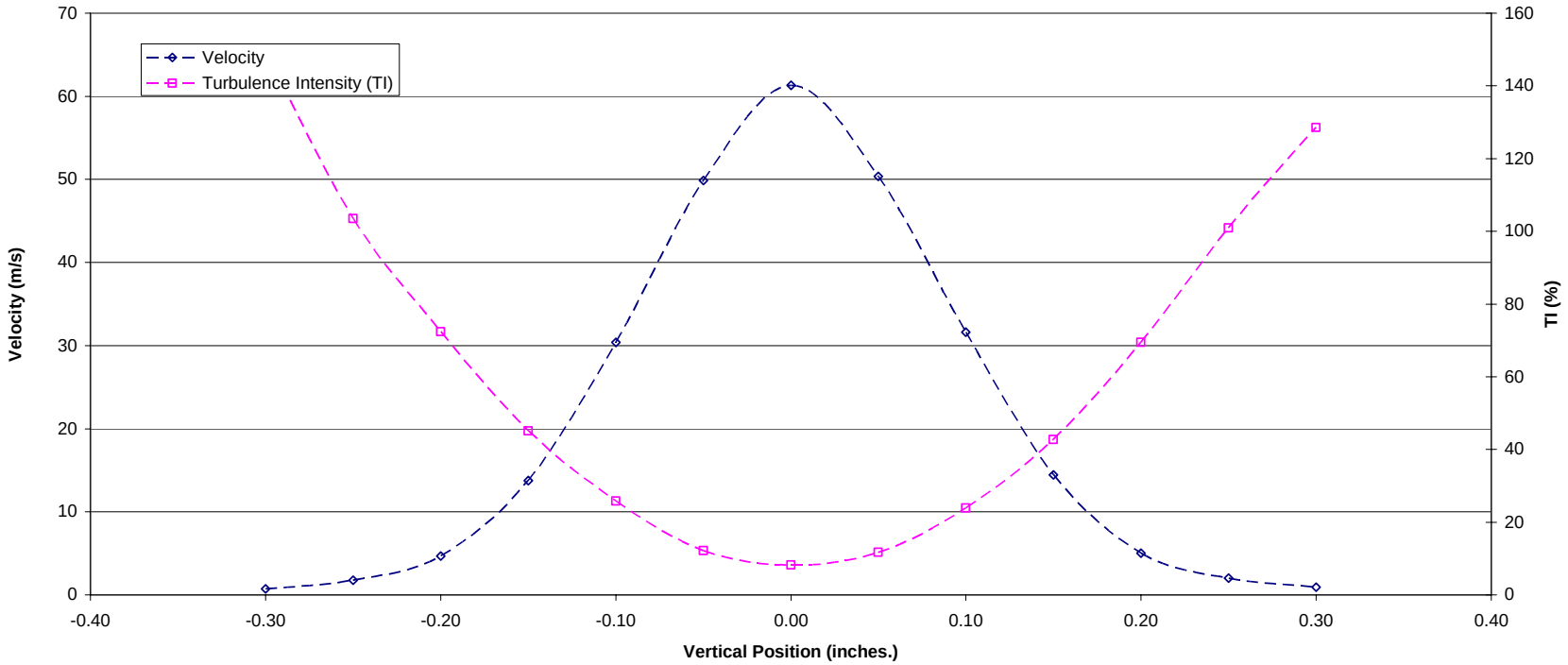

Figure B-52
Velocity and Turbulence Intensity as a Function of Vertical Position at a Horizontal Position of 0.7 Inches
(60 Degree Die – 2.125 psig Back Pressure)

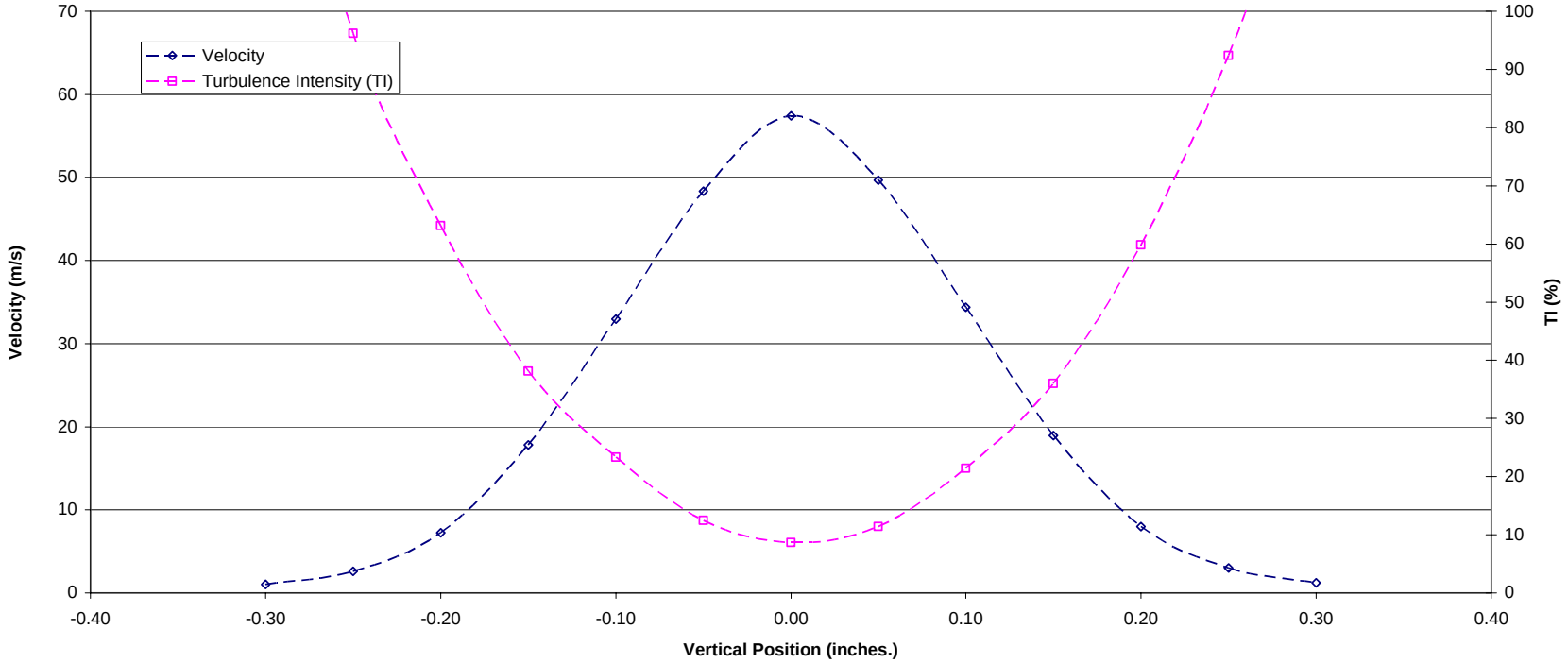

Figure B-53
Velocity and Turbulence Intensity as a Function of Vertical Position at a Horizontal Position of 0.8 Inches
(60 Degree Die – 2.125 psig Back Pressure)

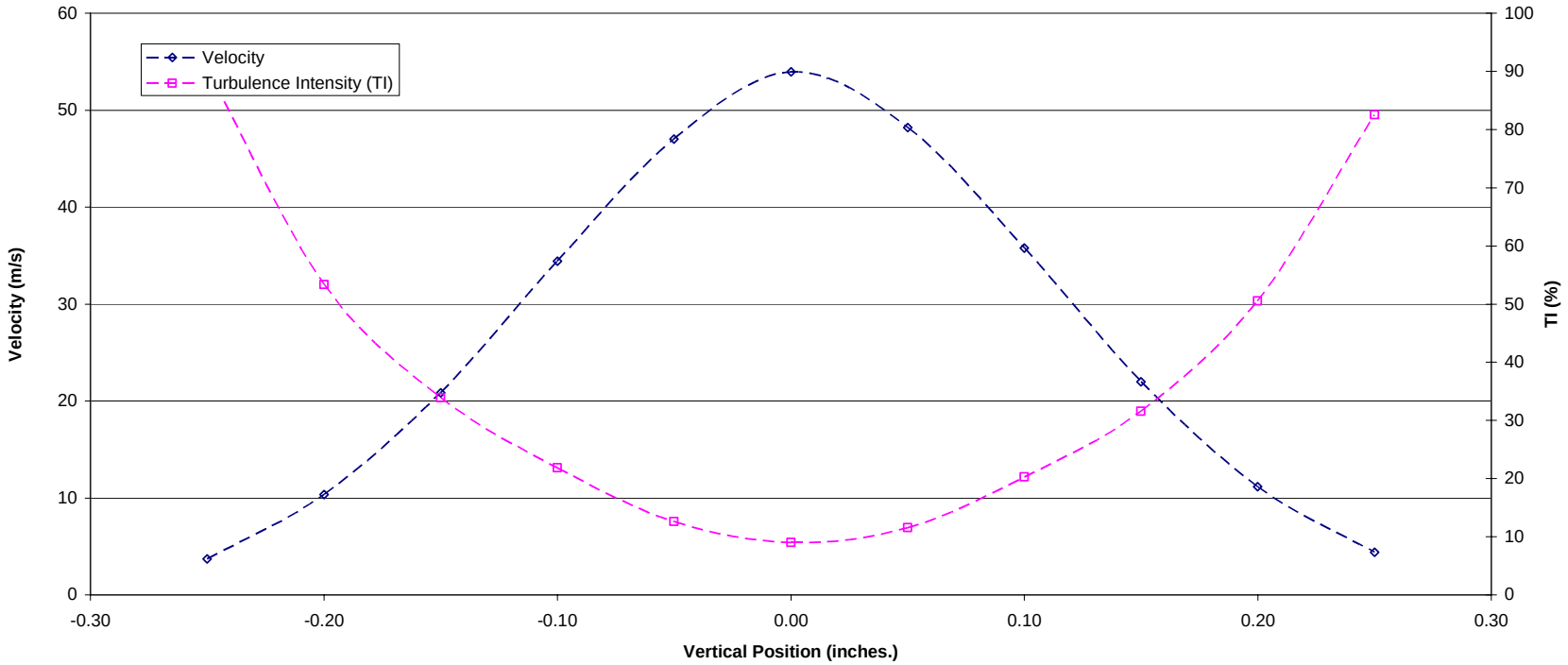

Figure B-54
Velocity and Turbulence Intensity as a Function of Vertical Position at a Horizontal Position of 0.9 Inches
(60 Degree Die – 2.125 psig Back Pressure)

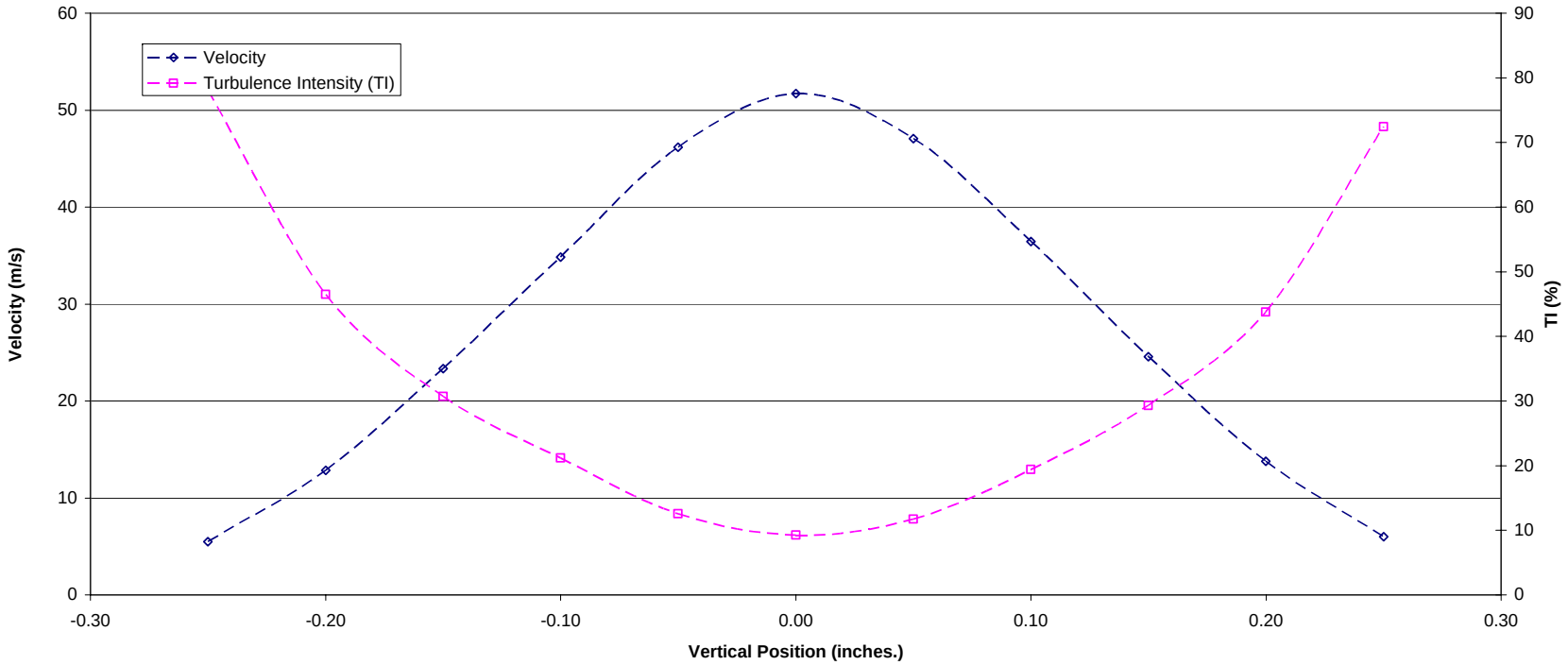

Figure B-55
Velocity and Turbulence Intensity as a Function of Vertical Position at a Horizontal Position of 1.0 Inches
(60 Degree Die – 2.125 psig Back Pressure)

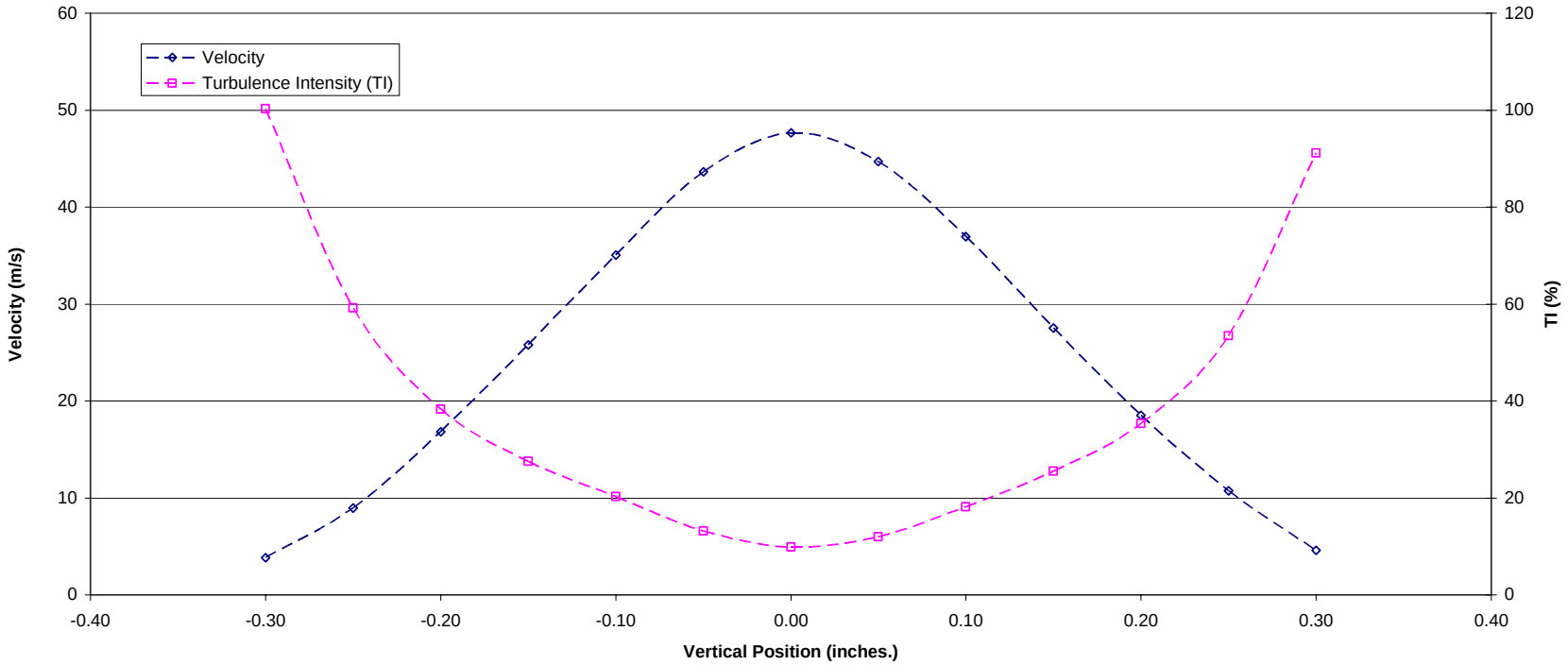

Figure B-56
Velocity and Turbulence Intensity as a Function of Vertical Position at a Horizontal Position of 1.2 Inches
(60 Degree Die – 2.125 psig Back Pressure)

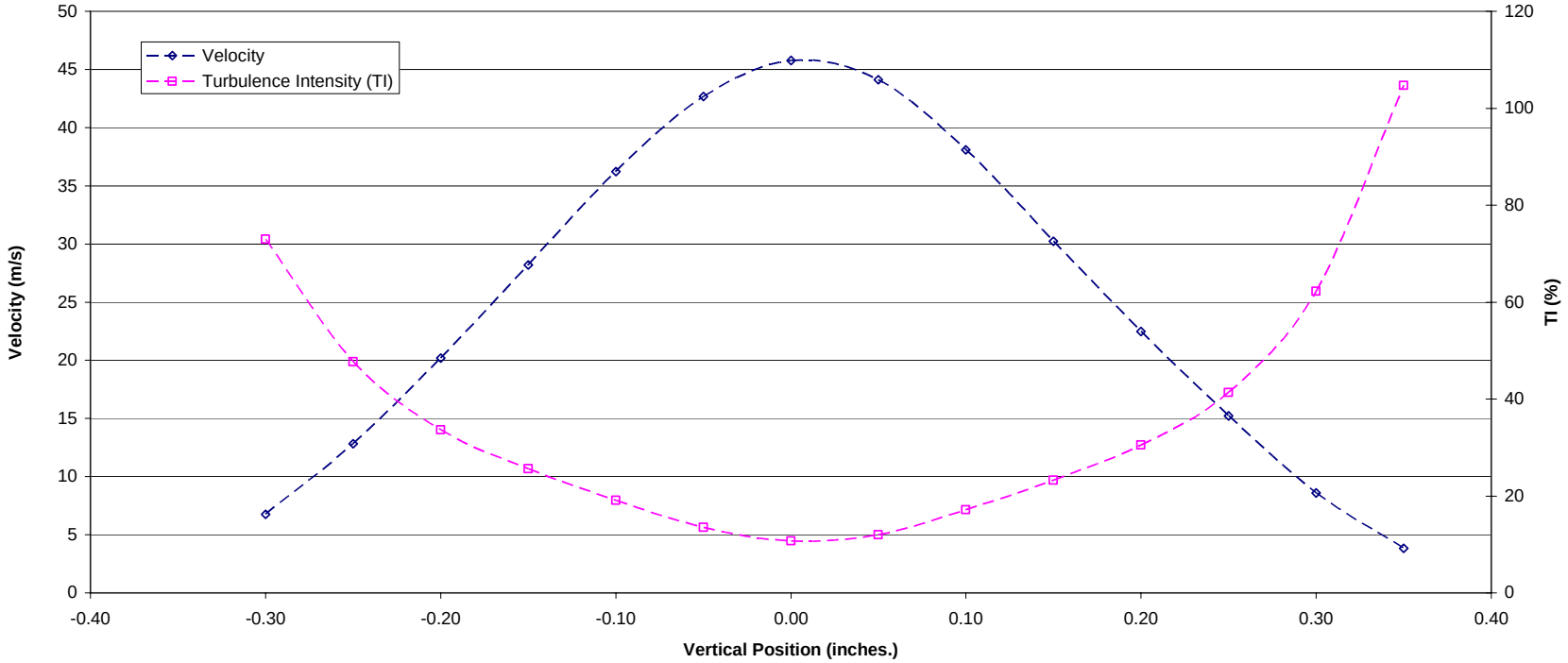

Figure B-57
Velocity and Turbulence Intensity as a Function of Vertical Position at a Horizontal Position of 1.4 Inches
(60 Degree Die – 2.125 psig Back Pressure)

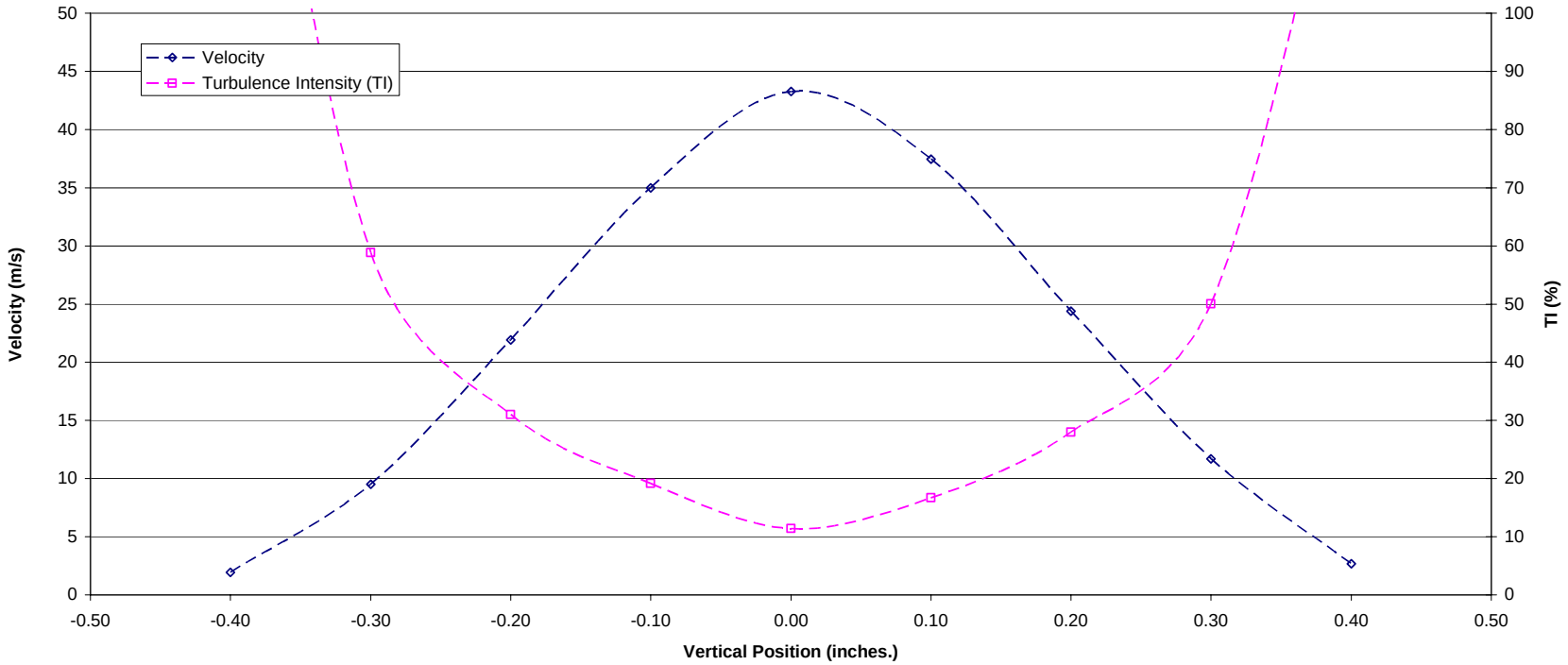

Figure B-58
Velocity and Turbulence Intensity as a Function of Vertical Position at a Horizontal Position of 1.6 Inches
(60 Degree Die – 2.125 psig Back Pressure)

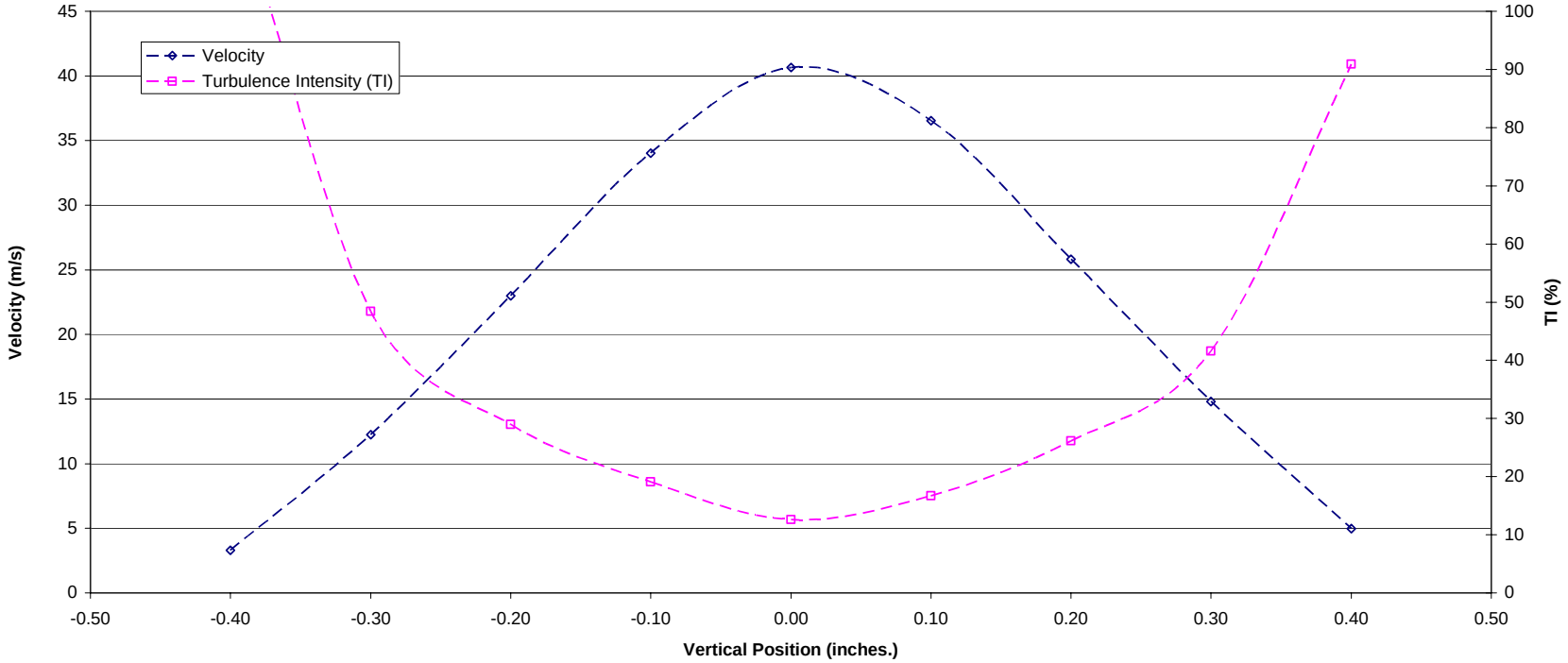

Figure B-59
Velocity and Turbulence Intensity as a Function of Vertical Position at a Horizontal Position of 1.8 Inches
(60 Degree Die – 2.125 psig Back Pressure)

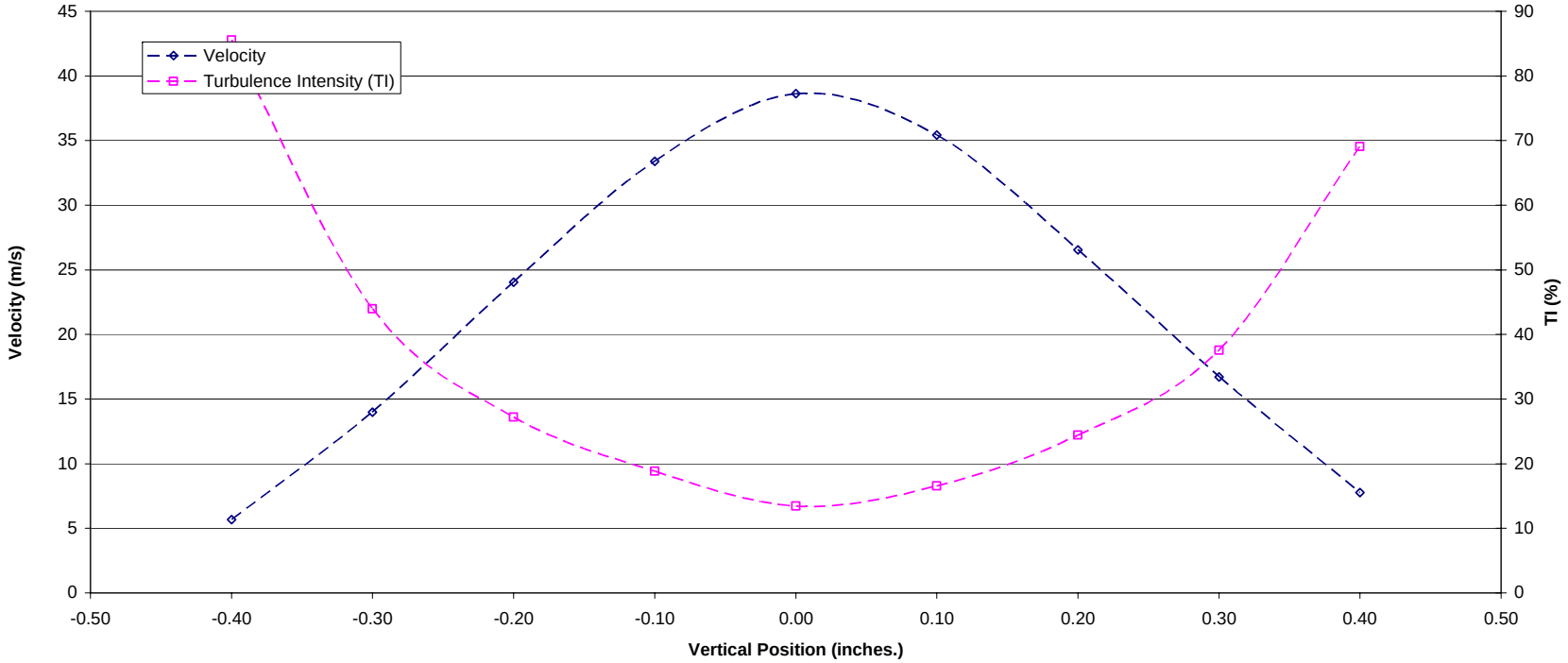

Figure B-60
Velocity and Turbulence Intensity as a Function of Vertical Position at a Horizontal Position of 2.0 Inches
(60 Degree Die – 2.125 psig Back Pressure)

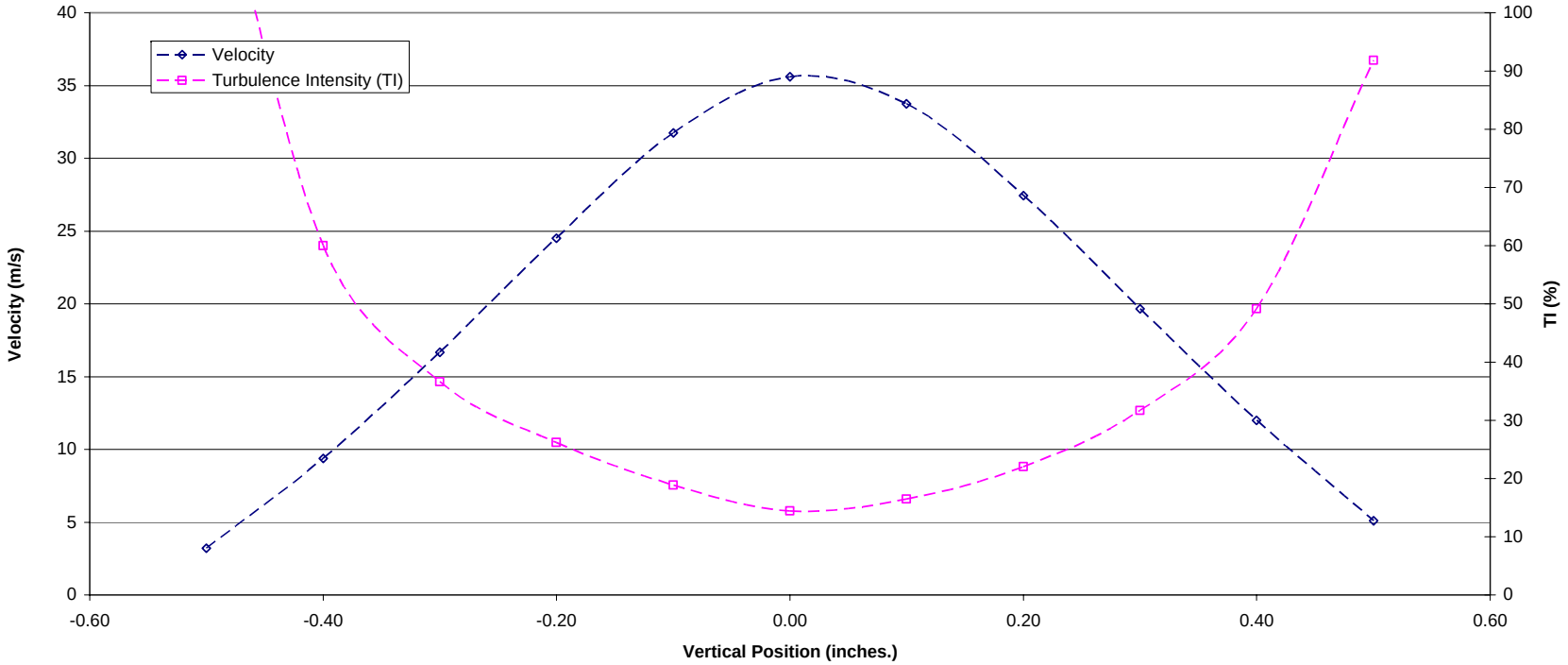

Figure B-61
Velocity and Turbulence Intensity as a Function of Vertical Position at a Horizontal Position of 2.4 Inches
(60 Degree Die – 2.125 psig Back Pressure)

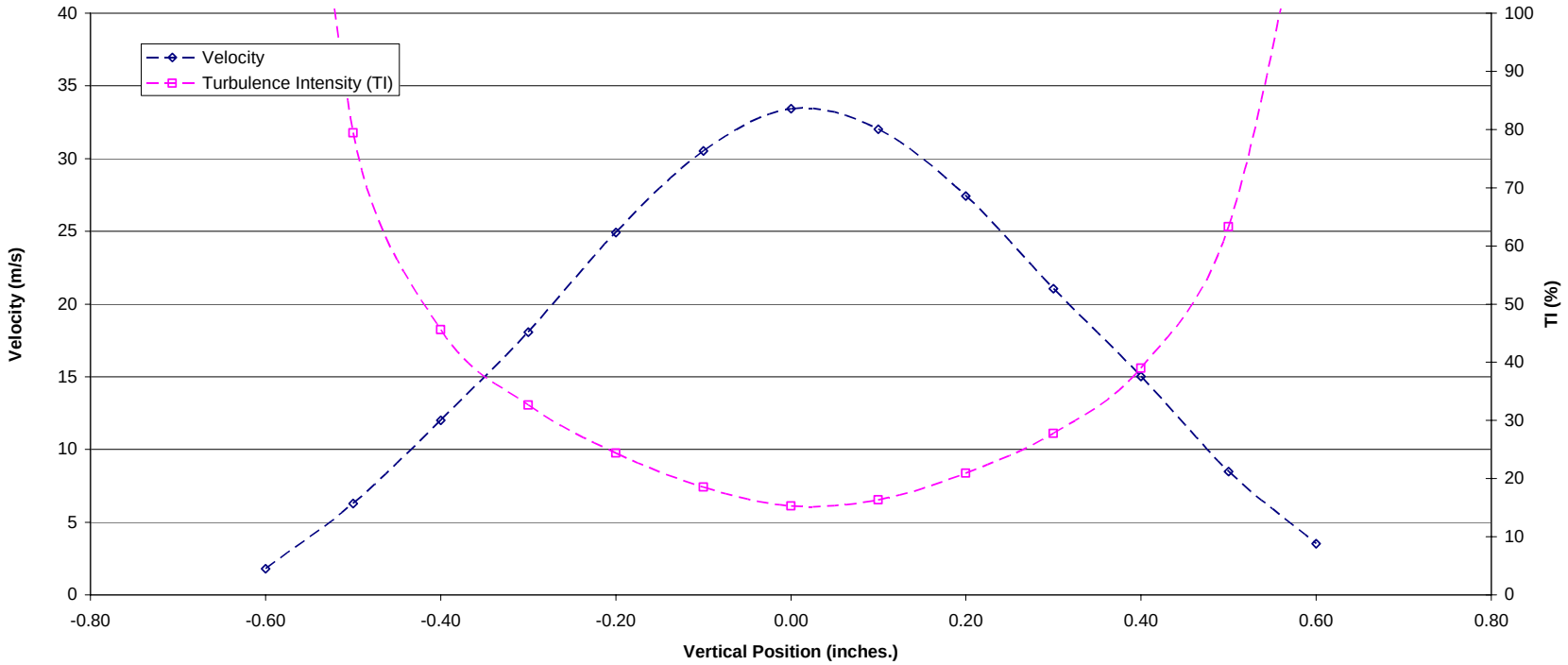

Figure B-62
Velocity and Turbulence Intensity as a Function of Vertical Position at a Horizontal Position of 2.8 Inches
(60 Degree Die – 2.125 psig Back Pressure)

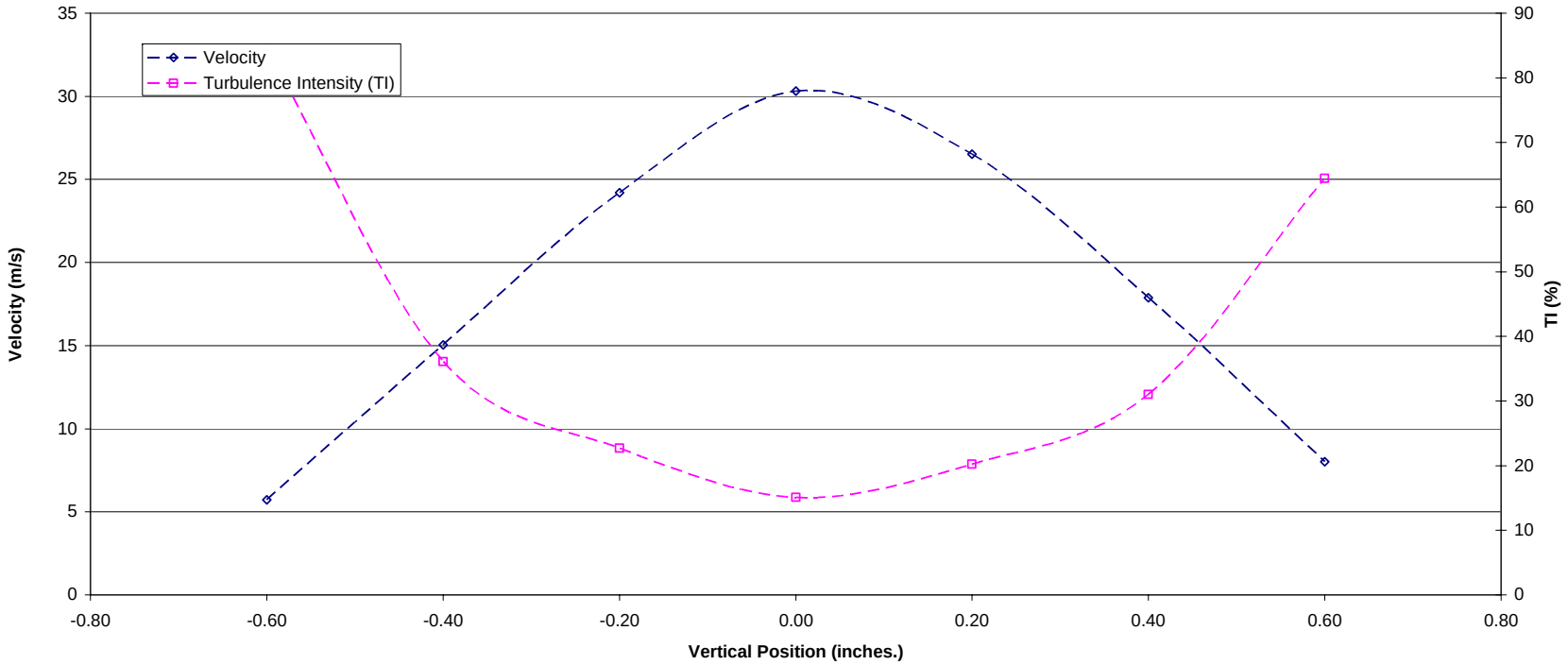

Figure B-63
Velocity and Turbulence Intensity as a Function of Vertical Position at a Horizontal Position of 3.5 Inches
(60 Degree Die – 2.125 psig Back Pressure)

VITA

Nathanael Tate McBee was born March 12, 1980 in Maryville, Tennessee. He grew up in Blount County and graduated from William Blount High School in 1998. He attended the University of Tennessee, Knoxville where he earned the degree of Bachelor of Science in Aerospace Engineering in 2004. He went on to pursue his Master of Science degree in Aerospace Engineering again from the University of Tennessee, Knoxville. He has begun his career with Analytical Graphics Inc. in Exton, Pennsylvania working as an Aerospace Application Support Engineer.